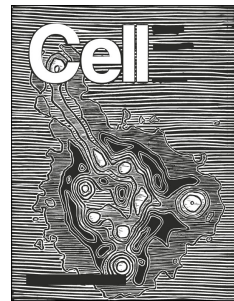


Journal Pre-proof



Severe COVID-19 is marked by a dysregulated myeloid cell compartment

Jonas Schulte-Schrepping, Nico Reusch, Daniela Paclik, Kevin Baßler, Stephan Schlickeiser, Bowen Zhang, Benjamin Krämer, Tobias Krammer, Sophia Brumhard, Lorenzo Bonaguro, Elena De Domenico, Daniel Wendisch, Martin Grasshoff, Theodore S. Kapellos, Michael Beckstette, Tal Pecht, Adem Saglam, Oliver Dietrich, Henrik E. Mei, Axel R. Schulz, Claudia Conrad, Désirée Kunkel, Ehsan Vafadarnejad, Cheng-Jian Xu, Arik Horne, Miriam Herbert, Anna Drews, Charlotte Thibeault, Moritz Pfeiffer, Stefan Hippenstiel, Andreas Hocke, Holger Müller-Redetzky, Katrin-Moira Heim, Felix Machleidt, Alexander Uhrig, Laure Bosquillon de Jarcy, Linda Jürgens, Miriam Stegemann, Christoph R. Glösenkamp, Hans-Dieter Volk, Christine Goffinet, Markus Landthaler, Emanuel Wyler, Philipp Georg, Maria Schneider, Chantip Dang-Heine, Nick Neuwinger, Kai Kappert, Rudolf Tauber, Victor Corman, Jan Raabe, Kim Melanie Kaiser, Michael To Vinh, Gereon Rieke, Christian Meisel, Thomas Ulas, Matthias Becker, Robert Geffers, Martin Witzenrath, Christian Drosten, Norbert Suttorp, Christof von Kalle, Florian Kurth, Kristian Händler, Joachim L. Schultze, Anna C. Aschenbrenner, Yang Li, Jacob Nattermann, Birgit Sawitzki, Antoine-Emmanuel Saliba, Leif Erik Sander, Deutsche COVID-19 OMICS Initiative (DeCOI)

PII: S0092-8674(20)30992-2

DOI: <https://doi.org/10.1016/j.cell.2020.08.001>

Reference: CELL 11548

To appear in: *Cell*

Received Date: 27 May 2020

Revised Date: 13 July 2020

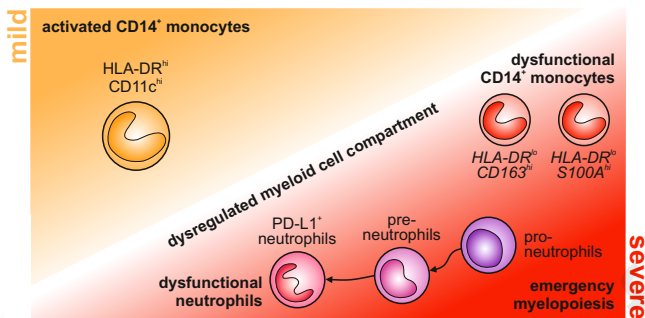
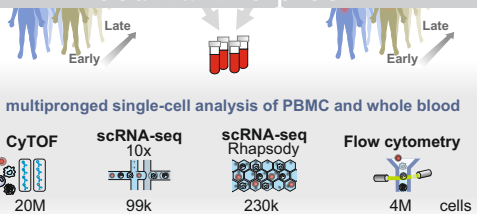
Accepted Date: 31 July 2020

Please cite this article as: Schulte-Schrepping, J., Reusch, N., Paclik, D., Baßler, K., Schlickeiser, S., Zhang, B., Krämer, B., Krammer, T., Brumhard, S., Bonaguro, L., De Domenico, E., Wendisch, D., Grasshoff, M., Kapellos, T.S., Beckstette, M., Pecht, T., Saglam, A., Dietrich, O., Mei, H.E., Schulz, A.R., Conrad, C., Kunkel, D., Vafadarnejad, E., Xu, C.-J., Horne, A., Herbert, M., Drews, A., Thibeault, C., Pfeiffer, M., Hippenstiel, S., Hocke, A., Müller-Redetzky, H., Heim, K.-M., Machleidt, F., Uhrig, A., Bosquillon de Jarcy, L., Jürgens, L., Stegemann, M., Glösenkamp, C.R., Volk, H.-D., Goffinet, C., Landthaler, M., Wyler, E., Georg, P., Schneider, M., Dang-Heine, C., Neuwinger, N., Kappert, K.,

Tauber, R., Corman, V., Raabe, J., Kaiser, K.M., Vinh, M.T., Rieke, G., Meisel, C., Ulas, T., Becker, M., Geffers, R., Witzenrath, M., Drosten, C., Suttorp, N., von Kalle, C., Kurth, F., Händler, K., Schultze, J.L., Aschenbrenner, A.C., Li, Y., Nattermann, J., Sawitzki, B., Saliba, A.-E., Sander, L.E., Deutsche COVID-19 OMICS Initiative (DeCOI), Severe COVID-19 is marked by a dysregulated myeloid cell compartment, *Cell* (2020), doi: <https://doi.org/10.1016/j.cell.2020.08.001>.

This is a PDF file of an article that has undergone enhancements after acceptance, such as the addition of a cover page and metadata, and formatting for readability, but it is not yet the definitive version of record. This version will undergo additional copyediting, typesetting and review before it is published in its final form, but we are providing this version to give early visibility of the article. Please note that, during the production process, errors may be discovered which could affect the content, and all legal disclaimers that apply to the journal pertain.

© 2020 Elsevier Inc.



1 Severe COVID-19 is marked by a dysregulated 2 myeloid cell compartment

3 Jonas Schulte-Schrepping^{1,2}, Nico Reusch^{1,2}, Daniela Paclik^{1,3}, Kevin Baßler^{1,2}, Stephan
4 Schlickeiser^{1,4}, Bowen Zhang^{1,5}, Benjamin Krämer^{1,6}, Tobias Krammer^{1,7}, Sophia
5 Brumhard^{1,8}, Lorenzo Bonaguro^{1,2}, Elena De Domenico^{1,9}, Daniel Wendisch^{1,8}, Martin
6 Grasshoff⁵, Theodore S. Kapellos², Michael Beckstette⁵, Tal Pecht², Adem Saglam⁹, Oliver
7 Dietrich⁷, Henrik E. Mei¹⁰, Axel R. Schulz¹⁰, Claudia Conrad⁸, Désirée Kunkel¹¹, Ehsan
8 Vafadarnejad⁷, Cheng-Jian Xu^{5,12}, Arik Horne², Miriam Herbert², Anna Drews⁹, Charlotte
9 Thibeault⁸, Moritz Pfeiffer⁸, Stefan Hippenstiel^{8,13}, Andreas Hocke^{8,13}, Holger Müller-
10 Redetzky⁸, Katrin-Moira Heim⁸, Felix Machleidt⁸, Alexander Uhrig⁸, Laure Bosquillon de
11 Jarcy⁸, Linda Jürgens⁸, Miriam Stegemann⁸, Christoph R. Glösenkamp⁸, Hans-Dieter
12 Volk^{3,4,14}, Christine Goffinet^{15,16}, Markus Landthaler¹⁷, Emanuel Wyler¹⁷, Philipp Georg⁸,
13 Maria Schneider³, Chantip Dang-Heine¹⁸, Nick Neuwinger¹⁹, Kai Kappert¹⁹, Rudolf Tauber¹⁹,
14 Victor Corman¹⁵, Jan Raabe⁶, Kim Melanie Kaiser⁶, Michael To Vinh⁶, Gereon Rieke⁶,
15 Christian Meisel¹⁴, Thomas Ulas⁹, Matthias Becker⁹, Robert Geffers²⁰, Martin Witzenrath^{8,13},
16 Christian Drosten^{15,21}, Norbert Suttorp^{8,13}, Christof von Kalle¹⁷, Florian Kurth^{8,22}, Kristian
17 Händler⁹, Joachim L. Schultze^{2,9,23,*}, Anna C. Aschenbrenner^{23,24}, Yang Li^{5,12,23}, Jacob
18 Nattermann^{6,21,23}, Birgit Sawitzki^{3,23}, Antoine-Emmanuel Saliba^{7,23}, Leif Erik Sander^{6,13,23},
19 Deutsche COVID-19 OMICS Initiative (DeCOI)

20 Affiliations

21 1 Equally contributing author

22 2 Life & Medical Sciences (LIMES) Institute, University of Bonn, Germany

23 3 Institute of Medical Immunology, Charité, Universitätsmedizin Berlin, Berlin, Germany

24 4 Institute of Medical Immunology, Charité, Universitätsmedizin Berlin, Berlin, Germany & BIH
25 Center for Regenerative Therapies, Charité and Berlin Institute of Health, Charité,
26 Universitätsmedizin Berlin, Berlin, Germany

27 5 Centre for Individualised Infection Medicine (CiIM) & TWINCORE, joint ventures between the
28 Helmholtz-Centre for Infection Research (HZI) and the Hannover Medical School (MHH),
29 Hannover, Germany

30 6 Department of Internal Medicine I, University Hospital Bonn, Bonn Germany

31 7 Helmholtz Institute for RNA-based Infection Research (HIRI), Helmholtz-Center for Infection
32 Research (HZI), Würzburg, Germany

33 8 Department of Infectious Diseases and Respiratory Medicine, Charité Universitätsmedizin Berlin,
34 Berlin, Germany

35 9 German Center for Neurodegenerative Diseases (DZNE). PRECISE Platform for Genomics and
36 Epigenomics at DZNE and University of Bonn, Germany

37 10 Mass Cytometry Lab, DRFZ Berlin, a Leibniz Institute, Berlin, Germany

- 38 11 Flow & Mass Cytometry Core Facility, Charité Universitätsmedizin Berlin and Berlin Institute of
39 Health (BIH), Berlin, Germany
- 40 12 Department of Internal Medicine and Radboud Center for Infectious Diseases, Radboud
41 University Medical Center, Nijmegen, the Netherlands
- 42 13 German Center for Lung Research (DZL)
- 43 14 Institute of Medical Immunology, Charité, Universitätsmedizin Berlin, Berlin, Germany, Labor
44 Berlin-Charité Vivantes, Department of Immunology, Berlin, Germany
- 45 15 Institute of Virology, Charité Universitätsmedizin Berlin, Berlin, Germany
- 46 16 Berlin Institute of Health, 10178 Berlin, Germany
- 47 17 Berlin Institute for Medical Systems Biology, Max-Delbrück-Center for Molecular Medicine in the
48 Helmholtz Association, 13125, Berlin, Germany.
- 49 18 Clinical Study Center (CSC), Berlin Institute of Health, and Charité - Universitätsmedizin Berlin,
50 Berlin, Germany
- 51 19 Institute of Laboratory Medicine, Clinical Chemistry and Pathobiochemistry, Charité,
52 Universitätsmedizin Berlin, Labor Berlin-Charité Vivantes, Berlin, Germany
- 53 20 Genome Analytics, Helmholtz-Center for Infection Research (HZI), Braunschweig, Germany
- 54 21 German Center for Infection Research (DZIF)
- 55 22 Department of Tropical Medicine, Bernhard Nocht Institute for Tropical Medicine & I. Department
56 of Medicine, University Medical Center Hamburg-Eppendorf, Hamburg, Germany
- 57 23 Senior authors
- 58 24 Life & Medical Science (LIMES) Institute, University of Bonn, Germany and Radboud UMC,
59 Nijmegen, The Netherlands
- 60 * Lead Contact Joachim L. Schultze, j.schultze@uni-bonn.de

61

62 Summary

63 Coronavirus Disease 2019 (COVID-19) is a mild to moderate respiratory tract infection,
64 however, a subset of patients progresses to severe disease and respiratory failure. The
65 mechanism of protective immunity in mild forms and the pathogenesis of severe COVID-19,
66 associated with increased neutrophil counts and dysregulated immune responses, remains
67 unclear. In a dual-center, two-cohort study, we combined single-cell RNA-sequencing and
68 single-cell proteomics of whole blood and peripheral blood mononuclear cells to determine
69 changes in immune cell composition and activation in mild vs. severe COVID-19 (242
70 samples from 109 individuals) over time. HLA-DR^{hi}CD11c^{hi} inflammatory monocytes with an
71 interferon-stimulated gene signature were elevated in mild COVID-19. Severe COVID-19
72 was marked by occurrence of neutrophil precursors, as evidence of emergency
73 myelopoiesis, dysfunctional mature neutrophils, and *HLA-DR^{lo}* monocytes. Our study
74 provides detailed insights into the systemic immune response to SARS-CoV-2 infection and
75 it reveals profound alterations in the myeloid cell compartment associated with severe
76 COVID-19.

77 Introduction

78 Clinical presentations of COVID-19 are highly variable, and while the majority of patients
 79 experiences mild to moderate symptoms, 10-20% of patients develop pneumonia and
 80 severe disease (Huang et al., 2020a; Wang et al., 2020; Zhou et al., 2020a). Clinical
 81 deterioration with respiratory failure and acute respiratory distress syndrome (ARDS)
 82 typically develops in the second week of disease. This kinetic may suggest a role for
 83 secondary immune responses in the development of severe COVID-19 (Ziying Ong et al.,
 84 2020). However, the exact mechanisms that govern the pathophysiology of the different
 85 disease courses of COVID-19 remain ill-defined.

86 Single-cell studies of bronchoalveolar lavage samples have suggested a complex
 87 dysregulation of the pulmonary immune response in severe COVID-19 (Chua et al., 2020;
 88 Liao et al., 2020). Overall, systemic inflammation is linked to an unfavorable clinical course
 89 of disease and the development of severe COVID-19 (Giamarellos-Bourboulis et al., 2020;
 90 Lucas et al., 2020; Ziying Ong et al., 2020). SARS-CoV-2 infection induces specific T cell
 91 and B cell responses, which is reflected by elevation of SARS-CoV-2 peptide-specific T cells
 92 (Braun et al., 2020; Grifoni et al., 2020) and the production of SARS-CoV-2 specific
 93 antibodies (Long et al., 2020; Ni et al., 2020; Robbiani et al., 2020). Patients with severe
 94 COVID-19 have high systemic levels of inflammatory cytokines, particularly IL-6 and IL-1 β
 95 (Chen et al., 2020; Giamarellos-Bourboulis et al., 2020; Lucas et al., 2020; Ziying Ong et al.,
 96 2020), whereas interferon (IFN) responses appear blunted, as shown by whole blood
 97 transcriptomics (Hadjadj et al., 2020) and plasma profiling (Trouillet-Assant et al., 2020). A
 98 number of studies and regular clinical observations indicate an increase of neutrophils and a
 99 decrease of non-classical ($CD14^{lo}CD16^{hi}$) monocytes in severe COVID-19 (Hadjadj et al.,
 100 2020; Merad and Martin, 2020; Sanchez-Cerrillo et al., 2020). Profound immune
 101 dysregulation is commonly observed in severe infections and sepsis, characterized by a
 102 progression from hyperinflammatory states to immunosuppression (Remy et al., 2020;
 103 Ritchie and Singanayagam, 2020) and similar mechanisms have been proposed for severe
 104 COVID-19 (Giamarellos-Bourboulis et al., 2020). Yet, comprehensive insights into the
 105 immunopathology of severe COVID-19 are still missing. Exacerbated immune responses
 106 played a major role in the pathophysiology of SARS, leading to severe lung injury and
 107 respiratory failure (Perlman and Dandekar, 2005). Mitigation of immunodysregulation is
 108 therefore viewed as a major therapeutic avenue for the treatment and prevention of severe
 109 COVID-19 (Dimopoulos et al., 2020; Jamilloux et al., 2020). In support of this view, a recent
 110 multicenter study reported that dexamethasone treatment significantly reduced mortality in
 111 hospitalized patients with COVID-19, particularly in patients on mechanical ventilation (Horby
 112 et al., 2020). Previous studies of peripheral blood mononuclear cell (PBMC) transcriptomes
 113 in a small number of patients with COVID-19, revealed changes in several cellular
 114 compartments, including monocytes, NK cells, dendritic cells (DCs) and T cells (Lee et al.,
 115 2020; Wilk et al., 2020).

116 The heterogeneity of clinical manifestations and the complexity of immune responses to
 117 COVID-19 highlight the need for detailed analyses using high-resolution techniques and
 118 well-characterized clinical cohorts. We hypothesized that distinct responses, particularly
 119 within the innate immune system, underlie the different clinical trajectories of COVID-19
 120 patients (Chua et al., 2020; Kuri-Cervantes et al., 2020; Mathew et al., 2020; McKechnie and

121 Blish, 2020). Here, we used single-cell transcriptomics and single-cell proteomics to analyze
122 immune responses in blood samples in two independent cohorts of COVID-19 patients.

123 Activated HLA-DR^{hi}CD11c^{hi}CD14⁺ monocytes were increased in patients with mild COVID-
124 19, similar to patients with SARS-CoV-2 negative flu-like illness ('FLI'). In contrast,
125 monocytes characterized by low expression of *HLA-DR*, and marker genes indicative of anti-
126 inflammatory functions (e.g. *CD163*, *PLAC8*) appeared in patients with severe COVID-19.
127 The granulocyte compartment was profoundly altered in severe COVID-19, marked by the
128 appearance of neutrophil precursors due to emergency myelopoiesis, dysfunctional
129 neutrophils expressing PD-L1, and exhibiting an impaired oxidative burst response.
130 Collectively, our study links highly dysregulated myeloid cell responses to severe COVID-19.

131 **Results**

132 Dual center cohort study to assess immunological alterations in COVID-19 patients

133 In order to probe the divergent immune responses in mild vs. severe COVID-19, we
 134 analyzed blood samples collected from independent patient cohorts at two university medical
 135 centers in Germany. Samples from the Berlin cohort (cohort 1) (Kurth et al., 2020), were
 136 analyzed by mass cytometry (CyTOF) and single-cell RNA-sequencing (scRNA-seq) using a
 137 droplet-based single-cell platform (10x Chromium), while samples from the Bonn cohort
 138 (cohort 2) were analyzed by multi-color flow cytometry (MCFC) and on a microwell-based
 139 scRNA-seq system (BD Rhapsody). We analyzed a total of 24 million cells by their protein
 140 markers and >328,000 cells by scRNA-seq in 242 samples from 53 COVID-19 patients and
 141 56 controls, including 8 patients with FLI (**Fig. 1A+B, S1A, Table S1**).

142 We first characterized alterations of the major leukocyte lineages by mass cytometry on
 143 whole blood samples from 20 COVID-19 patients collected between day 4 and day 29 after
 144 symptom onset, and compared them to 10 age- and gender-matched controls and 8 FLI
 145 patients. We designed two antibody panels to specifically capture alterations in mononuclear
 146 leukocytes (lymphocytes, monocytes and DCs, panel 1), and in granulocytes (panel 2, **Table**
 147 **S2**). High-resolution SPADE analysis was performed with 400 target nodes and individual
 148 nodes were aggregated into cell subsets based on lineage-specific markers, such as CD14
 149 for monocytes and CD15 for neutrophils (**Fig. S1B**). Uniform Manifold Approximation and
 150 Projection (UMAP) analysis revealed distinct clustering of samples from COVID-19 patients,
 151 FLI, and healthy controls, with marked changes of the monocyte and granulocyte
 152 compartment (**Fig. 1C**). Leukocyte lineages were compared in the earliest available samples
 153 in COVID-19 patients (day 4 to 13), FLI, and controls (**Table S1, Fig. 1D**). Since leukocyte
 154 counts were not available for all control samples, we compared the control samples for
 155 CyTOF ('ctrl CyTOF') to data from our recently published healthy control cohorts ('ctrl flow')
 156 (Kverneland et al., 2016; Sawitzki et al., 2020). The proportions of all major lineages were
 157 highly similar, irrespective of the methodology (**Fig. 1D**). Cell counts of the published cohort
 158 could therefore be used as a reference to report absolute cell counts for leukocyte lineages
 159 in COVID-19 samples. In line with recent reports (Barnes et al., 2020; Xintian et al., 2020),
 160 we observed elevated leukocytes and increased proportions of neutrophils in patients with
 161 severe COVID-19 (**Fig. 1D**), whereas only proportional increases in neutrophils were evident
 162 in FLI and mild COVID-19 patients (**Fig. 1D**). Total lymphocytes and T cells were strongly
 163 reduced in all COVID-19 and FLI patients, whereas non-classical monocytes were
 164 specifically depleted in COVID-19 (**Fig. 1D**). Increased neutrophils in severe COVID-19 and
 165 loss of non-classical monocytes in both mild and severe disease, were validated in cohort 2
 166 by MCFC (**Fig. S1C, Table S1+3**).

167 Thus, SARS-CoV-2 infection is associated with lymphopenia and profound alterations of the
 168 myeloid compartment.

169

170 Severity-dependent alterations of the myeloid cell compartment in COVID-19

171 Given the dramatic changes in various immune cell populations (**Fig. 1C+D**), we next
 172 assessed their composition and activation state by droplet-based scRNA-seq in 27 samples
 173 from 18 COVID-19 patients (8 mild & 10 severe, cohort 1, **Table S1**) collected between day
 174 3 and day 20 after symptom onset. A total of 48,266 single-cell transcriptomes of PBMC
 175 were analyzed together with 50,783 PBMC from publicly available control datasets (21
 176 control donors, **Table S1**). UMAP and high-resolution cell type classification identified all cell
 177 types expected in the mononuclear compartment of blood with a high granularity in the
 178 monocytes, identifying five distinct clusters (cluster 0-4) (**Fig. 2A+S2A, Table S4**).
 179 Monocytes in clusters 0-3 expressed *CD14*, cluster 4 comprised the non-classical
 180 monocytes marked by *FCGR3A* (encoding CD16a) and low expression of *CD14*. Separate
 181 visualization of cells in mild and severe cases revealed highly disease severity-specific
 182 clusters (**Fig. 2B**). A distinct subset of *CD14⁺* monocytes (cluster 1) (**Fig. 2A**) marked by high
 183 expression of *HLA-DRA*, *HLA-DRB1* and co-stimulatory molecule *CD83* (**Fig. S2D**),
 184 engagement of which has been linked to prolonged expansion of antigen-specific T cells
 185 (Hirano et al., 2006), was selectively detected in mild COVID-19 (**Fig. 2C**). In addition, we
 186 identified another closely related *CD14⁺HLA-DR^{hi}* monocyte population (cluster 2), which
 187 was characterized by high expression of IFN-stimulated genes (ISGs). However, upon closer
 188 analysis, this cluster was found to originate from a single donor with mild COVID-19 (**Fig.**
 189 **2A-C, Fig. S2D**). Both cluster 1 and cluster 2 expressed high levels of ISGs *IFI6* and *ISG15*
 190 (**Fig. S2D**). In patients with severe COVID-19, monocytes showed low expression of *HLA-*
 191 *DR* and high expression of alarmins *S100A8/9/12* (cluster 3, **Fig. 2A-C, Fig. S2D**). The most
 192 prominent change in severe COVID-19 was the appearance of two distinct cell populations
 193 (cluster 5+6), absent in PBMC of patients with mild COVID-19 and control donors (**Fig. 2A**).
 194 Published markers (Kwok et al., 2020; Ng et al., 2019) identified cluster 5 and 6 as
 195 neutrophils and immature neutrophils, respectively (**Fig. 2A+B**). Immature neutrophils
 196 (cluster 6) expressed *CD24*, *PGLYRP1*, *DEFA3* and *DEFA4*, whereas neutrophil cluster 5
 197 expressed *FCGR3B* (CD16b), *CXCL8*, and *LCN2* (lipocalin 2) (**Fig. 2C, Fig. S2A**). Their
 198 migration within the PBMC fraction on a density gradient marked these cells as low-density
 199 neutrophils (LDN).

200 In the second cohort, PBMC from 17 COVID-19 patients (8 mild, 9 severe, **Table S1**),
 201 sampled between 2 and 25 days after symptom onset, and 13 controls, were collected for
 202 scRNA-Seq on a microwell-based platform (BD Rhapsody). High-quality single-cell
 203 transcriptomes for 139,848 PBMC were assessed and their population structure was
 204 visualized using UMAP (**Fig. 2D, Table S4**). Data-driven cell type classification (Aran et al.,
 205 2019) and cluster-specific marker gene expression identified all cell types expected in the
 206 PBMC compartment and revealed additional clusters and substructures (**Fig. 2D+S2B**).
 207 Similar to cohort 1, monocytes exhibited significant plasticity and were subclassified into 5
 208 clusters (**Fig. 2D**, clusters 0-4). Disease severity-associated changes seen in cohort 1 were
 209 validated in cohort 2 (**Fig. 2E**). Immature and mature neutrophil clusters were detected in
 210 both cohorts (clusters 5-6) and showed near identical marker gene expression (**Fig. 2C**).
 211 Similar to cohort 1, a prominent shift in subpopulation occupancy was observed in the
 212 monocyte clusters (**Fig. 2D+E**).

213 Based on the union of the top 50 genes for monocyte and neutrophil clusters, we found a
 214 high correlation between the independently defined functional states within the monocyte

215 compartment, and mature and immature neutrophils in cohort 1 and cohort 2 (**Fig. S2C**).
 216 Violin plot representation of important marker genes illustrated distinct phenotypic states and
 217 underscored the high similarity of the two cohorts (**Fig. S2D**).

218 Disease-severity dependent alterations of the monocyte compartment and the appearance
 219 of two LDN populations were detected in two cohorts of COVID-19 patients.

220 Predominance of HLA-DR^{hi}CD11c^{hi} inflammatory monocytes in mild and HLA-
 221 DR^{lo}CD11c^{lo}CD226⁺CD69⁺ monocytes in severe COVID-19

222 The monocyte compartment is particularly affected by COVID-19, indicated by a loss of
 223 CD14^{lo}CD16^{hi} non-classical monocytes (**Fig. 1C+D**). Disease severity-dependent shifts in
 224 monocyte activation were identified by scRNA-seq (**Fig. 2**). We further explored the
 225 phenotypic alterations of the monocyte compartment using mass cytometry (**Table S2**, panel
 226 1) on whole blood samples from COVID-19 patients with a mild or severe disease (n=8+9),
 227 patients with FLI (n=8), and age- and gender-matched controls (n=9, all collected within
 228 cohort 1, **Table S1**). Unsupervised cluster analysis using 15 surface antigens and the
 229 proliferation marker Ki67 separated the monocyte and DC compartment into 12 main cell
 230 clusters (**Fig. 3A+B**). Classical CD14^{hi}CD16⁻ monocytes displayed high heterogeneity and
 231 separated into seven main subclusters. Most classical monocytes showed high expression
 232 of activation markers CD38, CD95, and CXCR3. The four most prevalent clusters (1, 2, 5, 6)
 233 varied according to CD62L, HLA-DR, CD11c, and Ki67 expression, with CD62L and HLA-DR
 234 showing a reverse expression pattern (**Fig. 3A**). Cluster 1 displayed an activated
 235 inflammatory phenotype with high co-expression of CD11c and HLA-DR (Bernardo et al.,
 236 2018; Janols et al., 2014). In addition, we observed classical monocyte cell clusters (7, 9,
 237 10) with high CD226 and CD69 but low HLA-DR expression and thus signs of altered or
 238 alternative activation (Davison et al., 2017; Reymond et al., 2004; Vo et al., 2016). Among
 239 the HLA-DR^{lo} clusters, particularly cluster 7 showed high expression of CD34 indicative of a
 240 more immature phenotype. In contrast, the majority of CD14^{hi}CD16⁺ intermediate monocyte
 241 cell clusters showed high CD11c and HLA-DR expression.

242 Monocytes from COVID-19 patients separated from those of FLI patients and controls (**Fig.**
 243 **3B**), mainly based on elevated CD226 and CD69 expression in COVID-19. Monocytes in
 244 mild and severe COVID-19 clustered separately, and monocytes from mild COVID-19
 245 clustered closer to monocytes in FLI. FLI patients and mild COVID-19 contained higher
 246 proportions of HLA-DR^{hi}CD11c^{hi} cells (cluster 3, 11), and total HLA-DR^{hi}CD11c^{hi} monocytes
 247 were higher compared to controls and severe COVID-19, reflecting blunted monocyte
 248 activation in severe COVID-19, reminiscent of observations in sepsis (Janols et al., 2014)
 249 (**Fig. 3A,C,D**). Increased levels of activated HLA-DR^{hi}CD11c^{hi} monocytes in mild COVID-19
 250 patients was confirmed by MCFC in cohort 2 (**Fig. 3E**). In severe COVID-19, we detected
 251 increased expression of CD226 and CD69 (cluster 10) and/or decreased expression of HLA-
 252 DR, and total CD226⁺CD69⁺ monocytes were elevated compared to controls. Cluster 10
 253 expressed high levels of CD10, which is induced during macrophage differentiation (Huang
 254 et al., 2020b). Thus, an alternative activation pattern of classical monocytes appeared to be
 255 COVID-19 specific and was associated with severe disease. Besides activated lymphocytes,
 256 also monocytes upregulate CD69 expression (Davison et al., 2017), which promotes tissue
 257 infiltration and retention (Cibrián and Sánchez-Madrid, 2017). Similarly, CD226 expression
 258 on alternatively activated monocytes might also promote diapedesis and tissue infiltration

259 (Reymond et al., 2004). Together, this activation pattern may contribute to the reduction of
 260 circulating monocytes in COVID-19.

261

262 *HLA-DR^{lo}* monocytes persist in severe COVID-19

263 Next, we dissected COVID-19 associated phenotypic alterations of monocytes by scRNA-
 264 seq. Marker genes of the monocyte clusters derived from **Fig. 2A** showed that mild COVID-
 265 19 associated clusters 1 and 2 were characterized by an ISG-driven transcriptional program
 266 (**Fig. S3A**), and gene ontology enrichment analysis (GOEA) assigned these clusters to ‘type
 267 I interferon signaling pathway’ (**Fig. S3B**). A monocyte cluster marked by low expression of
 268 *HLA-DR* and high expression of *S100A12* and *CXCL8* (cluster 3, *HLA-DR^{lo}S100A^{hi}*) was
 269 strongly associated with severe COVID-19 (**Fig. S3A, 2B, S2D**). For further in-depth
 270 analysis, we subclustered the monocyte compartment of the PBMC dataset of cohort 2 (**Fig.**
 271 **2D, S3C, Table S1**) resulting in 7 subclusters (**Fig. 4a**). Cluster 1 was marked by high
 272 expression of *HLA-DRA* and *HLA-DRB1* and co-stimulatory molecule *CD83* and was
 273 therefore designated *HLA-DR^{hi}CD83^{hi}* activated inflammatory monocytes (**Fig. 4A+B,**
 274 **S3D+E**). We identified two major clusters (0, 2) and a smaller cluster 6 with low *HLA-DR*
 275 expression, which were associated with severe COVID-19 (**Fig. 4B, S3D+E**). Low *HLA-DR*
 276 expression is an established surrogate marker of monocyte dysfunction (Venet et al., 2020)
 277 which results in reduced responsiveness to microbial stimuli (Veglia et al., 2018), suggesting
 278 that cluster 0 and 6 are composed of dysfunctional monocytes. Genes of the *S100A* family
 279 were expressed in both *HLA-DR^{lo}* clusters (**Fig. 4B**), albeit to a higher degree in cluster 0
 280 (*HLA-DR^{lo}S100A^{hi}*, e.g. *S100A12*, **Fig. S2D, S3E, Table 4**). Cluster 2 monocytes expressed
 281 high levels of *SELL* (*CD62L*) and *CD163* (*HLA-DR^{lo}CD163^{hi}*, **Fig. 4B**), associated with anti-
 282 inflammatory macrophage functions (Fischer-Riepe et al., 2020; MacParland et al., 2018), as
 283 well as pre-maturation markers like *MPO* and *PLAC8* (**Fig. 4B**), recently linked to immature
 284 monocyte states in sepsis patients (Reyes et al., 2020). In line with these findings, clusters
 285 0, 2 and 6 were significantly enriched in a gene signature derived from sepsis-associated
 286 monocytes (**Fig. 4C**) (Reyes et al., 2020). Moreover, blood monocytes isolated from COVID-
 287 19 patients showed a blunted cytokine response to LPS stimulation, particularly monocytes
 288 from patients with severe COVID-19 (**Fig. 4D**). Accordingly, *HLA-DR^{lo}* monocyte clusters (0,
 289 2, 6) were detected almost exclusively in severe COVID-19 (**Fig. 4E**). We next analyzed
 290 time-dependent cluster occupancies per patient in cohort 2 (**Fig. 4E+F**). Activated *HLA-*
 291 *DR^{hi}CD83^{hi}* monocytes (cluster 1) were found in all cases of mild COVID-19, even at late
 292 time points (**Fig. 4E+F**). In contrast, *HLA-DR^{lo}CD163^{hi}* monocytes (cluster 2) were present
 293 mainly early in severe disease, while *HLA-DR^{lo}S100A^{hi}* monocytes (cluster 0) dominated the
 294 late phase of disease (**Fig. 4E+F**). Violin plots of *ISG* (**Fig. S3D**) and visualization of marker
 295 genes (**Fig. S3E**) indicated differential expression patterns of IFN signature genes in
 296 individual monocyte clusters. To reveal the kinetics of ISG expression, we plotted the
 297 expression of *ISG15* and *IFI6* in the complete monocyte population for all patients that had
 298 been sampled at least twice (**Fig. 4G**). Expression levels were highest at early time points
 299 and consistently decreased over time, clearly indicating that the IFN response in COVID-19
 300 is inversely linked to disease severity and time (**Fig. S3F+G**). In contrast, decreased
 301 expression of *HLA-DRA* and *HLA-DRB1* in severe COVID-19 is evident early on and
 302 sustained over time.

303 Transcription factor prediction indicated a STAT signaling-driven gene expression program
 304 in monocytes in COVID-19 (**Fig. 4H**), with additional regulation by CEBPD and CEBPE,
 305 which have been implicated in gene expression programs of sepsis-associated monocytes
 306 (Reyes et al., 2020). STAT3 was predicted as a specific regulator of genes enriched in *HLA-*
 307 *DR*^{lo}*CD163*^{hi} and *HLA-DR*^{lo}*S100A*^{hi} monocytes (cluster 2 and 0), in line with their
 308 immunosuppressive phenotype.

309 Taken together, dynamic changes of monocyte phenotypes were associated with COVID-19
 310 disease severity and time after onset of disease.

311

312 Low-density neutrophils emerge in severe COVID-19 patients indicative of
 313 emergency myelopoiesis

314 PBMC derived from blood samples of patients with severe COVID-19 contained two distinct
 315 clusters of LDN (**Fig. 2A**, clusters 5, 6; **Fig. 2D**, clusters 5, 6). LDN were slightly more
 316 frequent in cohort 1, and we analyzed these cells in more detail. Subsampling of all LDN
 317 (**Fig. 5A**, **Table S1**) and re-clustering the cells revealed 8 transcriptionally distinct cell
 318 clusters (**Fig. 5A+B**, **Table S4**). Based on published markers for pro- and pre-neutrophils,
 319 and mature neutrophils (Kwok et al., 2020; Ng et al., 2019; Scapini et al., 2016) we identified
 320 cluster 4 and 6 as *CD81*⁺*SPN*(*CD43*)⁺*FUT4*(*CD15*)⁺*CD63*⁺*CEACAM8*(*CD66b*)⁺ pro-
 321 neutrophils, clusters 3 and 5 as *ITGAM*(*CD11b*)⁺*CEACAM8*(*CD66b*)⁺*CD101*⁺⁻ pre-
 322 neutrophils and the remaining clusters as mature neutrophils (**Fig. S4A**). Accordingly, pro-
 323 and pre-neutrophils were enriched for transcriptional signatures of neutrophil progenitors
 324 derived from published single-cell data (**Fig. 4C**) (Pellin et al., 2019; Popescu et al., 2019),
 325 and pro-neutrophils in cluster 4 and 6 showed the highest proportion of cells with a
 326 proliferative signature (**Fig. S4B**). Clusters 0, 1, 2 (originally in cluster 4 in **Fig. 2A**)
 327 expressed mature neutrophil markers *FCGR3B* (*CD16*) and *MME* (*CD10*) (**Fig. S4A**).

328 Differential gene expression analysis for each cluster revealed extensive phenotypic
 329 heterogeneity within the LDN compartment (**Fig. 5B**). LDN mainly arise under pathological
 330 conditions, such as severe infection and sepsis in the context of emergency myelopoiesis
 331 (Schultze et al., 2019), and they have been associated with dysfunctional immune
 332 responses, marked by combined immunosuppression and inflammation (Silvestre-Roig et
 333 al., 2019). While LDN in cluster 1 expressed numerous ISGs (*ISG15*, *IFITM1/3* and *RSAD2*),
 334 cluster 4 (pro-neutrophils) expressed genes (e.g. *MPO*, *ELANE*, *PRTN3*) that are involved in
 335 neutrophil extracellular trap formation (Stiel et al., 2018; Thomas et al., 2014; You et al.,
 336 2019) among other functions and that have been associated with sepsis (Ahmad et al.,
 337 2019; Carbon et al., 2019; Silvestre-Roig et al., 2019). Both pre-neutrophil clusters
 338 expressed *PADI4*, another co-factor in NETosis (Leshner et al., 2012) (**Fig. 5D**). NETs have
 339 recently been implicated in the pathogenesis of COVID-19 (Barnes et al., 2020; Zuo et al.,
 340 2020). Both pre-neutrophils (clusters 3 and 5) and pro-neutrophils expressed genes
 341 including *CD24*, *OLFM4*, *LCN2*, and *BPI*, previously associated with poor outcome in sepsis
 342 (**Fig. 5B, S4A**) (Kangelaris et al., 2015).

343 All LDNs also expressed high levels of alarmins *S100A8* and *S100A9* (**Fig. 5D**), whereas
 344 other *S100* genes (e.g. *S100A4*, *S100A12*) were strongly induced in selected neutrophil

345 clusters. Finally, known inhibitors of T cell activation, namely *CD274* (PD-L1) and *Arginase 1*
 346 (*ARG1*) (Bronte et al., 2003; Li et al., 2018) were highly expressed in neutrophils in COVID-
 347 19 patients (**Fig. 5E**). *ARG1*⁺ neutrophils in sepsis patients were shown to deplete arginine
 348 and constrain T cell function in septic shock (Darcy et al., 2014), and were predictive of the
 349 development of nosocomial infections (Uhel et al., 2017). Mature *CD274*(PD-L1)⁺ neutrophils
 350 (clusters 0) have been attributed suppressive functions in various conditions including HIV-1
 351 infection (Bowers et al., 2014), cancer (Chun et al., 2015) and in lymph nodes (Castell et al.,
 352 2019), spleen (Langereis et al., 2017) and blood after LPS exposure (de Kleijn et al., 2013).
 353 *ARG1*⁺ cells were mainly immature neutrophils (clusters 3-6) and did not overlap with *CD274*
 354 (PD-L1) expressing cells, indicating different populations of dysfunctional and potentially
 355 suppressive neutrophils in severe COVID-19.

356 LDNs recovered from PBMC fractions of COVID-19 patients revealed the presence of
 357 dysfunctional neutrophils and pointed towards multiple potentially deleterious pathways
 358 activated in severe COVID-19.

359

360 Persistent increase of activated neutrophil precursors and PD-L1⁺ neutrophils in
 361 severe COVID-19

362 Alterations of the neutrophil compartment were further interrogated by mass cytometry of
 363 whole blood samples of COVID-19 patients (n=8 mild + 9 severe, cohort 1), FLI patients
 364 (n=8), and age- and gender-matched controls (n=9) (**Table S1**), using a panel designed to
 365 detect myeloid cell maturation and activation states as well as markers of
 366 immunosuppression or dysfunction (**Table S2**). Unsupervised clustering analysis of all
 367 neutrophils in all samples revealed 10 major clusters (**Fig. 6A**) of immature (cluster 2, 5, 6,
 368 7), mature (cluster 1, 3, 4) and remaining clusters of low abundancy (cluster 8, 9, 10). Based
 369 on their differential expression of CD11b, CD16, CD24, CD34 and CD38, clusters 5 and 6
 370 were identified as pro-neutrophils and cluster 2 as pre-neutrophils (Kwok et al., 2020; Ng et
 371 al., 2019). The fourth immature cell cluster (7) showed very low expression of CD11b and
 372 CD16, reminiscent of pro-neutrophils, but lacking CD34, CD38 and CD24 (**Fig. 6A**),
 373 suggesting a hitherto unappreciated pro-neutrophil-like population. The mature neutrophils
 374 segregated into non-activated (cluster 1), partially activated (cluster 3) and highly activated
 375 cells (cluster 4), based on the loss of CD62L and upregulation of CD64, as well as signs of
 376 proliferative activity (Ki67⁺) (**Fig. 6A**).

377 Neutrophils from COVID-19 patients clearly separated from those of controls and also FLI
 378 patients in UMAP analysis (**Fig. 6B**), and neutrophils in patients with severe COVID-19 were
 379 distinct from those of patients with mild disease (**Fig. 6B**). Cells from control donors
 380 accumulated in areas enriched for mature non-activated cells (cluster 1) and immature pre-
 381 neutrophil-like cells (cluster 2). In contrast, neutrophils from FLI patients were mainly mature
 382 non-activated (cluster 1) and mature highly activated (cluster 4) cells. Neutrophils from
 383 COVID-19, particularly from patients with severe disease primarily occupied immature pre-
 384 and pro-neutrophil-like clusters. Plotting cell cluster-specific surface marker expression onto
 385 the UMAPs (**Fig. 6C**) as well as statistical analyses of cell cluster distribution and surface
 386 marker expression among different patient groups supported these observations (**Fig.**
 387 **6D+E**). Samples from FLI patients contain a high proportion of highly activated mature

388 neutrophils, but barely any immature neutrophils. In contrast, severe COVID-19 is
 389 associated with the appearance of immature pre- and pro-neutrophils (**Fig. 6D+6E**).
 390 Interestingly, immature cell clusters in severe COVID-19 showed signs of recent activation
 391 like upregulation of CD64 (Mortaz et al., 2018), RANK and RANKL (Riegel et al., 2012), as
 392 well as reduced CD62L expression (Mortaz et al., 2018). In addition to loss of CD62L,
 393 immature and mature neutrophils from severe COVID-19 showed elevated PD-L1
 394 expression compared to control samples (**Fig. 6E**). Indeed, CD62L downregulation and high
 395 PD-L1 expression has been frequently associated with suppressive function of neutrophils
 396 and granulocytic myeloid derived suppressor cells (gMDSCs) (Bronte et al., 2016; Cassetta
 397 et al., 2019; Kamp et al., 2012; Pillay et al., 2012; Tak et al., 2017; Testa et al., 2004;
 398 Younos et al., 2015). Interestingly, a recent study described a high abundance of similar
 399 immature and dysfunctional CD64⁺ and PD-L1⁺ neutrophils in sepsis patients (Meghraoui-
 400 Kheddar et al., 2020).

401 Thus, SARS-CoV-2 infection induces major alterations in the neutrophil compartment. While
 402 neutrophils in FLI patients display a mature activated phenotype, a release of immature
 403 neutrophils with phenotypic signs of immunosuppression and dysfunction is a hallmark of
 404 severe COVID-19.

405 We next assessed the dynamics of the changes within the myeloid cell compartment over
 406 time. We grouped samples according to collection time as 'early' (within the first 10 days) or
 407 late (during the following 20 days) after onset of symptoms. In both cohorts, we observed a
 408 tendency towards (cohort 1) or significantly higher (cohort 2) proportions of granulocytes in
 409 severe vs. mild COVID-19 patients, both at early and late time points (**Fig. S5A**). We
 410 observed a persistent release of immature neutrophils (e.g. cluster 6) in severe COVID-19
 411 (**Fig. S5B**) showing high expression of CD64 and PD-L1, but downregulation of CD62L as a
 412 sign of activation, dysfunction and immunosuppression (**Fig. S5C**). In addition, severe
 413 COVID-19 patients show further increased frequencies of mature, partially activated
 414 neutrophils (cluster 3) at later time periods (**Fig. S5B**). Thus, the neutrophil compartment of
 415 severe COVID-19 patients is characterized by a combination of persistent signs of
 416 inflammation and immunosuppression, which is reminiscent of long-term post-traumatic
 417 complications (Hesselink et al., 2019).

418 We also analyzed time-dependent phenotypic changes in the monocyte compartment by
 419 mass cytometry. Non-classical monocytes started to recover in COVID-19 patients during
 420 the later stages of the disease (**Fig. S5A**). HLA-DR^{hi}CD11c^{hi} monocyte cell clusters also
 421 declined at later time points in mild COVID-19 (**Fig. S5D,E,F**), which correlates well with the
 422 longitudinal changes of *IFI6* and *ISG15* as well as *HLA-DRA*, and *HLA-DRB1* expression
 423 profiles (**Fig. 4G+S3F**). In contrast, overall proportions of HLA-DR^{hi}CD11c^{hi} monocytes in
 424 severe COVID-19 remained low throughout the course of the disease. Proportions of CD10^{hi}
 425 macrophage-like cluster 10 and CD226⁺CD69⁺ monocytes were generally higher at later
 426 stages in severe COVID-19, which resembled the kinetics of *HLA-DR^{lo}S100A^{hi}* monocytes
 427 identified by scRNA-seq (**Fig. 4F**). This indicates a prolonged alternative activation of
 428 monocytes in severe COVID-19 (**Fig. S5E**).

429

430 Single-cell transcriptomes of whole blood reveal suppressive-like neutrophils in
 431 severe COVID-19

432 Whole blood CyTOF analysis (cohort 1) clearly indicated very distinct phenotypic alterations
 433 of the neutrophil compartment in mild and severe forms of COVID-19. To further delineate
 434 the underlying transcriptional programs, we performed scRNA-seq analysis on fresh whole
 435 blood samples of 23 individuals (34 samples, cohort 2, **Table S1**). Integrated visualization of
 436 all samples of cohort 2 (fresh/frozen PBMC, fresh whole blood, 229,731 cells, **Fig. S6A**)
 437 revealed the expected blood leukocyte distribution, including granulocytes (**Fig. 7A, S6A**,
 438 **Table S4**). Cell type distribution identified by scRNA-seq profiles (**Fig. S6B**) strongly
 439 correlated with MCFC characterization of the same samples (**Fig. S6C**). For further analysis
 440 of the granulocyte compartment, we first combined the whole blood samples with the fresh
 441 PBMC to guide the clustering of all major immune cells resulting in a total of 122,954 cells
 442 (**Fig 7A**). From these samples, we identified all neutrophil clusters and extracted the cells
 443 derived from whole blood for subsampling, which revealed a structure of 9 clusters
 444 (n=58,383 cells, **Fig. 7B+C**).

445 Using marker- and data-driven approaches as applied to LDN (**Fig. 5D, S4A**), we identified
 446 *FUT4*(CD15)⁺*CD63*⁺*CD66b*⁺ pro-neutrophils, *ITGAM*(CD11b)⁺*CD101*⁺ pre-neutrophils, along
 447 with 7 mature neutrophil clusters (**Fig. 7B-D, S6D, Table S4**). Heterogeneous expression of
 448 various markers involved in mature neutrophil function including *CXCR2*, *FCGR2A* (CD32),
 449 *FCGR1A* (CD64) or *MME* (CD10), pointed towards distinct functionalities within the
 450 neutrophil compartment (**Fig. 7E, S6D+E**). Seven of the nine 9 neutrophil clusters identified
 451 in whole blood in cohort 2, could also be mapped to the fresh PBMC transcriptomes in
 452 cohort 1 (**Fig. S6F**), indicating that scRNA-seq of fresh PBMC in COVID-19 patients reveals
 453 relevant parts of the neutrophil space. The transcriptional phenotype of pro- and pre-
 454 neutrophils (cluster 8+9) was corroborated in cohort 2 (**Fig. 7B-D, S6D**).

455 Heatmap and UMAP visualization of the cell type distribution identified pro- and pre-
 456 neutrophils mainly at late time points in severe COVID-19 (**Fig. 7F-G**). Furthermore, mature
 457 neutrophils with a high IFN-signature (cluster 1) were associated with severe COVID-19
 458 (**Fig. 7E, S6G**). This cluster was also enriched for markers identified by CyTOF as
 459 differentially expressed in patients with severe COVID-19 (**Fig. 6**), such as elevated
 460 expression of *CD274* (PD-L1) and *FCGR1A* (CD64) (**Fig. 7H**). In addition to *CD274*, cells in
 461 cluster 1 expressed genes indicative of a potentially suppressive or anti-inflammatory state,
 462 including *ZC3H12A* (**Fig. 7E**), which is known to suppress hepatitis C virus replication and
 463 virus-induced pro-inflammatory cytokine production (Lin et al., 2014). Cluster 2 was also
 464 enriched for cells from COVID-19 patients, mainly from severe but also mild cases (**Fig. 7F-**
 465 **G**).

466 Gene signatures from granulocytic MDSC (Bayik et al., 2020) and *CD274*(PD-L1)⁺
 467 neutrophils after LPS exposure (de Kleijn et al., 2013), both shown to be
 468 immunosuppressive, were enriched in clusters 1, 2 and 6, which mainly harbor cells from
 469 severe COVID-19. This indicates a suppressive functionality of these cells in severe COVID-
 470 19 (**Fig. 7I**). Predictions of transcription factor (TF)-based regulation of the cluster-specific
 471 gene signatures separated mature neutrophils from patients with severe COVID-19 (cluster
 472 1) and control patients (cluster 0, **Fig. 7J**). IFN-response genes are mainly controlled by
 473 STAT and IRF TFs, whereas the transcriptional signature of cluster 0 is mainly driven by the

474 CEBP TF family. The TF network underlying the transcriptional difference in pro-neutrophils
 475 is mainly driven by E2F family members and pre-neutrophils mainly depend on ETS TFs
 476 (**Fig. S6H**).

477 Pseudotime analysis strongly supported the differentiation trajectory from pro-neutrophils
 478 (cluster 8) via pre-neutrophils (cluster 6) to mature neutrophils in cluster 2 and 1 (**Fig. S6I-J**).
 479 Particularly *CD274* (PD-1L) was enriched in cluster 1 compared to cluster 2, supporting the
 480 potential of neutrophils to progress towards a suppressive phenotype in severe COVID-19
 481 (**Fig. S6J**). Interestingly, *CD177* is expressed in pre-neutrophils and persisting in cluster 1
 482 further highlighting the newly emerging character of this cluster (Volkmann et al., 2020).

483 Finally, we studied whether the persistent emergence of immature, potentially dysfunctional
 484 neutrophils in severe COVID-19 patients can be captured under routine diagnostic
 485 conditions. Therefore, samples of 32 COVID-19 patients (**Table S1**, cohort 1) were
 486 characterized by routine hematology analyses using a clinical flow cytometry system
 487 (Sysmex analyzer). Indeed, the assumption of rescue myelopoiesis in severe COVID-19 was
 488 supported by significantly higher counts in the population of immature granulocytes (IG,
 489 representing promyelocytes, myelocytes, and metamyelocytes) in this patient group (**Fig.**
 490 **7K**). We also found significant differences in the neutrophil compartment, when analyzing
 491 the width of dispersion with respect to granularity, activity, and cell volume defined as NE-
 492 WX, NE-WY and NE-WZ, respectively. As compared to patients with mild course, severely ill
 493 patients displayed increases in width of dispersion of activity and cell volume as surrogates
 494 for increased cellular heterogeneity, immaturity and dysregulation in severe COVID-19 (**Fig.**
 495 **7K**), resembling previously described alterations in sepsis patients (Stiel et al., 2016).
 496 Furthermore, neutrophils of severe COVID-19 patients were partially dysfunctional as their
 497 oxidative burst upon stimulation with standardized stimuli (*E.coli* or PMA) was strongly
 498 impaired in comparison to control and mild COVID-19 neutrophils, whereas phagocytic
 499 activity was preserved (**Fig. 7L, Table S1**).

500 Collectively, the neutrophil compartment in peripheral blood of severe COVID-19 patients is
 501 characterized by the appearance of LDN, *FUT4*(CD15)⁺*CD63*⁺*CD66b*⁺ pro-neutrophils, and
 502 *ITGAM*(CD11b)⁺*CD101*⁺ pre-neutrophils, reminiscent of emergency myelopoiesis, as well as
 503 *CD274*(PD-L1)⁺*ZC3H12A*⁺ mature neutrophils reminiscent of gMDSC-like cells, which might
 504 exert suppressive or anti-inflammatory functions.

505 Discussion

506 SARS-CoV-2 infection generally causes mild disease in the majority of individuals, however
 507 about 10-20% of COVID-19 patients progress to severe disease with pneumonia and
 508 respiratory failure. The reported case-fatality rates among patients with critical illness and
 509 respiratory failure vary, with a mean of approximately 25% (Quah et al., 2020). Dysregulated
 510 immune responses have been described in patients with severe COVID-19 (Chua et al.,
 511 2020; Giamarellos-Bourboulis et al., 2020; Lucas et al., 2020; Merad and Martin, 2020;
 512 Messner et al., 2020; Wei et al., 2020; Zhou et al., 2020b). Hence, detailed knowledge of the
 513 cellular and molecular processes that drive progression from mild disease to potentially fatal
 514 courses of COVID-19 is urgently needed to identify predictive biomarkers and therapeutic
 515 targets.

516 Here, we employed four complementary technologies at single-cell resolution to assess
 517 alterations in the systemic immune response in mild or severe courses of COVID-19. We
 518 analyzed a total of 53 patients (161 samples) from two independent cohorts collected at two
 519 university medical centers in Germany (Kurth et al., 2020). Combining single-cell
 520 transcriptomics with single-cell proteomics, using different technological platforms in two
 521 independent patient cohorts provided a detailed view of the systemic immune responses in
 522 COVID-19 and allowed for cross-validation and in-depth interrogation of key findings. The
 523 results were further supported by additional routine diagnostics lab measurements and
 524 functional assays, linking the results of the exploratory investigations to functional
 525 phenotypes and clinically relevant diagnostics.

526 This multipronged approach revealed drastic changes within the myeloid cell compartment
 527 during COVID-19, particularly in patients with a severe course of disease. Early activation of
 528 HLA-DR^{hi}CD11c^{hi} / HLA-DR^{hi}CD83^{hi} monocytes with a strong antiviral IFN-signature was a
 529 hallmark of mild COVID-19, which receded during the natural course of disease. In contrast,
 530 HLA-DR^{lo} dysfunctional monocytes along with clear evidence of emergency myelopoiesis
 531 with release of immature neutrophils including pro- and pre-neutrophils into the circulation
 532 marked severe COVID-19. Furthermore, we identified neutrophils in severe COVID-19 with
 533 transcriptional programs reminiscent of dysfunction and immunosuppression not observed in
 534 controls or patients with mild COVID-19. Thus, defective monocyte activation and
 535 dysregulated myelopoiesis may contribute to severe disease course and ARDS development
 536 (Middleton et al., 2020).

537 Previous immunophenotyping studies have reported an increase of inflammatory monocytes
 538 with a strong IFN-response in COVID-19 (Liao et al., 2020; Merad and Martin, 2020; Zhou et
 539 al., 2020b). Mononuclear phagocytes and neutrophils appear to dominate inflammatory
 540 infiltrates in the lungs, and resident alveolar macrophages are replaced by inflammatory
 541 monocyte-derived macrophages in patients with severe COVID-19 (Chua et al., 2020; Liao
 542 et al., 2020). Here, we report substantial time- and disease severity-dependent alterations of
 543 the monocyte compartment in COVID-19. Marked depletion of CD14^{lo}CD16^{hi} non-classical
 544 monocytes observed in all COVID-19 patients, but not in patients with SARS-CoV-2 negative
 545 FLI (**Fig. 1D**), is in line with previous reports on COVID-19, and other severe viral infections
 546 (Lüdtke et al., 2016; Naranjo-Gómez et al., 2019). Single-cell proteomics and transcriptomics
 547 revealed a transient increase in highly activated CD14⁺HLA-DR^{hi}CD11c^{hi} (HLA-DRA^{hi}CD83^{hi})

monocytes in mild COVID-19. This was similar in patients presenting with common cold or FLI, but absent in severe COVID-19 (**Fig. 3/4**). In contrast, in severe COVID-19, monocytes showed low expression of HLA-DR, and high levels of *MAFB*, *PLBD1* and *CD163*, all of which are associated with anti-inflammatory macrophage functions (Bronte et al., 2016; Cuevas et al., 2017; Fischer-Riepe et al., 2020; MacParland et al., 2018). Low HLA-DR expression on monocytes is an established surrogate marker of immunosuppression in sepsis (Venet et al., 2020). Elevated HLA-DR^{lo} monocytes have been associated with an increased risk of infectious complications after trauma (Hoffmann et al., 2017) and fatal outcome in septic shock (Monneret et al., 2006). Indeed, the *HLA-DR^{lo}CD163⁺* monocytes showed enrichment of genes associated with poor prognosis in sepsis patients, including *PLAC8* (Maslove et al., 2019), and *MPO* (Schrijver et al., 2017) (**Fig. 4B**). In line with this dysfunctional phenotype, *PLAC8* was recently shown to suppress production of IL-1 β and IL-18 (Segawa et al., 2018). In fact, we observed that inflammatory cytokine production, including IL-1 β release, was impaired in monocytes from patients with severe COVID-19 (**Fig. 4**). CD14⁺HLA-DR^{lo} monocytes have also been implicated with immunosuppression in cancer patients (Bronte et al., 2016; Mengos et al., 2019; Meyer et al., 2014). While exhibiting anti-inflammatory features, especially in the early stages of severe disease (**Fig. S3C-F**), persistently high expression of CD226 and CD69 may promote tissue infiltration and organ dysfunction (Davison et al., 2017; Reymond et al., 2004; Vo et al., 2016).

Acute pathological insults, such as trauma or severe infections, trigger a process referred to as emergency myelopoiesis to replenish functional granulocytes and other hematopoietic cells. Emergency myelopoiesis is characterized by the mobilization of immature myeloid cells, which are often linked to immunosuppressive functions (Loftus et al., 2018; Schultze et al., 2019). In fact, emergence of suppressive myeloid cells including neutrophils, often referred to as granulocytic MDSCs, has been observed during sepsis and severe influenza (Darcy et al., 2014; Loftus et al., 2018; Sander et al., 2010; De Santo et al., 2008). LDN in PBMC fractions in severe COVID-19 contained immature neutrophils, including pro- and pre-neutrophils, which was not observed in mild cases (**Fig. 5**). These immature LDN showed a surface marker and gene expression profile reminiscent of granulocytic MDSCs including genes such as *S100A12*, *S100A9*, *MMP8*, *ARG1* (Uhel et al., 2017), and *OLFM4*, which has been recently associated with immunopathogenesis in sepsis (Alder et al., 2017). Emergence of pro-neutrophils in severe COVID-19 was also detected by single-cell proteomics on whole blood samples. Strikingly, both immature and the mature neutrophils showed increased expression of CD64 and PD-L1 (**Fig. 6+S5**), similar to recently described alterations in sepsis (Meghraoui-Kheddar et al., 2020). In addition to the altered phenotype, we also observed an altered functionality. Neutrophils from patients with severe COVID-19 showed an impaired oxidative burst response, while their phagocytic capacity was preserved (**Fig. 7**).

Single-cell transcriptomics of whole blood samples revealed mature activated neutrophils in both mild and severe COVID-19 (**Fig. 7B**, cluster 2), however, expression of *CD274* (PD-L1) was only found in severe COVID-19 (cluster 1), and it increased in later stages of the disease. Expression of PD-L1 on neutrophils has been associated with T cell suppression (Bowers et al., 2014; Castell et al., 2019; de Kleijn et al., 2013; Langereis et al., 2017), suggesting that neutrophils in severe COVID-19 might exert suppressive functions. Furthermore, the expression of *CD177* on mature activated neutrophils and the identification of genes associated with anti-inflammatory functions (*CD274*, *ZC3H12A*) suggest a model in

594 which neutrophils emerging prematurely from the bone marrow are programmed towards an
 595 anti-inflammatory, or even suppressive phenotype in severe COVID-19. The transcriptional
 596 programs induced in immature neutrophils, including pro- and pre-neutrophils, as well as in
 597 COVID-19-associated mature neutrophil clusters, align with other observations in severe
 598 COVID-19 patients, including increased NET formation (Barnes et al., 2020; Zuo et al.,
 599 2020), coagulation (Klok et al., 2020; Pfeiler et al., 2014) and immunothrombosis (Stiel et al.,
 600 2018; Xu et al., 2020). In contrast, these transcriptional programs were not observed in
 601 patients with mild COVID-19 or in SARS-CoV-2 negative controls, even though the latter
 602 exhibited a range of comorbidities (e.g. COPD, type II diabetes).

603 Thus, defective or repressed monocyte activation combined with dysregulated myelopoiesis
 604 may cause a deleterious loop of continuous tissue inflammation and ineffective host
 605 defense.

606 ***Limitations of the study and future directions***

607 The pathophysiological consequences of the dysfunctional phenotype of myeloid cells in
 608 severe COVID-19 remain unclear at this stage. It is, however, highly likely that they
 609 contribute to immunosuppression in critically ill patients, potentially leading to insufficient
 610 host defense, disbalanced inflammation and increased susceptibility to superinfections.
 611 While our dual cohort study design provided robust and reproducible results concerning the
 612 alterations within the myeloid compartment in COVID-19, it is too early to speculate on the
 613 underlying mechanisms driving this response, such as genetics, lifestyle, comorbidities,
 614 environmental factors, or initial viral load (Ellinghaus et al., 2020). Utilizing the herein
 615 established transcriptional and functional phenotypes of the myeloid cell compartment, it will
 616 likely be possible to estimate the potential contribution of the causes mentioned above in
 617 larger clinical studies in the future and to address potential upstream events of immune
 618 dysregulation in preclinical model systems as they become available (Bao et al., 2020;
 619 Cohen, 2020). Indeed, in future studies it will be interesting to dissect, whether the myeloid
 620 subsets in COVID-19 are anti-inflammatory or even capable of suppressing other immune
 621 cells, and which pathways might be mainly involved. Clearly, PD-L1 is a prime candidate
 622 (Bowers et al., 2014; Castell et al., 2019; de Kleijn et al., 2013; Langereis et al., 2017).

623 Collectively, our data link a striking appearance of immature and dysfunctional cells, in both
 624 the monocyte and neutrophil compartment, to disease severity in COVID-19. Consequently,
 625 the development of treatments and prevention strategies for severe COVID-19 may benefit
 626 from insights gained in other fields such as oncology, which have successfully applied
 627 therapies targeting suppressive myeloid cells.

628 **Acknowledgements**

629 We thank Michael Kraut, Heidi Theis, Gudrun Hack, Claudia Finnemann, Magdalena Bürkle,
 630 Moritz Vollgraf and Wibke Groenewald for perfect technical assistance.

631

632 **Consortia**633 **Deutsche COVID-19 Omics Initiative (DeCOI)**

634 Angel Angelov, Robert Bals, Alexander Bartholomäus, Anke Becker, Daniela Bezdan, Ezio
 635 Bonifacio, Peer Bork, Thomas Clavel, Maria Colome-Tatche, Andreas Diefenbach,
 636 Alexander Dilthey, Nicole Fischer, Konrad Förstner, Julia-Stefanie Frick, Julien Gagneur,
 637 Alexander Goesmann, Torsten Hain, Michael Hummel, Stefan Janssen, Jörn Kalinowski,
 638 René Kallies, Birte Kehr, Andreas Keller, Sarah Kim-Hellmuth, Christoph Klein, Oliver
 639 Kohlbacher, Jan O. Korbel, Ingo Kurth, Markus Landthaler, Yang Li, Kerstin Ludwig, Oliwia
 640 Makarewicz, Manja Marz, Alice McHardy, Christian Mertes, Markus Nöthen, Peter Nürnberg,
 641 Uwe Ohler, Stephan Ossowski, Jörg Overmann, Silke Peter, Klaus Pfeffer, Anna R. Poetsch,
 642 Alfred Pühler, Nikolaus Rajewsky, Markus Ralser, Olaf Rieß, Stephan Ripke, Uliisses Nunes
 643 da Rocha, Philip Rosenstiel, Antoine-Emmanuel Saliba, Leif Erik Sander, Birgit Sawitzki,
 644 Philipp Schiffer, Eva-Christina Schulte, Joachim L. Schultze, Alexander Sczyrba, Oliver
 645 Stegle, Jens Stoye, Fabian Theis, Janne Vehreschild, Jörg Vogel, Max von Kleist, Andreas
 646 Walker, Jörn Walter, Dagmar Wieczorek, John Ziebuhr

647

648 **Funding**

649 This work was supported by the German Research Foundation (DFG, SFB-TR84
 650 #114933180 to LES, SH, AH, NS, CD; INST 37/1049-1, INST 216/981-1, INST 257/605-1,
 651 INST 269/768-1 and INST 217/988-1, INST 217/577-1 to JLS; SFB TR57, SPP1937 to JN;
 652 GRK2157 to A-ES, ME 3644/5-1 to HEM.); the Berlin University Alliance (BUA, PreEP-
 653 Corona grant to LES, VC and CD), the Berlin Institute of Health (BIH, grant to LES, AH, CD);
 654 the HGF grant sparse2big, the EU projects SYSCID (grant number 733100), and ERA CVD
 655 (grant number 00160389) to JLS.; the DZIF (TTU 04.816, 04.817 to JN); the Hector-
 656 Foundation (M89 to JN); the Helmholtz Association of German Research Centres to A-ES;
 657 the EU projects ONE STUDY (grant number 260687 to BS), BIO-DrIM (305147 to BS) and
 658 INsTRuCT (grant number 860003 to BS), the German Federal Ministry of Education and
 659 Research (BMBF, project RAPID to CD, SH, AH), and a Charité ³R project to BS and SH;
 660 Radboud University Medical Centre Hypatia Grant (2018 to YL).

661

662 **Author contributions**

663 Conceptualization: JS-S, NR, KB, BK, LB, EDD, FK, JLS, ACA, YL, JN, BS, A-ES, LES.
664 Methodology: JS-S, DP, TK, SB, LB, EDD, MG, DW, MB, TSK, AS, OD, HM, ARS, CC, DK, EV,
665 CJX, AD, CT, SH, CLG, ML, EW, TU, MB, RG, CD, CVK, KH. Software/data analysis: JS-S, NR,
666 KB, SS, BZ, TK, LB, AS, TU, MB. Investigation: JS-S, KB, TP, AH, MH, JLS, ACA., MW, YL, JN, BS,
667 A-ES, LES Biospecimen/ enzyme resources: BK, SB, MP, SH, HMR, FM, AU, LBJ, LJ, CRG, PG,
668 MS, CD-H, NN, KK, RT, VC, JR, KMK, MTV, GR, FK, JN, MW. Writing – Original Draft: JS-S, NR,
669 KB, LB, EDD, CM, JLS, ACA, YL, JN, BS, A-ES, LES. Writing – Review & Editing: JS-S, NR, MW,
670 KB, LB, EDD, TP, MB, TSK, SH, AH, MS, HDV, CD, NS, CVK, FK, JLS, ACA, YL, JN, BS, A-ES, LES.

671 **Declaration of interests**

672 The authors do not declare any conflict of interest

673

674 Main figure titles and legends

675 **Figure 1. Cohort definition and single-cell multi-omics analysis strategy**

676 **A**, Pipeline for control and COVID-19 blood samples of the two cohorts (see also **Table S1**).
 677 Whole blood samples were subjected to red blood cell (RBC) lysis and processed for CyTOF
 678 mass cytometry (two antibody panels), multi-color flow cytometry (MCFC), or scRNA-seq
 679 (BD Rhapsody). PBMC were isolated by density centrifugation and processed directly or
 680 after frozen storage, labeled with cell hashing antibodies and loaded on droplet-based (10x)
 681 or microwell-based (BD Rhapsody) scRNA-seq platforms. Box (bottom left): Number of
 682 subjects in each cohort. Boxes (on the right): Number of samples analyzed with each
 683 technique.

684 **B**, Number of samples per technique summarized across cohorts, divided by disease
 685 severity according to WHO ordinal scale and by the time after onset of first symptoms (early:
 686 day 0-10, late: > day 11).

687 **C**, UMAP of CD45⁺ leukocytes, down-sampled to 70,000 cells, from mass cytometry using
 688 antibody panel 2 (30 markers, Table S2). Cells are colored according to donor origin
 689 (blue=age-matched controls, grey=FLI, yellow=mild COVID-19, red=severe COVID-19) and
 690 major lineage subtypes.

691 **D**, Box and whisker (10-90 percentile) plots of major cell lineage composition in whole blood
 692 from FLI (n=8), COVID-19 patients with mild (n=8) or severe disease (n=9), age-matched
 693 controls measured by mass cytometry (ctrl CyTOF, n=9) or by flow cytometry (ctrl flow,
 694 n=19) (Kverneland et al., 2016). Kruskal-Wallis and Dunn's multiple comparison test
 695 *p<0.05, **p<0.01, ***p<0.001, ****p<0.0001. n.a. = not available.

696

697 **Figure 2. scRNA-seq of PBMC from patients of the two independent cohorts**

698 **A**, UMAP visualization of scRNA-seq profiles (10x, cohort 1) of 99,049 PBMC from 49
 699 samples (8 mild, 10 severe patients, different time points) and 22 control samples colored
 700 according to cell type classification (Louvain clustering), reference-based cell-type
 701 annotation, and marker gene expression (**Table S4**).

702 **B**, UMAP shown in (A) colored according to disease severity (yellow = mild COVID-19, red =
 703 severe COVID-19).

704 **C**, Dot plots of the intersection of the top 20 marker genes sorted by average log fold change
 705 determined for the indicated myeloid cell subsets in the PBMC data sets of both cohorts.

706 **D**, UMAP visualization of scRNA-seq profiles (BD Rhapsody, cohort 2) of 139,848 PBMC (50
 707 samples of 8 mild, 9 severe COVID-19; 14 samples of 13 controls; different time points),
 708 coloring as in (A) (see also **Fig. S2A, Table S4**).

709 **E**, Box plots of percentages of cell subsets of total PBMC (per patient). Boxes are colored
 710 according to disease group and dots according to the respective cohort of the sample.

711 Dirichlet-multinomial regression adjusted with the Benjamini-Hochberg method, * $p<0.05$,
 712 ** $p<0.01$, *** $p<0.001$)

713

714 **Figure 3. CD11c^{lo} and HLA-DR^{lo} but CD226⁺CD69⁺ monocytes in severe COVID-19**

715 **A**, Heatmap of CyTOF data (antibody panel 1, cohort 1) covering monocytes and DCs. Main
 716 cell, as defined by the numbers 1 to 12, and individual cell clusters are displayed in columns
 717 and marker identity is indicated in rows. MSI = marker staining intensity respective
 718 expression level, significance level for the following comparisons i) controls (ctrl, n=9) vs.
 719 COVID-19 (mild & severe, n=17, first row), ii) mild (n=8) vs. severe (n=9, second row), iii) FLI
 720 (n=8) vs. mild COVID-19 (n=8, third row) as well as iv) controls (ctrl, n=9) vs. FLI (n=8) are
 721 indicated using a grey scale on top of the heatmap (p-value scale next to heatmap). COVID-
 722 19 samples collected between day 4 and 13 post symptom onset (= first day of sample
 723 collection per patient). Abundance testing via generalized mixed effects models and multiple
 724 comparison adjustment using the Benjamini-Hochberg procedure and an FDR-cutoff of 5%
 725 across all clusters/subsets and between-group comparisons.

726 **B**, UMAP of monocytes and DCs, down-sampled to 70,000 cells, (39 markers, Table S2).
 727 Cells are colored according to main cell clusters (1 to 12, colors as in A) as defined in the
 728 table, donor origin (blue = controls, grey = FLI, yellow = mild COVID-19, red = severe
 729 COVID-19) and expression intensity of HLA-DR, CD11c, CD226 and CD69.

730 **C**, Box and whisker (10-90 percentile) plots of main monocyte cluster 1, 10 (CD14^{hi}CD16⁻
 731 classical monocytes), 11 and 3 (CD14^{hi}CD16⁺ intermediate monocytes) determined by mass
 732 cytometry (whole blood, cohort 1): controls (n=9), FLI patients (n=8), COVID-19 patients
 733 (mild, n=8; severe, n=9). Abundance testing via R multcomp and lsmeans packages
 734 adjusted using the Benjamini-Hochberg procedure and an FDR-cutoff of 5% across all
 735 clusters/subsets and between-group comparisons.

736 **D**, Box and whisker (10-90 percentile) plots of CXCR3⁺, HLA-DR^{hi}CD11c^{hi} and
 737 CD226⁺CD69⁺ monocytes measured by mass cytometry (whole blood, cohort 1): controls
 738 (n=9), FLI patients (n=8), COVID-19 patients (mild, n=8; severe, n=9). Kruskal-Wallis and
 739 Dunn's multiple comparison test.

740 **E**, Box plot of HLA-DR^{hi}CD11c^{hi} monocytes (cohort 2) measured by flow cytometry: COVID-
 741 19 (mild, n=3; severe, n=7) and age-matched controls (n=11). Unpaired t-test.

742 * $p<0.05$, ** $p<0.01$, *** $p<0.001$, **** $p<0.0001$.

743

744 **Figure 4. Disease-related longitudinal changes in monocyte transcriptomes**

745 **A**, UMAP visualization of monocytes (43,772 cells; from Fig. 2C, cohort 2); 46 samples from
 746 controls (n=6) and COVID-19 (mild, n=7; severe, n=8). Cells are colored according to the
 747 identified monocyte clusters (Louvain clustering, **Table S4**).

748 **B**, Visualization of scaled expression of selected genes (monocyte markers, **Fig. 2+S3E**)
 749 using the UMAP defined in (A). Three main clusters defining monocytes in COVID-19 (*HLA-DR^{lo}CD163^{hi}*, *HLA-DR^{lo}S100A^{hi}*, and *HLA-DR^{hi}CD83^{hi}* monocytes) indicated by dashed
 750 areas.
 751

752 **C**, AUCell-based enrichment of a gene signature from sepsis-associated monocytes (MS1
 753 cells) (Reyes et al., 2020), violin plots of the ‘Area Under the Curve’ (AUC) scores.
 754 Horizontal lines: median of the respective AUC scores per cluster.

755 **D**, Cytokine detection of IL-1 β , TNF α , and IL-12 in supernatants of purified monocytes
 756 (controls, ctrl, n=3; COVID-19, mild, n=3, and severe, n=3) after 8h *in vitro* incubation with or
 757 without 1ng/ml LPS. Kruskal-Wallis test adjusted with Benjamini-Hochberg method, *p<0.05.

758 **E**, Mapping of monocytes derived from COVID-19 patients (mild early, mild late, severe
 759 early, and severe late) onto UMAP from (A), coloring according to monocyte cluster identity.

760 **F**, Cluster occupancy over time for patients with longitudinal scRNA-seq data (mild, n=5;
 761 severe, n=7), coloring according to (A). Vertical dashed lines: time points of sampling. Red
 762 bar: WHO ordinal scale. X: patient deceased. Patient IDs on the right side, grouping
 763 according to disease severity. Bold dotted line (right): patients classified as mild at initial
 764 sampling developing severe disease over time.

765 **G**, Time-dependent change of *IFI6* and *ISG15* expression (violin-plots) in monocytes of
 766 cohort 1 (mild (yellow), n=4; severe (red), n=4), cohort 2 (mild (yellow), n=5; severe (red),
 767 n=7), and controls (cohort 1, n=22, cohort 2, n=6).

768 **H**, Network representation of marker genes and their predicted upstream transcriptional
 769 regulators for monocyte clusters 0, 1, 2, 3. Edges: predicted transcriptional regulation.
 770 Transcription factors (TFs, inner circle) and predicted target genes (outer circle) represented
 771 as nodes sized and colored according to the scaled expression level across all clusters.
 772 Selected TFs and genes labeled based on connectivity and literature mining. Numbers in the
 773 center refer to clusters defined in (A).

774

775 **Figure 5. Immature and dysfunctional low-density neutrophils emerge in PBMC**

776 **A**, UMAP representation and clustering of low-density neutrophils (LDNs, 3,154 cells) in
 777 PBMC (cohort 1, clusters 5 / 6, **Fig. 2A**) from 21 samples (6 mild, 10 severe COVID-19). Left
 778 panel: cluster affiliation in **Fig. 2A**; right panel: data-driven clustering and cell type
 779 nomenclature based on marker genes (**Table S4**).

780 **B**, Dot plot of the top 10 marker genes sorted by average log fold change associated with
 781 the neutrophil clusters identified in (A).

782 **C**, Signature enrichment scores of single-cell data from neutrophil progenitors (Pellin et al.,
 783 2019; Popescu et al., 2019) in LDN clusters, plotted as violin plots. The lines in the violin
 784 plots represent the median of the respective AUC (Area Under the Curve) scores per cluster
 785 and the 0.25 and 0.75 quantiles. The ribosomal^{hi}-specific cluster 7 was excluded from this
 786 analysis.

787 **D**, Violin plots of expression of selected activation genes across the neutrophil clusters
 788 identified in (A). The panel of genes was chosen based on their described role in neutrophil
 789 extracellular trap formation (*PRTN3*, *ELANE*, *MPO*, *PADI4*) and neutrophil activation and
 790 dysregulation (*CD24*, *OLFM4*, *LCN2*, *BPI*, *CD274* (PD-L1), *Arginase 1* (*ARG1*) and *ANXA1*).

791 **E**, Expression of *ARG1* and *CD274*(PD-L1) projected on the UMAP from (A).

792

793 **Figure 6. Appearance of immature and PD-L1⁺ neutrophils in severe COVID-19**

794 **A**, Heatmap revealing differences in marker expression determined by mass cytometry
 795 (antibody panel 2, cohort 1) of main neutrophil cell cluster (1 to 10). Main individual
 796 neutrophil cell clusters are displayed in columns and marker identity is indicated in rows. MSI
 797 = marker staining intensity respective expression level, significance level for the following
 798 comparisons i) controls (ctrl, n=9) vs. COVID-19 (mild & severe, n=17, first row), ii) mild
 799 (n=8) vs. severe (n=9, second row), iii) FLI (n=8) vs. mild COVID-19 (n=8, third row) as well
 800 as iv) controls (ctrl, n=9) vs. FLI (n=8) are indicated using a grey scale on top of the heatmap
 801 (see also p-value scale next to the heatmap). Samples of COVID-19 patients collected
 802 between day 4 and 13 post-symptom onset (= first day of sample collection per patient).
 803 Abundance testing via generalized mixed effects models and multiple comparison
 804 adjustment using the Benjamini-Hochberg procedure and an FDR-cutoff of 5 % across all
 805 clusters/subsets and between-group comparisons

806 **B**, UMAP of neutrophils, down-sampled to 70,000 cells (30 markers, **Table S2**). Cells are
 807 colored according to main cell clusters (1 to 10, see table). Donor origin (blue=controls,
 808 grey=FLI, yellow=mild COVID-19, red=severe COVID-19).

809 **C**, UMAP (from (B) with cells colored according to expression intensity of CD38, CD34,
 810 CD16, CD11b, CD33, CD64, CD62L and CD45.

811 **D**, Box and whisker (10-90 percentile) plots of main neutrophil cell cluster 1 to 7, reaching
 812 proportions of over 1%, measured by mass cytometry (whole blood, cohort 1): controls
 813 (n=9), FLI (n=8), and COVID-19 (mild, n=8; severe, n=9). Abundance testing via generalized
 814 mixed effects models and multiple comparison adjustment using the Benjamini-Hochberg
 815 procedure and an FDR-cutoff of 5% across all clusters/subsets and between-group
 816 comparisons.

817 **E**, Box and whisker (10-90 percentile) plots of proportions of CD34⁺, CD11b^{lo/-}CD16⁻, CD64⁺,
 818 CD62L⁺, CD10⁻CD11b^{lo/-}CD16⁻ (reported from panel 1) and PD-L1⁺ neutrophils (whole blood,
 819 cohort 1): controls (n=9), FLI (n=8), and COVID-19 (mild, n=8; severe, n=9). Kruskal-Wallis
 820 and Dunn's multiple comparison test.

821 *p<0.05, **p<0.01, ***p<0.001, ****p<0.0001

822

823 **Figure 7. Immature and dysfunctional whole blood neutrophils in severe COVID-19**

- 824 **A**, UMAP of 35 fresh blood samples from cohort 2 (122,954 cells, PBMC and whole blood):
 825 controls (n=17), mild COVID-19 (early, n=3; late, n=3) and sever COVID-19 (early, n=3,
 826 late=9). Clusters defined by Louvain clustering. Cell types assigned based on reference-
 827 based cell type classification (Aran et al., 2019) and marker gene expression (**Table S4**).

 828 **B**, UMAP visualization of neutrophils (58,383 cells; 34 whole blood samples, cohort 2):
 829 controls (n=16), mild COVID-19 (early, n=3; late, n=3), severe COVID-19 (early, n=3; late,
 830 n=9). Clusters defined by Louvain clustering (**Table S4**).

 831 **C**, Nomenclature and marker genes for each neutrophil cluster from (B).

 832 **D**, Dot plot of selected marker genes for each neutrophil cluster from (B).

 833 **E**, Dot plot of genes from different functional classes (based on literature research). Cluster
 834 8, 6, 1, and 2 are specific for severe COVID-19, cluster 0 represents homeostatic mature
 835 neutrophils from controls.

 836 **F**, Heatmap divided by disease severity and stage (early vs. late) showing the proportion of
 837 each patient group for each cluster.

 838 **G**, Density plot of cell frequency by disease severity and stage (early vs. late) overlaid on the
 839 UMAP of the neutrophil space.

 840 **H**, UMAP visualization showing scaled expression of *CD274 (PD-L1)* and *FCGR1A(CD64)*.

 841 **I**, Violin plots showing AUCell-based enrichment as AUC scores of gene signature from
 842 granulocytic myeloid-derived suppressor cells (Bayik et al., 2020) and *PD-L1^{hi}* neutrophils
 843 after LPS exposure (de Kleijn et al., 2013) in neutrophil clusters from (B). Horizontal lines:
 844 median of the respective AUC scores per cluster and 0.25 and 0.75 quantiles.

 845 **J**, Network representation of marker genes and their predicted upstream transcriptional
 846 regulators for neutrophil clusters 1 (mature/COVID-19 severe-specific) and 0 (mature /
 847 control-specific). Edges in cluster color: predicted transcriptional regulation. TFs (inner circle)
 848 and their predicted target genes (outer circle): nodes, sized and colored according to scaled
 849 expression level across all clusters. Selected genes and TFs labeled based on connectivity
 850 and literature mining.

 851 **K**, Box and whisker (10-90 percentile) plots representing the hematological analyses (whole
 852 blood, cohort 1): mild (n=11), severe (n=21) COVID-19. Analytes, measured by flow
 853 cytometry in white blood cell differential channel, included absolute counts of immature
 854 granulocytes (IG, dotted line: upper limit of reference range) and width of neutrophil
 855 cytometric dispersions (NE-WX, dispersion of side scatter; NE-WY, dispersion of side
 856 fluorescence light; NE-WZ, dispersion of forward scatter). Mann Whitney test applied to IG
 857 count analysis and Mixed-effect-analysis and Sidak's multiple comparison test to NE-WX,
 858 NE-WY and NE-WZ analyses.

 859 **L**, Box and whisker (10-90 percentile) plots of *E.coli*- and PMA-induced neutrophil oxidative
 860 burst (ROS production) and phagocytosis of whole blood samples (cohort 1; mild, n=10;
 861 severe (n=8) COVID-19) in comparison to controls measured by flow cytometry. Dotted line:

862 relative level of controls run in the assay. Mixed-effect-analysis and Sidak's multiple
 863 comparison test. **p<0.01, ***p<0.001, ****p<0.0001.

864 Supplemental figure titles and legends

865 **Supplemental Figure 1. Overview of sample analysis pipeline, major leukocyte**
 866 **lineages definition and quantification by CyTOF and MCFC.** Related to Figure 1

867 **A,** Overview of the analysis pipeline for scRNA-seq and proteomics of COVID-19 samples.

868 **B,** High resolution SPADE analysis with 400 target nodes and individual nodes aggregated
 869 to the indicated major immune cell lineages according to the expression of lineage specific
 870 cell marker such as CD14 for monocytes and CD15 for neutrophils of whole blood samples
 871 collected from FLI patients, COVID-19 patients and controls and stained with CyTOF panel 1
 872 and 2, respectively.

873 **C,** Box plots of the composition of total granulocytes and non-classical monocytes within
 874 whole blood samples from the second cohort of COVID-19 patients showing either mild
 875 (n=3) or severe disease (n=7) as well as controls (n=11) measured by flow cytometry.
 876 Statistical analysis was performed using unpaired *t*-test. **p<0.01, ***p<0.001.

877

878 **Supplemental Figure 2. Cluster-specific marker gene expression shows inflammatory**
 879 **activation signatures of monocyte subsets and the appearance of neutrophil subsets**
 880 **in the PBMC fraction.** Related to Figure 2

881 **A,** Dot plots of the top 5 marker genes sorted by average log fold change determined for the
 882 clusters depicted in **Fig. 2A.**

883 **B,** Dot plot representation of the top 5 marker genes sorted by average log fold change
 884 determined for the clusters depicted in **Fig. 2D.**

885 **C:** Heatmap of the Spearman correlation coefficients between myeloid cell subsets in two
 886 cohorts, based on the union of top 50 marker genes per cluster.

887

888 **Supplemental Figure 3. Transcriptional differences of monocytes from mild and**
 889 **severe COVID-19.** Related to Figure 4

890 **A,** Dot plot of the top 10 marker genes sorted by average log fold change of the clusters
 891 within the monocyte space of cohort 1 (related to **Fig. 2, Table S4**).

892 **B,** Gene ontology enrichment analysis based on the complete marker genes obtained for
 893 each monocyte cluster of cohort 1, showing the top 10 significant terms enriched in each
 894 cluster ranked by adjusted p-values.

895 **C**, Back-mapping of monocyte clusters of cohort 2 (**Fig. 4C**) onto the PBMC UMAP of cohort
 896 2 (**Fig. 2D**). The legend shows the association of the colors to the clusters together with the
 897 labeling of the clusters based on expressed marker genes (according to **Fig. 2** and **Fig.**
 898 **S3D-F**).

899 **D**, Violin plots of marker gene expression in the monocyte clusters identified in the complete
 900 PBMC space of cohort 2 (**Fig. 2C,D**)

901 **E**, Dot plot of the top 10 marker genes sorted by average log fold change calculated for the
 902 monocyte clusters (**Fig. 4C**).

903 **F**, Violin plots of the *IFI6* and *ISG15* expression in cells of mild and severe patients,
 904 additionally divided into early (1-10 days after disease onset) and late (>10 days after
 905 disease onset). Statistical analysis was performed using Wilcoxon Rank Sum test adjusted
 906 with the Bonferroni method, ****p<0.0001.

907 **G**, Violin plots showing the time-dependent change of *HLA-DRA* and *HLA-DRB1* expression
 908 in the monocyte population of cohort 1 (mild: n=4; severe: n=4) and cohort 2 (mild: n=5;
 909 severe: n=7). Mild samples are colored in yellow, severe samples in red and controls in blue,
 910 with the latter shown as reference violin plots representing the expression of all control
 911 monocytes in the respective cohort (cohort 1: n=22, cohort 2: n=6).

912

913 **Supplemental Figure 4. Additional analysis of dysfunctional neutrophils in PBMC**
 914 **fraction.** Related to Figure 5

915 **A**, Dot plot of marker genes associated with immature neutrophils (pro- and pre-neutrophils),
 916 and mature neutrophils.

917 **B**, Pie charts showing the proportion of cells predicted to be in a given cell cycle stage. The
 918 numbers refer to the cell clusters presented in panel A.

919

920 **Supplemental Figure 5. Longitudinal analysis of neutrophil and monocyte cell**
 921 **populations.** Related to Figure 6

922 **A**, Box and whisker (10-90 percentile) plots of time-dependent differences in total
 923 granulocytes and monocytes, non-classical monocytes and correlation analysis between
 924 days post-symptom onset and proportion of non-classical monocytes.

925 **B**, Box and whisker (10-90 percentile) plots of time-dependent differences in main neutrophil
 926 cell cluster 3, 5, 6 and 7 in cohort 1.

927 **C**, Box and whisker (10-90 percentile) plots of time-dependent differences in proportions of
 928 CD34⁺, CD11b^{lo/-}CD16⁻, CD64⁺, CD62L⁺, CD10⁻CD11b^{lo/-}CD16⁻ (reported from panel 1) and
 929 PD-L1⁺ neutrophils in cohort 1.

930 **D**, Box and whisker (10-90 percentile) plots of time-dependent differences in main monocyte
 931 cluster 1, 10 (belonging to CD14^{hi}CD16⁻ classical monocytes), cluster 11 and 3 (belonging to
 932 CD14^{hi}CD16⁺ intermediate monocytes) in cohort 1.

933 **E**, Box and whisker (10-90 percentile) plots of time-dependent differences in CXCR3⁺, HLA-
 934 DR^{hi}CD11c^{hi} and CD226⁺CD69⁺ monocytes.

935 **F**, Box and whisker (10-90 percentile) plot showing time-dependent differences in HLA-
 936 DR^{hi}CD11c^{hi} monocytes in cohort 2.

937 Measurements in cohort 1 were done applying mass cytometry on whole blood samples
 938 distinguishing between COVID-19 patients with mild (days 0-10: n=6, days 11-30: n=12) or
 939 severe disease (days 0-10: n=9, days 11-30: n=13) course. Mixed-effect-analysis and
 940 Sidak's multiple comparison test was used to calculate significant differences

941 Measurements in cohort 2 were done with flow cytometry on 26 whole blood samples from
 942 COVID-19 patients showing either mild (n=8) or severe disease (n=18) course as well as 11
 943 samples from age-matched controls (n=10).

944 *p<0.05, **p<0.01, ***p<0.001, ****p<0.0001

945

946 **Supplemental Figure 6. Overview of scRNA-seq dataset from cohort 2 and additional**
 947 **characterization of neutrophils.** Related to Figure 7

948 **A**, UMAP (on the left) of the complete scRNA-seq dataset from cohort 2 (frozen PBMC, fresh
 949 PBMC, fresh whole blood), encompassing 98 samples from 16 controls, 8 mild, and 10
 950 severe COVID-19 patients. Right panel: violin plots of the number of genic reads, transcripts
 951 and genes expressed in the PBMC (right) vs. the granulocyte fraction (left) across the
 952 different data sets of cohort 2. The UMAP is split by experimental condition and the
 953 classified granulocyte and PBMC fractions are marked separately. The table below indicates
 954 the number of cells per experimental condition separated by control, COVID-19 mild and
 955 COVID-19 severe. The numbers of samples are indicated in brackets.

956 **B**, Box plot of cell type frequencies identified by scRNA-seq in fresh whole blood samples
 957 after erythrocyte lysis comparing 16 samples from 15 controls, 6 from 5 mild COVID-19 and
 958 12 from 4 severe COVID-19 patients.

959 **C**, Comparison between cell frequencies identified by scRNA-seq and MCFC. Pearson's
 960 correlation between the mean of each cell population measured in MCFC (y-axis) and by
 961 scRNA-seq of R²=0.96 with p=0.0098 (left). The stacked bar chart sorted by disease severity
 962 shows the cell type frequency for controls (n=16), mild (n=5) and severe COVID-19 samples
 963 (n=18) split by scRNA-seq and MCFC.

964 **D**, Dot plot of literature-based marker genes classifying different neutrophil subsets.

965 **E**, UMAP of neutrophils showing the scaled expression of MME(CD10) and CXCR4 with
 966 enrichment in the control-specific clusters 0.

967 **F**, UMAP of AUCell-based enrichment of gene signatures derived from the neutrophil
 968 clusters from cohort 2 on the UMAP visualization of cohort 1. The UMAP is colored by the
 969 'Area Under the Curve' (AUC) scores of each cell.

970 **G**, Dot plot visualization of selected significantly enriched Gene Ontology terms and KEGG
 971 pathways for each cluster from the neutrophil space. The dots are colored by their adjusted
 972 p-value and the size of the dots is defined by the number of genes found in the Gene
 973 Ontology term.

974 **H**, Network representation of marker genes and their predicted upstream transcriptional
 975 regulators for neutrophil clusters 6 (pre-Neutrophils) and 8 (pro-Neutrophils). Edges
 976 represent predicted transcriptional regulation. Transcription factors in the inner circle and
 977 their predicted target genes in the outer circle are represented as nodes sized and colored
 978 according to the scaled expression level across all clusters. Selected genes and
 979 transcription factors were labeled based on connectivity and literature mining.

980 **I**, Diffusion map dimensionality reduction of the main neutrophil clusters 8, 6, 2, and 1 from
 981 the severe COVID-19 patients (top) and diffusion pseudotime visualized on the diffusion map
 982 indicating the transition probability of the different clusters in the following order: 8 - 6 - 2 - 1
 983 (bottom).

984 **J**, Genes specific for each cluster (*HSP90AA1*, *CD274(PD-L1)*, *CD177*, *MME(CD10)*, *ARG1*)
 985 visualized along the diffusion pseudotime (top) with the density of each cluster along the
 986 pseudotime (bottom) highlighting the proposed order of differentiation of the different
 987 neutrophil subsets.

988

989 **STAR Methods**990 **RESOURCE AVAILABILITY**991 ***Lead Contact***

992 Further information and requests for resources and reagents should be directed to and will
 993 be fulfilled by the Lead Contact, **Joachim L. Schultze** (j.schultze@uni-bonn.de).

994 ***Materials Availability***

995 This study did not generate new unique reagents.

996 ***Data and Code Availability***

997 ScRNA-seq data generated during this study are deposited at the European Genome-
 998 phenome Archive (EGA) under access number EGAS00001004571, which is hosted by the
 999 EBI and the CRG. Additional supplemental items are available from Mendeley Data at
 1000 <https://data.mendeley.com/datasets/hwxhw2sxys/draft?a=50288c49-d6c2-4740-882b-f27b0e1e41a4>.
 1001

1002

1003 **EXPERIMENTAL MODEL AND SUBJECT DETAILS**

1004 Samples from patients with COVID-19 were collected within two cohort studies (Kurth et al.,
 1005 2020) designed to allow deep molecular and immunological transcriptomic and proteomic
 1006 profiling of COVID-19 in blood. Patients for which sufficient material was available for
 1007 scRNA-seq, CyTOF or flow cytometry analysis, were included in this study. This study was
 1008 designed to describe immunological deviations in COVID-19 patients without intention of the
 1009 development of new treatments or new diagnostics, and therefore sample size estimation
 1010 was not included in the original study design.

1011 ***Cohort 1 / Berlin cohort***

1012 This study includes a subset of patients enrolled between March 2 and July 02 2020 in the
 1013 Pa-COVID-19 study, a prospective observational cohort study assessing pathophysiology
 1014 and clinical characteristics of patients with COVID-19 at Charité Universitätsmedizin Berlin
 1015 (Kurth et al., 2020). The study is approved by the Institutional Review board of Charité
 1016 (EA2/066/20). Written informed consent was provided by all patients or legal representatives
 1017 for participation in the study. The patient population included in all analyses of cohort 1
 1018 consists of 10 control donors (samples collected in 2019 before SARS-CoV2 outbreak), 8
 1019 patients presenting with flu-like illness but tested SARS-CoV-2-negative, 25 mild and 29
 1020 severe COVID-19 patients (**Figure 1A+B, Table S1**). Information on age, sex, medication,
 1021 and co-morbidities is listed in **Table S1**. All COVID-19 patients were tested positive for
 1022 SARS-CoV-2 RNA in nasopharyngeal swabs and allocated to mild (WHO 2-4) or severe (5-
 1023 7) disease according to the WHO clinical ordinal scale. We also included publicly available
 1024 single-cell transcriptome data derived from 22 control samples into the analysis; 3 samples

1025 were derived from 10x Genomics, San Francisco, CA 94111, USA (5k_pbmc_v3;
 1026 pbmc_10k_v3; pbmc_1k_v3), 19 samples derived from Reyes M, et al. (Reyes et al., 2020).

1027 ***Cohort 2 / Bonn cohort***

1028 This study was approved by the Institutional Review board of the University Hospital Bonn
 1029 (073/19 and 134/20). After providing written informed consent, 19 control donors and 22
 1030 COVID-19 patients (**Figure 1A+B, Table S1**) were included in the study. In patients who
 1031 were not able to consent at the time of study enrollment, consent was obtained after
 1032 recovery. Information on age, sex, medication, and co-morbidities are listed in **Table S1**.
 1033 COVID-19 patients who tested positive for SARS-CoV-2 RNA in nasopharyngeal swabs
 1034 were recruited at the Medical Clinic I of the University Hospital Bonn between March 30 and
 1035 June 17, 2020 and allocated to mild (WHO 2-4) or severe (5-7) disease according to the
 1036 WHO clinical ordinal scale. Controls in cohort 2 were collected from healthy people or from
 1037 otherwise hospitalized patients with a wide range of diseases and comorbidities including
 1038 chronic inflammatory immune responses. These individuals were either tested negative for
 1039 SARS-CoV-2, serologically negative or had no indication for acute COVID-19 disease based
 1040 on clinical or laboratory parameters.

1041

1042 **METHOD DETAILS**

1043 **Isolation of blood cells for scRNA-seq**

1044 ***Cohort 1 / Berlin cohort***

1045 PBMC were isolated from heparinized whole blood by density centrifugation over Pancoll
 1046 (density: 1.077g/ml; PAN-Biotech™). If the pellet was still slightly red, remaining CD235ab⁺
 1047 cells (Erythrocytes) were depleted by Negative Selection (*MagniSort*™ Thermo Fisher).
 1048 Subsequently the PBMC were prepared for 3'scRNA-seq (10xGenomics) or cryopreserved
 1049 and analyzed later.

1050

1051 ***Cohort 2 / Bonn cohort***

1052 In the Bonn cohort, scRNA-seq was performed on fresh whole blood, fresh PBMC and
 1053 frozen PBMC. Briefly, PBMC were isolated from EDTA-treated or heparinized peripheral
 1054 blood by density centrifugation over Pancoll or Ficoll-Paque density centrifugation (density:
 1055 1.077g/ml). Cells were then washed with DPBS, directly prepared for scRNA-seq (BD
 1056 Rhapsody) or cryopreserved in RPMI1640 with 40% FBS and 10% DMSO. Whole blood was
 1057 prepared by treatment of 1ml peripheral blood with 10ml of RBC lysis buffer (Biolegend).
 1058 After one wash in DPBS cells were directly processed for scRNA-seq (BD Rhapsody) or
 1059 multi-color flow cytometry (MCFC). Frozen PBMC were recovered by rapidly thawing frozen
 1060 cell suspensions in a 37°C water bath followed by immediate dilution in pre-warmed RPMI-
 1061 1640+10% FBS (Gibco) and centrifugation at 300g for 5min. After centrifugation, the cells
 1062 were resuspended in RPMI-1640+10% FBS and processed for scRNA-seq. Antibody
 1063 cocktails were cryopreserved as described before (Schulz et al., 2019).

1064

1065 **Antibodies used for mass cytometry**

1066 All anti-human antibodies pre-conjugated to metal isotopes were obtained from Fluidigm
 1067 Corporation (San Francisco, US). All remaining antibodies were obtained from the indicated
 1068 companies as purified antibodies and in-house conjugation was done using the MaxPar X8
 1069 labeling kit (Fluidigm). **Table S2** shows a detailed list of all antibodies used for panel 1 and
 1070 panel 2.

1071

1072 **Sample processing, antigen staining and data analysis of mass cytometry-based
 1073 immune cell profiling**

1074 500 μ l of whole blood (heparin) was fixed in 700 μ l of proteomic stabilizer (Smart Tube Inc.,
 1075 San Carlos, US) as described in the user manual and stored at -80°C until further
 1076 processing. Whole blood samples were thawed in Thaw/Lyse buffer (Smart Tube Inc.). For
 1077 barcoding antibodies recognizing human beta-2 microglobulin (B2M) were conjugated in
 1078 house to 104 Pd, 106 Pd, 108 Pd, 110 Pd, 198 Pt (Mei et al., 2015, 2016; Schulz and Mei, 2019). Up
 1079 to 10 individual samples were stained using a staining buffer from Fluidigm with a
 1080 combination of two different B2M antibodies for 30min at 4°C. Cells were washed and
 1081 pooled for surface and intracellular staining.

1082 For surface staining the barcoded and pooled samples were equally divided into two
 1083 samples. Cells were resuspended in antibody staining cocktails for panel 1 or panel 2
 1084 respectively (**Table S2**) and stained for 30min at 4°C. For secondary antibody staining of
 1085 panel 2, cells were washed and stained with anti-APC 163 Dy for 30min at 4°C. After surface
 1086 staining cells were washed with PBS and fixed overnight in PFA solution diluted in PBS to
 1087 2%.

1088 For intracellular staining cells were washed twice with a permeabilization buffer
 1089 (eBioscience, San Diego, US) and stained with the respective antibodies diluted in a
 1090 permeabilization buffer for 30min at room temperature. After washing, cells were stained
 1091 with iridium intercalator (Fluidigm) diluted in 2% PFA for 20min at room temperature. Cells
 1092 were washed once with PBS and then twice with ddH₂O and kept at 4°C until mass
 1093 cytometry measurement.

1094 A minimum of 100,000 cells per sample and panel were acquired on a CyTOF2/Helios mass
 1095 cytometer (Fluidigm). For normalization of the fcs files 1:10 EQ Four Element Calibration
 1096 Beads (Fluidigm) were added. Cells were analyzed using a CyTOF2 upgraded to Helios
 1097 specifications, with software version 6.7.1014, using a narrow bore injector. The instrument
 1098 was tuned according to the manufacturer's instructions with tuning solution (Fluidigm) and
 1099 measurement of EQ four element calibration beads (Fluidigm) containing 140/142Ce,
 1100 151/153Eu, 165Ho and 175/176Lu served as a quality control for sensitivity and recovery.
 1101 Directly prior to analysis, cells were resuspended in ddH₂O, filtered through a 20- μ m cell
 1102 strainer (Celltrics, Sysmex), counted and adjusted to 5-8 x10⁵ cells/ml. EQ four element
 1103 calibration beads were added at a final concentration of 1:10 v/v of the sample volume to be
 1104 able to normalize the data to compensate for signal drift and day-to-day changes in

1105 instrument sensitivity. Samples were acquired with a flow rate of 300-400 events/s. The
 1106 lower convolution threshold was set to 400, with noise reduction mode turned on and cell
 1107 definition parameters set at event duration of 10-150 pushes (push=13 μ s). The resulting flow
 1108 cytometry standard (FCS) files were normalized and randomized using the CyTOF
 1109 software's internal FCS-Processing module on the non-randomized ('original') data. The
 1110 default settings in the software were used with time interval normalization (100 s/minimum of
 1111 50 beads) and passport version 2. Intervals with less than 50 beads per 100s were excluded
 1112 from the resulting FCS file.

1113

1114 **Blood processing for multi-color flow cytometry**

1115 1ml of fresh blood from control or COVID-19 donors was treated with 10ml of RBC lysis
 1116 buffer (Biolegend). After RBC lysis, cells were washed with DPBS and 1-2 million cells were
 1117 used for flow cytometry analysis. Cells were then stained for surface markers (**Table S3**) in
 1118 DPBS with BD Horizon Brilliant™ Stain Buffer (Becton Dickinson) for 30min at 4°C. To
 1119 distinguish live from dead cells, the cells were incubated with LIVE/DEAD Fixable Yellow
 1120 Dead Cell Stain Kit (1:1000 – Thermo Scientific). Following staining and washing, the cell
 1121 suspension was fixed with 4% PFA for 5min at room temperature to prevent any possible
 1122 risk of contamination during acquisition of the samples. Flow cytometry analysis was
 1123 performed on a BD Symphony instrument (Becton Dickinson) configured with 5 lasers (UV,
 1124 violet, blue, yellow-green, red).

1125

1126 ***Ex vivo* functional analysis of neutrophils**

1127
 1128 Determination of neutrophil oxidative burst and phagocytosis was performed by flow
 1129 cytometry using the CE/IVD PHAGOBURST and PHAGOTEST assay (BD Biosciences,
 1130 Heidelberg, Germany) according to the manufacturer's instructions.
 1131

1132 Briefly, heparinized whole blood was incubated with PMA, unlabeled opsonized *E. coli*
 1133 bacteria or washing solution (negative control) at 37°C for 10min. Dihydrorhodamine (DHR
 1134 123) was then added for 10min, erythrocytes were lysed and DNA staining solution was
 1135 added. The freely cell permeable nonfluorescent Dihydrorhodamine 123 becomes
 1136 fluorescent when oxidized by reactive oxygen species. Stained samples were analyzed on a
 1137 Navios flow cytometer (Beckman Coulter, Krefeld, Germany) within less than 30min. The
 1138 respiratory burst intensity in neutrophils was determined by analysis of increase in the mean
 1139 fluorescence intensity (MFI) in the FL1 Channel in the stimulated samples compared to the
 1140 unstimulated control.

1141

1142 For analysis of neutrophil phagocytic activity, heparinized whole blood was incubated with
 1143 FITC-labeled opsonized *E. coli* bacteria for 10min at 37°C or 0°C (negative control). After
 1144 incubation, the reaction was stopped, erythrocytes were lysed and the DNA staining solution
 1145 was added. Stained samples were analyzed on a Navios flow cytometer (Beckman Coulter,
 1146 Krefeld, Germany) within less than 30min. The phagocytic activity of neutrophils was
 1147 determined by the increase in MFI in the FL1 Channel in the stimulated sample compared to

1148 the unstimulated control. Data were analyzed using prism version 8. Mixed-effect-analysis
 1149 and Sidak's multiple comparison test was applied to report statistical differences of *E.coli*-
 1150 and PMA-induced ROS production as well as phagocytosis between mild and severe
 1151 COVID-19 patients.

1152

1153 ***Ex vivo functional analysis of monocytes***

1154 Monocytes were isolated from frozen PBMCs by negative selection using the Pan Monocyte
 1155 Isolation Kit (Miltenyi, Bergisch Gladbach, Germany). The purity of isolated cells was
 1156 assessed by BD Canto 2 flow cytometer, and preparations with >85% purity were used for
 1157 experiments. Monocytes were resuspended in complete RPMI1640 medium (Gibco)
 1158 supplemented with 10% heat-inactivated fetal bovine serum (Pan Biotech), 10 U/ml penicillin
 1159 and 10µg/ml streptomycin (Sigma-Aldrich, USA), and stimulated for 8h with LPS (1 ng/ml;
 1160 TLRpure; Innaxon, UK). After stimulation, cell-free supernatants were collected and tested
 1161 for IL-1 β , IFNy, and TNFa, respectively, using the cytokine bead assay *Legend-Plex*
 1162 *Mix&Match inflammation panel 1 kit* (Biolegend, USA). Cytokine-bound beads were
 1163 measured with a BD Canto 2 flow cytometer and analyzed using Legend-Plex Software 8.0
 1164 (Biolegend, USA).

1165

1166 **Hematological analyses of the granulocyte compartment**

1167 Blood samples were collected into K₃EDTA evacuated plastic tubes (Greiner Bio-One
 1168 GmbH, Frickenhausen, Germany) and were subsequently analyzed using Sysmex XN-10
 1169 hematology analyzers within a XN-2000 or XN-9100 configuration (Sysmex Corporation,
 1170 Kobe, Japan) as previously described (Stiel et al., 2016). Immature granulocytes (IG) were
 1171 quantified by automated flow cytometry using the Sysmex WBC differential channel in XN-10
 1172 hematology analyzers within a XN-2000 or XN-9100 configuration (Sysmex Corporation,
 1173 Kobe, Japan). Whole blood was treated with Lysercell™WDF for cell permeabilization and
 1174 stained with the nucleic acid polymethine fluorescent dye Fluorocell™WDF according to
 1175 Sysmex-proprietary protocols without modifications. Subsequent differentiation of white
 1176 blood cells into lymphocytes, monocytes, neutrophils, eosinophils, and immature
 1177 granulocytes was achieved by flow cytometry using a 663 nm laser. The cell populations'
 1178 distinct forward-scattered light (FSC = NE-WZ, i.e. cell volume), side-scattered light (SSC =
 1179 NE-WX, i.e. granularity), and side-fluorescent light (SFL = NE-WY, i.e. nucleic acid content)
 1180 properties allowed determining the width of neutrophil cytometric dispersions applying
 1181 Sysmex-proprietary algorithms. Data were analysed using prism version 8. Mann Whitney
 1182 test was used to report differences in IG count, whereas mixed-effect-analysis and Sidak's
 1183 multiple comparison test was applied to report statistical differences of NE-WX, NE-WY and
 1184 NE-WZ between mild and severe COVID-19 patients.

1185

1186 **10x Genomics Chromium single-cell RNA-seq**

1187 PBMC were isolated and prepared as described above. Afterwards, patient samples were
 1188 hashtagged with TotalSeq-A antibodies (Biolegend) according to the manufacturer's protocol

1189 for TotalSeqTM-A antibodies and cell hashing with 10x Single Cell 3' Reagent Kit v3.1. 50µL
 1190 cell suspension with 1x10⁶ cells were resuspended in staining buffer (2% BSA, Jackson
 1191 Immuno Research; 0.01% Tween-20, Sigma-Aldrich; 1x DPBS, Gibco) and 5 µL Human
 1192 TruStain FcXTM FcBlocking (Biolegend) reagent were added. The blocking was performed
 1193 for 10min at 4°C. In the next step 1µg unique TotalSeq-A antibody was added to each
 1194 sample and incubated for 30min at 4°C. After the incubation time 1.5mL staining buffer were
 1195 added and centrifuged for 5min at 350g and 4°C. Washing was repeated for a total of 3
 1196 washes. Subsequently, the cells were resuspended in an appropriate volume of 1x DPBS
 1197 (Gibco), passed through a 40µm mesh (FlowmiTM Cell Strainer, Merck) and counted, using a
 1198 Neubauer Hemocytometer (Marienfeld). Cell counts were adjusted and hashtagged cells
 1199 were pooled equally. The cell suspension was super-loaded, with 50,000 cells, in the
 1200 ChromiumTM Controller for partitioning single cells into nanoliter-scale Gel Bead-In-
 1201 Emulsions (GEMs). Single Cell 3' reagent kit v3.1 was used for reverse transcription, cDNA
 1202 amplification and library construction of the gene expression libraries (10x Genomics)
 1203 following the detailed protocol provided by 10x Genomics. Hashtag libraries were prepared
 1204 according to the cell hashing protocol for 10x Single Cell 3' Reagent Kit v3.1 provided by
 1205 Biolegend, including primer sequences and reagent specifications. Biometra Trio Thermal
 1206 Cycler was used for amplification and incubation steps (Analytik Jena). Libraries were
 1207 quantified by QubitTM 2.0 Fluorometer (ThermoFisher) and quality was checked using 2100
 1208 Bioanalyzer with High Sensitivity DNA kit (Agilent). Sequencing was performed in paired-end
 1209 mode with a S1 and S2 flow cell (2x 50 cycles) using NovaSeq 6000 sequencer (Illumina).

1210

1211 BD Rhapsody single-cell RNA-seq

1212 Whole transcriptome analyses, using the BD Rhapsody Single-Cell Analysis System (BD,
 1213 Biosciences) were performed on PBMC and whole blood samples prepared as described
 1214 above. Cells from each sample were labeled with sample tags (BDTM Human Single-Cell
 1215 Multiplexing Kit) following the manufacturer's protocol. Briefly, a total number of 1x10⁶ cells
 1216 were resuspended in 180µl of Stain Buffer (FBS) (BD Pharmingen). The sample tags were
 1217 added to the respective samples and incubated for 20min at room temperature. After
 1218 incubation, 200µl stain buffer was added to each sample and centrifuged for 5min at 300g
 1219 and 4°C. Samples were washed one more time. Subsequently cells were resuspended in
 1220 300µl of cold BD Sample Buffer and counted using Improved Neubauer Hemocytometer
 1221 (INCYTO). Labelled samples were pooled equally in 650µl cold BD Sample Buffer. For each
 1222 pooled sample two BD Rhapsody cartridges were super-loaded with approximately 60,000
 1223 cells each. Single cells were isolated using Single-Cell Capture and cDNA Synthesis with the
 1224 BD Rhapsody Express Single-Cell Analysis System according to the manufacturer's
 1225 recommendations (BD Biosciences). cDNA libraries were prepared using the BD
 1226 RhapsodyTM Whole Transcriptome Analysis Amplification Kit following the BD RhapsodyTM
 1227 System mRNA Whole Transcriptome Analysis (WTA) and Sample Tag Library Preparation
 1228 Protocol (BD Biosciences). The final libraries were quantified using a Qubit Fluorometer with
 1229 the Qubit dsDNA HS Kit (ThermoFisher) and the size-distribution was measured using the
 1230 Agilent high sensitivity D5000 assay on a TapeStation 4200 system (Agilent technologies).
 1231 Sequencing was performed in paired-end mode (2*75 cycles) on a NovaSeq 6000 and
 1232 NextSeq 500 System (Illumina) with NovaSeq 6000 S2 Reagent Kit (200 cycles) and
 1233 NextSeq 500/550 High Output Kit v2.5 (150 Cycles) chemistry, respectively.

1234

1235 **QUANTIFICATION AND STATISTICAL ANALYSIS**1236 **Data pre-processing of 10x Genomics Chromium scRNA-seq data**

1237 CellRanger v3.1.0 (10x Genomics) was used to process scRNA-seq. To generate a digital
 1238 gene expression (DGE) matrix for each sample, we mapped their reads to a combined
 1239 reference of GRCh38 genome and SARS-CoV-2 genome and recorded the number of UMIs
 1240 for each gene in each cell.

1241

1242 **Data pre-processing of BD Rhapsody scRNA-seq data**

1243 After demultiplexing of bcl files using Bcl2fastq2 V2.20 from Illumina and quality control,
 1244 paired-end scRNA-seq reads were filtered for valid cell barcodes using the barcode whitelist
 1245 provided by BD. Cutadapt 1.16 was then used to trim NexteraPE-PE adapter sequences
 1246 where needed and to filter reads for a PHRED score of 20 or above (Martin, 2011). Then,
 1247 STAR 2.6.1b was used for alignment against the Gencode v27 reference genome (Dobin et
 1248 al., 2013). Dropseq-tools 2.0.0 were used to quantify gene expression and collapse to UMI
 1249 count data (<https://github.com/broadinstitute/Drop-seq/>). For hashtag-oligo based
 1250 demultiplexing of single-cell transcriptomes and subsequent assignment of cell barcodes to
 1251 their sample of origin the respective multiplexing tag sequences were added to the reference
 1252 genome and quantified as well.

1253

1254 **ScRNA-seq data analysis of 10x Chromium data of cohort 1**

1255 ScRNA-seq UMI count matrices were imported to R 3.6.2 and gene expression data analysis
 1256 was performed using the R/Seurat package 3.1.4 (Butler et al., 2018; Hafemeister and
 1257 Satija, 2019). Demultiplexing of cells was performed using the *HTODemux* function
 1258 implemented in Seurat.

1259 ***Data quality control***

1260 We excluded cells based on the following quality criteria: more than 25% mitochondrial
 1261 reads, more than 25% *HBA/HBB* gene reads, less than 250 expressed genes or more than
 1262 5,000 expressed genes and less than 500 detected transcripts. We further excluded genes
 1263 that were expressed in less than five cells. In addition, mitochondrial genes have been
 1264 excluded from further analysis.

1265 ***Normalization***

1266 LogNormalization (Seurat function) was applied before downstream analysis. The original
 1267 gene counts for each cell were normalized by total UMI counts, multiplied by 10,000 (TP10K)
 1268 and then log transformed by $\log_{10}(\text{TP10k}+1)$.

1269 ***Data integration***

1270 After normalization, the count data was scaled regressing for total UMI counts and principal
 1271 component analysis (PCA) was performed based on the 2,000 most variable features
 1272 identified using the vst method implemented in Seurat. Subsequently, the scRNA-seq data
 1273 from cohort 1 was integrated with publicly available 10x scRNAseq data of healthy controls
 1274 using the ‘harmony’ algorithm (Korsunsky et al., 2019) based on the first 20 principal
 1275 components to correct for technical differences in the gene expression counts of the different
 1276 data sources (Control samples from Reyes et al. (Reyes et al., 2020), 10x v3.1 PBMC
 1277 benchmarking data from healthy controls and 10x v3.1 scRNA-seq data from cohort 1). We
 1278 downloaded the count matrices for the publicly available scRNA-seq data and filtered the
 1279 cells using the above-mentioned quality criteria prior to data integration. For two-dimensional
 1280 data visualization we performed UMAP based on the first 20 dimensions of the ‘harmony’
 1281 data reduction. The cells were clustered using the Louvain algorithm based on the first 20
 1282 ‘harmony’ dimensions with a resolution of 0.4.

1283 ***Differential expression tests and cluster marker genes.***

1284 Differential expression (DE) tests were performed using FindMarkers/FindAllMarkers
 1285 functions in Seurat with Wilcoxon Rank Sum test. Genes with >0.25 log-fold changes, at
 1286 least 25% expressed in tested groups, and Bonferroni-corrected p-values<0.05 were
 1287 regarded as significantly differentially expressed genes (DEGs). Cluster marker genes were
 1288 identified by applying the DE tests for upregulated genes between cells in one cluster to all
 1289 other clusters in the dataset. Top ranked genes (by log-fold changes) from each cluster of
 1290 interest were extracted for further illustration. The exact number and definition of samples
 1291 used in the analysis are specified in the legend of **Fig. 2A** and summarized in **Table S1**.

1292 ***Cluster annotation.***

1293 Clusters were annotated based on a double-checking strategy: 1) by comparing cluster
 1294 marker genes with public sources, and 2) by directly visualizing the expression pattern of
 1295 CyTOF marker genes.

1296 ***GO enrichment analysis.***

1297 Significant DEGs between each monocyte cluster and the rest of monocyte subpopulations
 1298 were identified by FindMarkers function from the Seurat package using Wilcoxon Rank Sum
 1299 test statistics for genes expressed in at least 25% of all monocyte clusters. P-values were
 1300 corrected for multiple testing using Bonferroni correction and genes with corrected p-values
 1301 lower or equal 0.05 have been taken as significant DEGs for GO enrichment test by R
 1302 package/ClusterProfiler v.3.10.1 (Yu et al., 2012).

1303 ***Correlation analysis of marker genes for monocyte and neutrophils between cohort 1
 1304 and 2***

1305 To systematically compare the similarity of marker gene expression in the identified
 1306 monocyte/neutrophils subpopulations between the two cohorts, the Spearman correlation
 1307 coefficients were calculated based on the union of the top 50 marker genes of each cluster
 1308 sorted by fold change in the two cohorts, based on their average expression of all cells in the
 1309 specific subpopulation. The pairwise comparisons were performed, and the correlation
 1310 coefficients were displayed using a heatmap.

1311 **Subset analysis of the neutrophils within the PBMC data set of cohort 1**

1312 The neutrophil space was investigated by subsetting the PBMC dataset to those clusters
 1313 identified as neutrophils and immature neutrophils (cluster 5 and 6). Within those subsets,
 1314 we selected top 2,000 variable genes and repeated the clustering using the SNN-graph
 1315 based Louvain algorithm mentioned above with a resolution of 0.6. The dimensionality of the
 1316 data was then reduced to 10 PCs, which served as input for the UMAP calculation. To
 1317 categorize the observed neutrophil clusters into the respective cell cycle states, we applied
 1318 the CellCycleScoring function of Seurat and visualized the results as pie charts.

1319 A gene signature enrichment analysis using the ‘AUCCell’ method (Aibar et al., 2017) was
 1320 applied to link observed neutrophil clusters to existing studies and neutrophils of cohort 2.
 1321 We set the threshold for the calculation of the area under the curve (AUC) to marker genes
 1322 from collected publications and top 30 of the ranked maker genes from each of neutrophil
 1323 clusters from cohort 2. The resulting AUC values were normalized the maximum possible
 1324 AUC to 1 and subsequently visualized in violin plots or UMAP plots.

1325

1326 **ScRNA-seq data analysis of Rhapsody data of cohort 2**1327 ***General steps for Rhapsody data downstream analysis***

1328 ScRNA-seq UMI count matrices were imported to R 3.6.2 and gene expression data
 1329 analysis was performed using the R/Seurat package 3.1.2 (Butler et al., 2018).
 1330 Demultiplexing of cells was performed using the *HTODemux* function implemented in
 1331 Seurat. After identification of singlets, cells with more than 25% mitochondrial reads, less
 1332 than 250 expressed genes or more than 5,000 expressed genes and less than 500 detected
 1333 transcripts were excluded from the analysis and only those genes present in more than 5
 1334 cells were considered for downstream analysis. The following normalization, scaling and
 1335 dimensionality reduction steps were performed independently for each of the data subsets
 1336 used for the different analyses as indicated respectively. In general, gene expression values
 1337 were normalized by total UMI counts per cell, multiplied by 10,000 (TP10K) and then log
 1338 transformed by $\log_{10}(TP10k+1)$. Subsequently, the data was scaled, centered and
 1339 regressed against the number of detected transcripts per cell to correct for heterogeneity
 1340 associated with differences in sequencing depth. For dimensionality reduction, PCA was
 1341 performed on the top 2,000 variable genes identified using the vst method implemented in
 1342 Seurat. Subsequently, UMAP was used for two-dimensional representation of the data
 1343 structure. Cell type annotation was based on the respective clustering results combined with
 1344 data-driven cell type classification algorithms based on reference transcriptome data (Aran
 1345 et al., 2019) and expression of known marker genes.

1346 ***scRNA-seq analysis of the complete BD Rhapsody data set of cohort 2 including data
 1347 from frozen and fresh PBMC and whole blood***

1348 ScRNA-seq count data of 229,731 cells derived from fresh and frozen PBMC samples
 1349 purified by density gradient centrifugation and whole blood after erythrocyte lysis of cohort 2
 1350 (Bonn, BD Rhapsody) were combined, normalized and scaled as described above (see **Fig.**
 1351 **S6A**). After variable gene selection and PCA, UMAP was performed based on the first 20

1352 principal components (PCs). No batch correction or data integration strategies were applied
 1353 to the data. Visualization of the cells (**Fig. S6A**) showed overlay of cells of the same type
 1354 (e.g. T cells clustered within the same cluster, irrespective of cell isolation procedure). In
 1355 other words, cell type distribution was unaffected by the technical differences in sample
 1356 handling. Data quality and information content was visualized as violin plots showing the
 1357 number of detected genes, transcripts (UMIs) and genic reads per sample handling strategy
 1358 split by PBMC and granulocyte fraction.

1359 ***scRNA-seq analysis of fresh and frozen PBMC samples***

1360 ScRNA-seq count data of 139,848 cells derived from fresh and frozen PBMC samples of
 1361 cohort 2 (Bonn, BD Rhapsody) purified by density gradient centrifugation were normalized
 1362 and scaled as described above. After variable gene selection and PCA, UMAP was
 1363 performed and the cells were clustered using the Louvain algorithm based on the first 20
 1364 PCs and a resolution of 0.4. Cluster identities were determined by reference-based cell
 1365 classification and inference of cluster-specific marker genes using the Wilcoxon rank sum
 1366 test using the following cutoffs: genes have to be expressed in more than 20% of the cells of
 1367 the respective cluster, exceed a logarithmic fold change cutoff to at least 0.2, and exhibited a
 1368 difference of >10% in the detection between two clusters. The exact number and definition of
 1369 samples used in the analysis are specified in the legend of **Fig. 2D** and summarized in
 1370 **Table S1**.

1371 ***Quantification of the percentages of cell clusters in the PBMC scRNA-seq data of both***
 1372 ***cohorts separated by disease group***

1373 To compare shifts in the monocyte and neutrophil populations in the PBMC compartment of
 1374 COVID-19 patients, the percentages of the cellular subsets - as identified by clustering and
 1375 cluster annotation explained above for the two independent scRNA-seq data sets (cohort 1
 1376 and cohort 2) - of the total number of PBMC in each data set were quantified per sample and
 1377 visualized together in box plots. To determine the statistical significance of differences in cell
 1378 proportions between the different conditions, a Dirichlet regression model was used, due to
 1379 the fact that the proportions are not independent of one another. The R/RDirichletReg
 1380 (Maier, 2014) package was used. The p-values were corrected for multiple testing using the
 1381 Benjamini-Hochberg procedure.

1382 ***Subset analysis of the monocytes within the PBMC data set of cohort 2***

1383 The monocyte space was investigated by subsetting the PBMC dataset to those clusters
 1384 identified as monocytes (cluster 0-4), removing cells with strong multi-lineage marker
 1385 expressions, and repeating the variable gene selection (top 2,000 variable genes),
 1386 regression for the number of UMIs and scaling as described above. The dimensionality of
 1387 the data was then reduced to 8 PCs, which served as input for the UMAP calculation. The
 1388 SNN-graph based Louvain clustering of the monocytes was performed using a resolution of
 1389 0.2. Marker genes per cluster were calculated using the Wilcoxon rank sum test using the
 1390 following cutoffs: genes have to be expressed in >20% of the cells, exceed a logarithmic fold
 1391 change cutoff to at least 0.25, and exhibited a difference of >10% in the detection between
 1392 two clusters. The exact number and definition of samples used in the analysis are specified
 1393 in the legend of **Fig. 4A** and summarized in **Table S1**.

1394 ***Time kinetics analysis of identified monocyte clusters***

1395 For each patient and time point of sample collection, the proportional occupancy of the
 1396 monocyte clusters was calculated, and the relative proportions were subsequently visualized
 1397 as a function of time.

1398 ***Analysis of scRNA-seq data from fresh PBMC and whole blood samples of cohort 2***

1399 ScRNA-seq count data derived from fresh PBMC samples purified by density gradient
 1400 centrifugation and whole blood after erythrocyte lysis of cohort 2 (BD Rhapsody) were
 1401 normalized, scaled, and regressed for the number of UMI per cell as described above. After
 1402 PCA based on the top 2,000 variable genes, UMAP was performed using the first 30 PCs.
 1403 Cell clusters were determined using Louvain clustering implemented in Seurat based on the
 1404 first 30 principle components and a resolution of 0.8. Cluster identities were assigned as
 1405 detailed above using reference-based classification and marker gene expression.
 1406 Subsequently, the dataset was subsetted for whole blood samples after erythrocyte lysis and
 1407 clusters identified as neutrophils and immature neutrophils, and re-scaled and regressed.
 1408 After PCA on the top 2,000 variable genes, the neutrophil subset data was further processed
 1409 using the data integration approach implemented in Seurat (Stuart et al., 2019) based on the
 1410 first 30 PCs removing potential technical biases of separate experimental runs. UMAP and
 1411 clustering were performed as described above on the top 12 PCs using a resolution of 0.3.
 1412 Differentially expressed genes between clusters were defined using a Wilcoxon rank sum
 1413 test for differential gene expression implemented in Seurat. Genes had to be expressed in
 1414 >10% of the cells of a cluster, exceed a logarithmic threshold >0.1. The exact number and
 1415 definition of samples used in the analysis are specified in the legend of **Fig. 7A** and
 1416 summarized in **Table S1**.

1417 ***Quantification of percentages of cell subsets in whole blood scRNA-seq data of***
 1418 ***cohort 2***

1419 After cell type classification of the combined scRNA-seq data set of fresh PBMC and whole
 1420 blood samples of cohort 2 described above, 89,883 cells derived from whole blood samples
 1421 after erythrocyte lysis were subsetted. Percentages of cell subsets in those whole blood
 1422 samples of the total number of cells were quantified per sample and visualized in box plots
 1423 separated by disease stage and group.

1424 ***Confusion matrix***

1425 For each cluster of neutrophils, the relative proportion across disease severity and time point
 1426 was visualized as a fraction of samples from the respective condition contributing to the
 1427 cluster.

1428 ***GO enrichment***

1429 Gene set enrichment was performed on gene sets from the Kyoto Encyclopedia of Genes
 1430 and Genomes (KEGG) database (Kanehisa, 2019), Hallmark gene sets (Liberzon et al.,
 1431 2015) and Gene Ontology (GO) (Ashburner et al., 2000; Carbon et al., 2019) using the R
 1432 package/ClusterProfiler v.3.10.1 (Yu et al., 2012).

1433 **Cell cycle state analysis of scRNA-seq data**

1434 To categorize the cells within the neutrophil clusters into the respective cell cycle states, we
 1435 applied the *CellCycleScoring* function of Seurat and visualized the results as pie charts.

1436 **Trajectory analysis**

1437 Trajectory analysis was performed using the *destiny* algorithm v3.0.1 (Angerer et al., 2016).
 1438 In brief, the neutrophil space was subsetted to only severe patients (early and late) and only
 1439 the most prominent clusters of the latter (clusters 1,2,6,8). The normalized data were scaled
 1440 and regressed for UMIs and a diffusion map was calculated based on the top 2,000 variable
 1441 genes with a sum of at least 10 counts over all cells. Based on the diffusion map, a diffusion
 1442 pseudo time was calculated to infer a transition probability between the different cell states
 1443 of the neutrophils. Subsequently, the density of the clusters along the pseudotime and
 1444 marker gene expression for each cluster were visualized.

1445 Enrichment of gene sets was performed using the ‘AUCell’ method (Aibar et al., 2017)
 1446 implemented in the package (version 1.4.1) in R. We set the threshold for the calculation of
 1447 the AUC to the top 3% of the ranked genes and normalized the maximum possible AUC to 1.
 1448 The resulting AUC values were subsequently visualized in violin plots or UMAP plots.

1449 **Transcription factor prediction analysis**

1450 The Cytoscape (version v3.7.1, doi: 10.1101/gr.1239303) plug-in iRegulon (Janky et al.,
 1451 2014) (version 1.3) was used to predict the transcription factors potentially regulating cluster-
 1452 specifically expressed gene sets in the neutrophil and monocyte subset analysis in cohort 2.
 1453 The genomic regions for TF-motif search were limited to 10kb around the respective
 1454 transcriptional start sites and filtered for predicted TFs with a normalized enrichment score >
 1455 4.0. Next, we filtered for TFs, which exceeded a cumulative normalized expression cutoff of
 1456 50 in the respective cluster. Subsequently, we selected transcription factors of known
 1457 relevance in the context of neutrophil and monocyte biology and constructed a network
 1458 linking target genes among the cluster-specifically expressed marker genes and their
 1459 predicted and expressed regulators for visualization in Cytoscape.

1460

1461 **Mass cytometry data analysis**

1462 Cytobank.org was used for de-barcoding of individual samples and manually gating of cell
 1463 events to remove doublets, normalization beads and dead cells (Kotecha et al., 2010). Per
 1464 channel intensity ranges were aligned between batches of measurements using a reference
 1465 sample acquired across all batches and the BatchAdjust function to compute scaling factors
 1466 at the 95th event percentiles (Schuyler et al., 2019). For semi-automated gating of
 1467 populations of interest, high-resolution SPADE clustering was conducted on all indicated
 1468 asinh-transformed markers (**Table S2**) with 400 target nodes (Qiu et al., 2011). Individual
 1469 SPADE nodes were then aggregated and annotated to cell subsets (bubbles) according to
 1470 the expression of lineage-specific differentiation markers. Clustering results and FCS files
 1471 were subsequently loaded into the R CytoML/flowCore environment
 1472 ([10.18129/B9.bioc.CytoML](https://doi.org/10.18129/B9.bioc.CytoML), [10.18129/B9.bioc.flowCore](https://doi.org/10.18129/B9.bioc.flowCore)) for further downstream analyses. To

1473 generate UMAP representations all events of a given population of interest were down-
 1474 sampled to 70,000 cells and then embedded using the tmap function (R uwot package,
 1475 <https://CRAN.R-project.org/package=uwot>) parameterized by local neighborhood 50,
 1476 learning rate 0.5, and using the indicated markers (**Table S2**) as input dimensions. For
 1477 statistical analysis of cell population abundances, we fitted a generalized linear mixed-effects
 1478 model (GLMM) for each population using the lme4 package (Nowicka et al., 2019). P-values
 1479 resulting from differential abundance testing (via R multcomp and lsmeans packages) were
 1480 adjusted using the Benjamini-Hochberg procedure and an FDR-cutoff of 5% across all
 1481 clusters/subsets and between-group comparisons (Hothorn et al., 2008; Lenth, 2016).
 1482 Additionally, indicated surface marker positive populations were exported from Cytobank and
 1483 analysed using prism 8. Kruskal-Wallis and Dunn's multiple comparison test was used to
 1484 compare differences in proportions between patient groups, whereas mixed-effect-analysis
 1485 and Sidak's multiple comparison test was applied to report time-dependent differences. The
 1486 exact numbers and definitions of samples used in the analyses are specified in the
 1487 respective figure legends and summarized in **Table S1**.

1488 **Data Analysis of Flow Cytometry Data**

1489 Flow cytometry data analysis was performed with FlowJo V10.6.1. Cell type was defined as
 1490 granulocytes (CD45⁺, CD66b⁺), non-classical monocytes (CD45⁺, CD66b⁻, CD19⁻, CD3⁻,
 1491 CD56⁻, CD14^{lo}, CD16⁺). Relative cell percentage or mean fluorescence intensity (MFI) was
 1492 used for visualization and statistical analysis was done using unpaired *t*-test.

1493 **Data visualization**

1494 In general, the R packages Seurat and the ggplot2 package (version 3.1.0, Wickham, 2016)
 1495 were used to generate figures. For visualization of mass cytometry data, cluster minimum-
 1496 spanning trees were rendered using Cytobank, the ComplexHeatmap package (Gu et al.,
 1497 2016) was used to display subset phenotypes and GraphPad Prism to generate boxplots of
 1498 quantitative data.

1499 **ADDITIONAL RESOURCES**

1500 Part of the patients included in this study have been recruited within the clinical trial
 1501 DRKS00021688, registered at the German registry for clinical studies (Kurth et al., 2020).

1502 In addition to the deposition of the raw sequencing data on EGA, we provide an interactive
 1503 platform for data inspection and analysis via FASTGenomics. The FASTGenomics platform
 1504 (fastgenomics.org) provides processed count tables of the datasets generated in this study
 1505 as well as key analytical results, such as UMAP coordinates and cluster identities, and the
 1506 code written to analyze the respective data.

1507

1508 **Supplemental Tables**

1509

1510 **Table S1. Cohort details, related to all Figures**

1511

1512 **Table S2. Detailed information on antibody panels used for mass cytometry**
1513 **analysis, related to Figure 1,3,6**

1514

1515 **Table S3. List of antibodies used for multi-color flow cytometry, related to**
1516 **Figure 1,3,6**

1517

1518 **Table S4. Cluster-specific marker gene lists from the scRNA-seq analyses,**
1519 **related to Figure 2,4,5,7 + S2-4,S6**

1520

1521 References

- 1522
- 1523 Ahmad, S., Singh, P., Sharma, A., Arora, S., Shriwash, N., Rahmani, A.H., Almatroodi, S.A.,
 1524 Manda, K., Dohare, R., and Syed, M.A. (2019). Transcriptome meta-analysis deciphers a
 1525 dysregulation in immune response-associated gene signatures during sepsis. *Genes*
 1526 (*Basel*). *10*, 1005.
- 1527 Aibar, S., González-Blas, C.B., Moerman, T., Huynh-Thu, V.A., Imrichova, H., Hulselmans,
 1528 G., Rambow, F., Marine, J.C., Geurts, P., Aerts, J., et al. (2017). SCENIC: Single-cell
 1529 regulatory network inference and clustering. *Nat. Methods* *14*, 1083–1086.
- 1530 Alder, M.N., Opoka, A.M., Lahni, P., Hildeman, D.A., and Wong, H.R. (2017). Olfactomedin-
 1531 4 Is a Candidate Marker for a Pathogenic Neutrophil Subset in Septic Shock. *Crit. Care Med.*
 1532 *45*, e426–e432.
- 1533 Angerer, P., Haghverdi, L., Büttner, M., Theis, F.J., Marr, C., and Buettner, F. (2016).
 1534 Destiny: Diffusion maps for large-scale single-cell data in R. *Bioinformatics* *32*, 1241–1243.
- 1535 Aran, D., Looney, A.P., Liu, L., Wu, E., Fong, V., Hsu, A., Chak, S., Naikawadi, R.P.,
 1536 Wolters, P.J., Abate, A.R., et al. (2019). Reference-based analysis of lung single-cell
 1537 sequencing reveals a transitional profibrotic macrophage. *Nat. Immunol.* *20*, 163–172.
- 1538 Ashburner, M., Ball, C.A., Blake, J.A., Botstein, D., Butler, H., Cherry, J.M., Davis, A.P.,
 1539 Dolinski, K., Dwight, S.S., Eppig, J.T., et al. (2000). Gene ontology: Tool for the unification of
 1540 biology. *Nat. Genet.* *25*, 25–29.
- 1541 Bao, L., Deng, W., Huang, B., Gao, H., Liu, J., Ren, L., Wei, Q., Yu, P., Xu, Y., Qi, F., et al.
 1542 (2020). The pathogenicity of SARS-CoV-2 in hACE2 transgenic mice. *Nature* doi:
 1543 10.1038/s41586-020-2312-y.
- 1544 Barnes, B.J., Adrover, J.M., Baxter-Stoltzfus, A., Borczuk, A., Cools-Lartigue, J., Crawford,
 1545 J.M., Daßler-Plenker, J., Guerci, P., Huynh, C., Knight, J.S., et al. (2020). Targeting potential
 1546 drivers of COVID-19: Neutrophil extracellular traps. *J. Exp. Med.* *217*(6), e20200652.
- 1547 Bayik, D., Zhou, Y., Park, C., Hong, C., Vail, D., Silver, D.J., Lauko, A., Roversi, G., Watson,
 1548 D.C., Lo, A., et al. (2020). Myeloid-derived suppressor cell subsets drive glioblastoma growth
 1549 in a sex-specific manner. *Cancer Discov.* CD-19-1355.
- 1550 Bernardo, D., Marin, A.C., Fernández-Tomé, S., Montalban-Arques, A., Carrasco, A.,
 1551 Tristán, E., Ortega-Moreno, L., Mora-Gutiérrez, I., Díaz-Guerra, A., Caminero-Fernández,
 1552 R., et al. (2018). Human intestinal pro-inflammatory CD11chighCCR2+CX3CR1+
 1553 macrophages, but not their tolerogenic CD11c-CCR2-CX3CR1- counterparts, are expanded
 1554 in inflammatory bowel disease article. *Mucosal Immunol.* *11*, 1114–1126.
- 1555 Bowers, N.L., Helton, E.S., Huijbregts, R.P.H., Goepfert, P.A., Heath, S.L., and Hel, Z.
 1556 (2014). Immune Suppression by Neutrophils in HIV-1 Infection: Role of PD-L1/PD-1
 1557 Pathway. *PLoS Pathog.* *10*(3), e1003993.
- 1558 Braun, J., Loyal, L., Frentsche, M., Wendisch, D., Georg, P., Kurth, F., Hippenstiel, S.,
 1559 Dingeldey, M., Kruse, B., Fauchere, F., et al. (2020). Presence of SARS-CoV-2 reactive T
 1560 cells in COVID-19 patients and healthy donors. *MedRxiv* doi: 10.1101/2020.04.17.20061440.

- 1561 Bronte, V., Serafini, P., Mazzoni, A., Segal, D.M., and Zanovello, P. (2003). L-arginine
 1562 metabolism in myeloid cells controls T-lymphocyte functions. *Trends Immunol.* 24, 301–305.
- 1563 Bronte, V., Brandau, S., Chen, S.H., Colombo, M.P., Frey, A.B., Greten, T.F., Mandruzzato,
 1564 S., Murray, P.J., Ochoa, A., Ostrand-Rosenberg, S., et al. (2016). Recommendations for
 1565 myeloid-derived suppressor cell nomenclature and characterization standards. *Nat.*
 1566 *Commun.* 7, 12150.
- 1567 Butler, A., Hoffman, P., Smibert, P., Papalexis, E., and Satija, R. (2018). Integrating single-
 1568 cell transcriptomic data across different conditions, technologies, and species. *Nat.*
 1569 *Biotechnol.* 36, 411–420.
- 1570 Carbon, S., Douglass, E., Dunn, N., Good, B., Harris, N.L., Lewis, S.E., Mungall, C.J., Basu,
 1571 S., Chisholm, R.L., Dodson, R.J., et al. (2019). The Gene Ontology Resource: 20 years and
 1572 still GOing strong. *Nucleic Acids Res.* 47, D330–D338.
- 1573 Cassetta, L., Baekkevold, E.S., Brandau, S., Bujko, A., Cassatella, M.A., Dorhoi, A., Krieg,
 1574 C., Lin, A., Loré, K., Marini, O., et al. (2019). Deciphering myeloid-derived suppressor cells:
 1575 isolation and markers in humans, mice and non-human primates. *Cancer Immunol.*
 1576 *Immunother.* 68, 687–697.
- 1577 Castell, S.D., Harman, M.F., Morón, G., Maletto, B.A., and Pistoresi-Palencia, M.C. (2019).
 1578 Neutrophils which migrate to lymph nodes modulate CD4+ T cell response by a PD-L1
 1579 dependent mechanism. *Front. Immunol.* 10, 105.
- 1580 Chen, G., Wu, D., Guo, W., Cao, Y., Huang, D., Wang, H., Wang, T., Zhang, X., Chen, H.,
 1581 Yu, H., et al. (2020). Clinical and immunologic features in severe and moderate Coronavirus
 1582 Disease 2019. *J. Clin. Invest.* 130(5), 2620–2629.
- 1583 Chua, R.L., Lukassen, S., Trump, S., Hennig, B.P., Wendisch, D., Pott, F., Debnath, O.,
 1584 Thürmann, L., Kurth, F., Völker, M.T., et al. (2020). COVID-19 severity correlates with airway
 1585 epithelium–immune cell interactions identified by single-cell analysis. *Nat. Biotechnol.* doi:
 1586 10.1038/s41587-020-0602-4.
- 1587 Chun, E., Lavoie, S., Michaud, M., Gallini, C.A., Kim, J., Soucy, G., Odze, R., Glickman,
 1588 J.N., and Garrett, W.S. (2015). CCL2 Promotes Colorectal Carcinogenesis by Enhancing
 1589 Polymorphonuclear Myeloid-Derived Suppressor Cell Population and Function. *Cell Rep.* 12,
 1590 244–257.
- 1591 Cibrián, D., and Sánchez-Madrid, F. (2017). CD69: from activation marker to metabolic
 1592 gatekeeper. *Eur. J. Immunol.* 47, 946–953.
- 1593 Cohen, J. (2020). From mice to monkeys, animals studied for coronavirus answers. *Science*
 1594 (80-.). 368, 221–222.
- 1595 Cuevas, V.D., Anta, L., Samaniego, R., Orta-Zavalza, E., Vladimir de la Rosa, J., Baujat, G.,
 1596 Domínguez-Soto, Á., Sánchez-Mateos, P., Escribese, M.M., Castrillo, A., et al. (2017).
 1597 MAFB Determines Human Macrophage Anti-Inflammatory Polarization: Relevance for the
 1598 Pathogenic Mechanisms Operating in Multicentric Carpotarsal Osteolysis. *J. Immunol.* 198,
 1599 2070–2081.
- 1600 Darcy, C.J., Minigo, G., Piera, K.A., Davis, J.S., McNeil, Y.R., Chen, Y., Volkheimer, A.D.,
 1601 Weinberg, J.B., Anstey, N.M., and Woodberry, T. (2014). Neutrophils with myeloid derived
 1602 suppressor function deplete arginine and constrain T cell function in septic shock patients.
 1603 *Crit. Care* 18, R163.

- 1604 Davison, G.M., Nkambule, B.B., Mkandla, Z., Hon, G.M., Kengne, A.P., Erasmus, R.T., and
 1605 Matsha, T.E. (2017). Platelet, monocyte and neutrophil activation and glucose tolerance in
 1606 South African Mixed Ancestry individuals. *Sci. Rep.* 7, 40329. doi: 10.1038/srep40329.
- 1607 Dimopoulos, G., de Mast, Q., Markou, N., Theodorakopoulou, M., Komnos, A., Mouktaroudi,
 1608 M., Netea, M.G., Spyridopoulos, T., Verheggen, R.J., Hoogerwerf, J., et al. (2020).
 1609 Favorable Anakinra Responses in Severe Covid-19 Patients with Secondary
 1610 Hemophagocytic Lymphohistiocytosis. *Cell Host Microbe* 10.1016/j.chom.2020.05.007.
- 1611 Dobin, A., Davis, C.A., Schlesinger, F., Drenkow, J., Zaleski, C., Jha, S., Batut, P.,
 1612 Chaisson, M., and Gingeras, T.R. (2013). STAR: ultrafast universal RNA-seq aligner. 29,
 1613 15–21.
- 1614 Ellinghaus, D., Degenhardt, F., Bujanda, L., Buti, M., Albillos, A., Invernizzi, P., Fernández,
 1615 J., Prati, D., Baselli, G., Asselta, R., et al. (2020). Genomewide Association Study of Severe
 1616 Covid-19 with Respiratory Failure. *N. Engl. J. Med.* NEJMoa2020283.
- 1617 Fischer-Riepe, L., Daber, N., Schulte-Schrepping, J., Caroline eras De Carvalho, B. V.,
 1618 Russo, A., Pohlen, M., Fischer, J., Imam Chasan, A., Wolf, M., Ulas, T., et al. (2020). CD163
 1619 expression defines specific, IRF8-dependent, immune-modulatory macrophages in the bone
 1620 marrow. doi: 10.1016/j.jaci.2020.02.034.
- 1621 Giamarellos-Bourboulis, E.J., Netea, M.G., Rovina, N., Akinosoglou, K., Antoniadou, A.,
 1622 Antonakos, N., Damoraki, G., Gkavogianni, T., Adami, M.E., Katsaounou, P., et al. (2020).
 1623 Complex Immune Dysregulation in COVID-19 Patients with Severe Respiratory Failure. *Cell*
 1624 *Host Microbe* 27, doi: 10.1016/j.chom.2020.04.009.
- 1625 Grifoni, A., Weiskopf, D., Ramirez, S.I., Mateus, J., Dan, J.M., Moderbacher, C.R., Rawlings,
 1626 S.A., Sutherland, A., Premkumar, L., Jadi, R.S., et al. (2020). Targets of T cell responses to
 1627 SARS-CoV-2 coronavirus in humans with COVID-19 disease and unexposed individuals.
 1628 *Cell* doi: 10.1016/j.cell.2020.05.015.
- 1629 Gu, Z., Eils, R., and Schlesner, M. (2016). Complex heatmaps reveal patterns and
 1630 correlations in multidimensional genomic data. *Bioinformatics* 32(18), 2847–2849.
- 1631 Hadjadj, J., Yatim, N., Barnabei, L., Corneau, A., Boussier, J., Pere, H., Charbit, B., Bondet,
 1632 V., Chenevier-Gobeaux, C., Breillat, P., et al. (2020). Impaired type I interferon activity and
 1633 exacerbated inflammatory responses in severe Covid-19 patients. *MedRxiv* doi:
 1634 2020.04.19.20068015.
- 1635 Hafemeister, C., and Satija, R. (2019). Normalization and variance stabilization of single-cell
 1636 RNA-seq data using regularized negative binomial regression. *Genome Biol.* 20(1), doi:
 1637 10.1186/s13059-019-1874-1.
- 1638 Hesselink, L., Spijkerman, R., Van Wessem, K.J.P., Koenderman, L., Leenen, L.P.H.,
 1639 Huber-Lang, M., and Hietbrink, F. (2019). Neutrophil heterogeneity and its role in infectious
 1640 complications after severe trauma. *World J. Emerg. Surg.* 14(1), doi: 10.1186/s13017-019-0244-3.
- 1642 Hirano, N., Butler, M.O., Xia, Z., Ansén, S., Von Bergwelt-Baildon, M.S., Neuberg, D.,
 1643 Freeman, G.J., and Nadler, L.M. (2006). Engagement of CD83 ligand induces prolonged
 1644 expansion of CD8+ T cells and preferential enrichment for antigen specificity. *Blood* 107,
 1645 1528–1536.
- 1646 Hoffmann, S., Harms, H., Ulm, L., Nabavi, D.G., Mackert, B.M., Schmehl, I., Jungehulsing,

- 1647 G.J., Montaner, J., Bustamante, A., Hermans, M., et al. (2017). Stroke-induced
 1648 immunodepression and dysphagia independently predict stroke-associated pneumonia –
 1649 The PREDICT study. *J. Cereb. Blood Flow Metab.* 37, 3671–3682.
- 1650 Horby, P., Lim, W.S., Emberson, J.R., Mafham, M., Bell, J.L., Linsell, L., Phil, D., Sta-Plin,
 1651 N., Brightling, C., Med, F., et al. (2020). Dexamethasone in Hospitalized Patients with Covid-
 1652 19 — Preliminary Report. *N. Engl. J. Med.* NEJMoa2021436.
- 1653 Hothorn, T., Bretz, F., and Westfall, P. (2008). Simultaneous inference in general parametric
 1654 models. *Biometrical J.* 50, 346–363.
- 1655 Huang, C., Wang, Y., Li, X., Ren, L., Zhao, J., Hu, Y., Zhang, L., Fan, G., Xu, J., Gu, X., et
 1656 al. (2020a). Clinical features of patients infected with 2019 novel coronavirus in Wuhan,
 1657 China. *Lancet* 395, 497–506.
- 1658 Huang, X., He, C., Lin, G., Lu, L., Xing, K., Hua, X., Sun, S., Mao, Y., Song, Y., Wang, J., et
 1659 al. (2020b). Induced CD10 expression during monocyte-to-macrophage differentiation
 1660 identifies a unique subset of macrophages in pancreatic ductal adenocarcinoma. *Biochem.
 1661 Biophys. Res. Commun.* 524, 1064–1071.
- 1662 Jamilloux, Y., Henry, T., Belot, A., Viel, S., Fauter, M., El Jammal, T., Walzer, T., François,
 1663 B., and Sève, P. (2020). Should we stimulate or suppress immune responses in COVID-19?
 1664 Cytokine and anti-cytokine interventions. *Autoimmun. Rev.* 19(7), 102567.
- 1665 Janký, R., Verfaillie, A., Imrichová, H., van de Sande, B., Standaert, L., Christiaens, V.,
 1666 Hulselmans, G., Herten, K., Naval Sanchez, M., Potier, D., et al. (2014). iRegulon: From a
 1667 Gene List to a Gene Regulatory Network Using Large Motif and Track Collections. *PLoS
 1668 Comput. Biol.* 10, doi: 10.1371/journal.pcbi.1003731.
- 1669 Janols, H., Wullt, M., Bergenfelz, C., Björnsson, S., Lickei, H., Janciauskiene, S.,
 1670 Leandersson, K., and Bredberg, A. (2014). Heterogeneity among septic shock patients in a
 1671 set of immunoregulatory markers. *Eur. J. Clin. Microbiol. Infect. Dis.* 33, 313–324.
- 1672 Kamp, V.M., Pillay, J., Lammers, J.-W.J., Pickkers, P., Ulfman, L.H., and Koenderman, L.
 1673 (2012). Human suppressive neutrophils CD16 bright /CD62L dim exhibit decreased
 1674 adhesion. *J. Leukoc. Biol.* 92, 1011–1020.
- 1675 Kanehisa, M. (2019). Toward understanding the origin and evolution of cellular organisms.
 1676 *Protein Sci.* 28, 1947–1951.
- 1677 Kangelaris, K.N., Prakash, A., Liu, K.D., Aouizerat, B., Woodruff, P.G., Erle, D.J., Rogers, A.,
 1678 Seeley, E.J., Chu, J., Liu, T., et al. (2015). Increased expression of neutrophil-related genes
 1679 in patients with early sepsis-induced ARDS. *Am. J. Physiol. - Lung Cell. Mol. Physiol.* 308,
 1680 L1102–L1113.
- 1681 de Kleijn, S., Langereis, J.D., Leentjens, J., Kox, M., Netea, M.G., Koenderman, L.,
 1682 Ferwerda, G., Pickkers, P., and Hermans, P.W.M. (2013). IFN-γ-Stimulated Neutrophils
 1683 Suppress Lymphocyte Proliferation through Expression of PD-L1. *PLoS One* 8(8), e72249.
- 1684 Klok, F.A., Kruip, M.J.H.A., van der Meer, N.J.M., Arbous, M.S., Gommers, D.A.M.P.J., Kant,
 1685 K.M., Kaptein, F.H.J., van Paassen, J., Stals, M.A.M., Huisman, M. V., et al. (2020).
 1686 Incidence of thrombotic complications in critically ill ICU patients with COVID-19. *Thromb.
 1687 Res.* doi: 10.1016/j.thromres.2020.04.013.
- 1688 Korsunsky, I., Millard, N., Fan, J., Slowikowski, K., Zhang, F., Wei, K., Baglaenko, Y.,

- 1689 Brenner, M., Loh, P. ru, and Raychaudhuri, S. (2019). Fast, sensitive and accurate
 1690 integration of single-cell data with Harmony. *Nat. Methods* 16, 1289–1296.
- 1691 Kotecha, N., Krutzik, P.O., and Irish, J.M. (2010). Web-based analysis and publication of
 1692 flow cytometry experiments. *Curr. Protoc. Cytom. Chapter 10*, doi:
 1693 10.1002/0471142956.cy1017s53.
- 1694 Kuri-Cervantes, L., Pampena, M.B., Meng, W., Rosenfeld, A.M., Ittner, C.A.G., Weisman,
 1695 A.R., Agyekum, R., Mathew, D., Baxter, A.E., Vella, L., et al. (2020). Immunologic
 1696 perturbations in severe COVID-19/SARS-CoV-2 infection. *BioRxiv* 2020.05.18.101717.
- 1697 Kurth, F., Roennefarth, M., Thibeault, C., Corman, V.M., Müller-Redetzky, H., Mittermaier,
 1698 M., Ruwwe-Glösenkamp, C., Heim, K.M., Krannich, A., Zvorc, S., et al. (2020). Studying the
 1699 pathophysiology of coronavirus disease 2019: a protocol for the Berlin prospective COVID-
 1700 19 patient cohort (Pa-COVID-19). *Infection* 1(1), doi: 10.1007/s15010-020-01464-x.
- 1701 Kverneland, A.H., Streitz, M., Geissler, E., Hutchinson, J., Vogt, K., Boës, D., Niemann, N.,
 1702 Pedersen, A.E., Schlickeiser, S., and Sawitzki, B. (2016). Age and gender leucocytes
 1703 variances and references values generated using the standardized ONE-Study protocol.
 1704 *Cytom. Part A* 89, 543–564.
- 1705 Kwok, I., Becht, E., Xia, Y., Ng, M., Teh, Y.C., Tan, L., Evrard, M., Li, J.L.Y., Tran, H.T.N.,
 1706 Tan, Y., et al. (2020). Combinatorial Single-Cell Analyses of Granulocyte-Monocyte
 1707 Progenitor Heterogeneity Reveals an Early Uni-potent Neutrophil Progenitor. *Immunity*
 1708 S1074-7613(20)30235-1.
- 1709 Langereis, J.D., Pickkers, P., de Kleijn, S., Gerretsen, J., de Jonge, M.I., and Kox, M. (2017).
 1710 Spleen-derived IFN- γ induces generation of PD-L1 + -suppressive neutrophils during
 1711 endotoxemia . *J. Leukoc. Biol.* 102, 1401–1409.
- 1712 Lee, J.S., Park, S., Jeong, H.W., Ahn, J.Y., Choi, S.J., Lee, H., Choi, B., Nam, S.K., Sa, M.,
 1713 Kwon, J.-S., et al. (2020). Immunophenotyping of COVID-19 and influenza highlights the role
 1714 of type I interferons in development of severe COVID-19. *Sci. Immunol.* 5, eabd1554.
- 1715 Lenth, R. V. (2016). Least-squares means: The R package lsmeans. *J. Stat. Softw.* 69, 1–
 1716 33.
- 1717 Leshner, M., Wang, S., Lewis, C., Zheng, H., Chen, X.A., Santy, L., and Wang, Y. (2012).
 1718 PAD4 mediated histone hypercitrullination induces heterochromatin decondensation and
 1719 chromatin unfolding to form neutrophil extracellular trap-like structures. *Front. Immunol.*
 1720 3(307), doi: 10.3389/fimmu.2012.00307. eCollection 2012.
- 1721 Li, X.K., Lu, Q. Bin, Chen, W.W., Xu, W., Liu, R., Zhang, S.F., Du, J., Li, H., Yao, K., Zhai,
 1722 D., et al. (2018). Arginine deficiency is involved in thrombocytopenia and
 1723 immunosuppression in severe fever with thrombocytopenia syndrome. *Sci. Transl. Med.*
 1724 10(459), eaat4162.
- 1725 Liao, M., Liu, Y., Yuan, J., Wen, Y., Xu, G., Zhao, J., Cheng, L., Li, J., Wang, X., Wang, F.,
 1726 et al. (2020). Single-cell landscape of bronchoalveolar immune cells in patients with COVID-
 1727 19. *Nat. Med.* 26, 842–844.
- 1728 Liberzon, A., Birger, C., Thorvaldsdóttir, H., Ghandi, M., Mesirov, J.P., and Tamayo, P.
 1729 (2015). The Molecular Signatures Database Hallmark Gene Set Collection. *Cell Syst.* 1,
 1730 417–425.

- 1731 Lin, R.-J., Chu, J.-S., Chien, H.-L., Tseng, C.-H., Ko, P.-C., Mei, Y.-Y., Tang, W.-C., Kao, Y.-
 1732 T., Cheng, H.-Y., Liang, Y.-C., et al. (2014). MCPIP1 Suppresses Hepatitis C Virus
 1733 Replication and Negatively Regulates Virus-Induced Proinflammatory Cytokine Responses.
 1734 *J. Immunol.* 193, 4159–4168.
- 1735 Loftus, T.J., Mohr, A.M., and Moldawer, L.L. (2018). Dysregulated myelopoiesis and
 1736 hematopoietic function following acute physiologic insult. *Curr. Opin. Hematol.* 25, 37–43.
- 1737 Long, Q.-X., Liu, B.-Z., Deng, H.-J., Wu, G.-C., Deng, K., Chen, Y.-K., Liao, P., Qiu, J.-F.,
 1738 Lin, Y., Cai, X.-F., et al. (2020). Antibody responses to SARS-CoV-2 in patients with COVID-
 1739 19. *Nat. Med.* doi: 10.1038/s41591-020-0897-1.
- 1740 Lucas, C., Wong, P., Klein, J., Castro, T.B.R., Silva, J., Sundaram, M., Ellingson, M.K., Mao,
 1741 T., Oh, J.E., Israelow, B., et al. (2020). Longitudinal analyses reveal immunological misfiring
 1742 in severe COVID-19. *Nature* doi: 10.1038/s41586-020-2588-y.
- 1743 Lüdtke, A., Ruibal, P., Becker-Ziaja, B., Rottstegge, M., Wozniak, D.M., Cabeza-Cabrerozo,
 1744 M., Thorenz, A., Weller, R., Kerber, R., Idoyaga, J., et al. (2016). Ebola Virus Disease Is
 1745 Characterized by Poor Activation and Reduced Levels of Circulating CD16+ Monocytes. *J.*
 1746 *Infect. Dis.* 214, S275–S280.
- 1747 MacParland, S.A., Liu, J.C., Ma, X.Z., Innes, B.T., Bartczak, A.M., Gage, B.K., Manuel, J.,
 1748 Khuu, N., Echeverri, J., Linares, I., et al. (2018). Single cell RNA sequencing of human liver
 1749 reveals distinct intrahepatic macrophage populations. *Nat. Commun.* 9, 1–21.
- 1750 Maier, M.J. (2014). DirichletReg: Dirichlet Regression for Compositional Data in R.
 1751 <https://epub.wu.ac.at/id/eprint/4077>.
- 1752 Martin, M. (2011). Cutadapt removes adapter sequences from high-throughput sequencing
 1753 reads. *EMBnet.Journal* 17, 10.
- 1754 Maslove, D.M., Shapira, T., Tyryshkin, K., Veldhoen, R.A., Marshall, J.C., and Muscedere, J.
 1755 (2019). Validation of diagnostic gene sets to identify critically ill patients with sepsis. *J. Crit.*
 1756 *Care* 49, 92–98.
- 1757 Mathew, D., Giles, J.R., Baxter, A.E., Greenplate, A.R., Wu, J.E., Alanio, C., Oldridge, D.A.,
 1758 Kuri-Cervantes, L., Pampena, M.B., D'Andrea, K., et al. (2020). Deep immune profiling of
 1759 COVID-19 patients reveals patient heterogeneity and distinct immunotypes with implications
 1760 for therapeutic interventions. *BioRxiv Prepr. Serv. Biol.* 2020.05.20.106401.
- 1761 McKechnie, J.L., and Blish, C.A. (2020). The Innate Immune System: Fighting on the Front
 1762 Lines or Fanning the Flames of COVID-19? *Cell Host Microbe* 27(6), 863–869.
- 1763 Meghraoui-Kheddar, A., Chousterman, B.G., Guillou, N., Barone, S.M., Granjeaud, S.,
 1764 Vallet, H., Corneau, A., Guessous, K., Boissonnas, A., Irish, J.M., et al. (2020). Two new
 1765 immature and dysfunctional neutrophil cell subsets define a predictive signature of sepsis
 1766 useable in clinical practice. *BioRxiv* doi: 10.1101/2020.05.29.123992.
- 1767 Mei, H.E., Leipold, M.D., Schulz, A.R., Chester, C., and Maecker, H.T. (2015). Barcoding of
 1768 Live Human Peripheral Blood Mononuclear Cells for Multiplexed Mass Cytometry. *J.*
 1769 *Immunol.* 194, 2022–2031.
- 1770 Mei, H.E., Leipold, M.D., and Maecker, H.T. (2016). Platinum-conjugated antibodies for
 1771 application in mass cytometry. *Cytom. Part A* 89, 292–300.

- 1772 Mengos, A.E., Gastineau, D.A., and Gustafson, M.P. (2019). The CD14+HLA-DrLO/NEG
 1773 monocyte: An immunosuppressive phenotype that restrains responses to cancer
 1774 immunotherapy. *Front. Immunol.* 10, doi: 10.3389/fimmu.2019.01147.
- 1775 Merad, M., and Martin, J.C. (2020). Pathological inflammation in patients with COVID-19: a
 1776 key role for monocytes and macrophages. *Nat. Rev. Immunol.* 20(6), 355-362.
- 1777 Messner, C.B., Demichev, V., Wendisch, D., Michalick, L., White, M., Freiwald, A., Textoris-
 1778 Taube, K., Vernardis, S.I., Egger, A.-S., Kreidl, M., et al. (2020). Ultra-high-throughput
 1779 clinical proteomics reveals classifiers of COVID-19 infection. *Cell Syst.* doi:
 1780 10.1016/j.cels.2020.05.012.
- 1781 Meyer, C., Cagnon, L., Costa-Nunes, C.M., Baumgaertner, P., Montandon, N., Leyvraz, L.,
 1782 Michielin, O., Romano, E., and Speiser, D.E. (2014). Frequencies of circulating MDSC
 1783 correlate with clinical outcome of melanoma patients treated with ipilimumab. *Cancer*
 1784 *Immunol. Immunother.* 63, 247–257.
- 1785 Middleton, E.A., He, X.-Y., Denorme, F., Campbell, R.A., Ng, D., Salvatore, S.P., Mostyka,
 1786 M., Baxter-Stoltzfus, A., Borczuk, A.C., Loda, M., et al. (2020). Neutrophil Extracellular Traps
 1787 (NETs) Contribute to Immunothrombosis in COVID-19 Acute Respiratory Distress
 1788 Syndrome. *Blood* doi: 10.1182/blood.2020007008.
- 1789 Monneret, G., Lepape, A., Voirin, N., Bohé, J., Venet, F., Debard, A.L., Thizy, H., Bienvenu,
 1790 J., Gueyffier, F., and Vanhems, P. (2006). Persisting low monocyte human leukocyte
 1791 antigen-DR expression predicts mortality in septic shock. *Intensive Care Med.* 32, 1175–
 1792 1183.
- 1793 Mortaz, E., Alipoor, S.D., Adcock, I.M., Mumby, S., and Koenderman, L. (2018). Update on
 1794 neutrophil function in severe inflammation. *Front. Immunol.* 9(OCT), doi:
 1795 10.3389/fimmu.2018.02171.
- 1796 Naranjo-Gómez, J.S., Castillo, J.A., Rojas, M., Restrepo, B.N., Diaz, F.J., Velilla, P.A., and
 1797 Castaño, D. (2019). Different phenotypes of non-classical monocytes associated with
 1798 systemic inflammation, endothelial alteration and hepatic compromise in patients with
 1799 dengue. *Immunology* 156, 147–163.
- 1800 Ng, L.G., Ostuni, R., and Hidalgo, A. (2019). Heterogeneity of neutrophils. *Nat. Rev.*
 1801 *Immunol.* 19, 255–265.
- 1802 Ni, L., Ye, F., Cheng, M.L., Feng, Y., Deng, Y.Q., Zhao, H., Wei, P., Ge, J., Gou, M., Li, X.,
 1803 et al. (2020). Detection of SARS-CoV-2-Specific Humoral and Cellular Immunity in COVID-
 1804 19 Convalescent Individuals. *Immunity* doi: 10.1016/j.jimmuni.2020.04.023.
- 1805 Nowicka, M., Krieg, C., Crowell, H.L., Weber, L.M., Hartmann, F.J., Guglietta, S., Becher, B.,
 1806 Levesque, M.P., and Robinson, M.D. (2019). CyTOF workflow: differential discovery in high-
 1807 throughput high-dimensional cytometry datasets. *F1000Research* 6, 748.
- 1808 Pellin, D., Loperfido, M., Baricordi, C., Wolock, S.L., Montepeloso, A., Weinberg, O.K., Biffi,
 1809 A., Klein, A.M., and Biasco, L. (2019). A comprehensive single cell transcriptional landscape
 1810 of human hematopoietic progenitors. *Nat. Commun.* 10(1), 2395.
- 1811 Perlman, S., and Dandekar, A.A. (2005). Immunopathogenesis of coronavirus infections:
 1812 Implications for SARS. *Nat. Rev. Immunol.* 5, 917–927.
- 1813 Pfeiler, S., Massberg, S., and Engelmann, B. (2014). Biological basis and pathological

- 1814 relevance of microvascular thrombosis. *Thromb. Res.* 133.
- 1815 Pillay, J., Kamp, V.M., Van Hoffen, E., Visser, T., Tak, T., Lammers, J.W., Ulfman, L.H.,
1816 Leenen, L.P., Pickkers, P., and Koenderman, L. (2012). A subset of neutrophils in human
1817 systemic inflammation inhibits T cell responses through Mac-1. *J. Clin. Invest.* 122, 327–336.
- 1818 Popescu, D.M., Botting, R.A., Stephenson, E., Green, K., Webb, S., Jardine, L., Calderbank,
1819 E.F., Polanski, K., Goh, I., Efremova, M., et al. (2019). Decoding human fetal liver
1820 haematopoiesis. *Nature* 574, 365–371.
- 1821 Qiu, P., Simonds, E.F., Bendall, S.C., Gibbs, K.D., Bruggner, R. V., Linderman, M.D., Sachs,
1822 K., Nolan, G.P., and Plevritis, S.K. (2011). Extracting a cellular hierarchy from high-
1823 dimensional cytometry data with SPADE. *Nat. Biotechnol.* 29, 886–893.
- 1824 Quah, P., Li, A., Phua, J., and Phua, J. (2020). Mortality rates of patients with COVID-19 in
1825 the intensive care unit: A systematic review of the emerging literature. *Crit. Care* 24, 285.
- 1826 Remy, K.E., Brakenridge, S.C., Francois, B., Daix, T., Deutschman, C.S., Monneret, G.,
1827 Jeannet, R., Laterre, P.-F., Hotchkiss, R.S., and Moldawer, L.L. (2020). Immunotherapies for
1828 COVID-19: lessons learned from sepsis. *Lancet Respir. Med.* 2, 2–5.
- 1829 Reyes, M., Filbin, M.R., Bhattacharyya, R.P., Billman, K., Eisenhaure, T., Hung, D.T., Levy,
1830 B.D., Baron, R.M., Blainey, P.C., Goldberg, M.B., et al. (2020). An immune-cell signature of
1831 bacterial sepsis. *Nat. Med.* 26, 333–340.
- 1832 Reymond, N., Imbert, A.M., Devilard, E., Fabre, S., Chabannon, C., Xerri, L., Farnarier, C.,
1833 Cantoni, C., Bottino, C., Moretta, A., et al. (2004). DNAM-1 and PVR regulate monocyte
1834 migration through endothelial junctions. *J. Exp. Med.* 199, 1331–1341.
- 1835 Riegel, A., Maurer, T., Prior, B., Stegmaier, S., Heppert, V., Wagner, C., and Hänsch, G.M.
1836 (2012). Human polymorphonuclear neutrophils express RANK and are activated by its
1837 ligand, RANKL. *Eur. J. Immunol.* 42, 975–981.
- 1838 Ritchie, A.I., and Singanayagam, A. (2020). Immunosuppression for hyperinflammation in
1839 COVID-19: a double-edged sword? *Lancet* 395, 1111.
- 1840 Robbiani, D.F., Gaebler, C., Muecksch, F., Lorenzi, J.C.C., Wang, Z., Cho, A., Agudelo, M.,
1841 Barnes, C.O., Gazumyan, A., Finkin, S., et al. (2020). Convergent antibody responses to
1842 SARS-CoV-2 in convalescent individuals. *Nature* doi: 10.1038/s41586-020-2456-9.
- 1843 Sanchez-Cerrillo, I., Landete, P., Aldave, B., Sanchez-Alonso, S., Sanchez-Azofra, A.,
1844 Marcos-Jimenez, A., Avalos, E., Alcaraz-Serna, A., de los Santos, I., Mateu-Albero, T., et al.
1845 (2020). Differential Redistribution of Activated Monocyte and Dendritic Cell Subsets to the
1846 Lung Associates with Severity of COVID-19. *MedRxiv Prepr. Serv. Heal. Sci.*
1847 2020.05.13.20100925.
- 1848 Sander, L.E., Sackett, S.D., Dierssen, U., Beraza, N., Linke, R.P., Müller, M., Blander, J.M.,
1849 Tacke, F., and Trautwein, C. (2010). Hepatic acute-phase proteins control innate immune
1850 responses during infection by promoting myeloid-derived suppressor cell function. *J. Exp.*
1851 *Med.* 207, 1453–1464.
- 1852 De Santo, C., Salio, M., Masri, S.H., Lee, L.Y.H., Dong, T., Speak, A.O., Porubsky, S.,
1853 Booth, S., Veerapen, N., Besra, G.S., et al. (2008). Invariant NKT cells reduce the
1854 immunosuppressive activity of influenza A virus-induced myeloid-derived suppressor cells in
1855 mice and humans. *J. Clin. Invest.* 118, 4036–4048.

- 1856 Sawitzki, B., Harden, P.N., Reinke, P., Moreau, A., Hutchinson, J.A., Game, D.S., Tang, Q.,
 1857 Guinan, E.C., Battaglia, M., Burlingham, W.J., et al. (2020). Regulatory cell therapy in kidney
 1858 transplantation (The ONE Study): a harmonised design and analysis of seven non-
 1859 randomised, single-arm, phase 1/2A trials. *Lancet* 395, 1627–1639.
- 1860 Scapini, P., Marini, O., Tecchio, C., and Cassatella, M.A. (2016). Human neutrophils in the
 1861 saga of cellular heterogeneity: insights and open questions. *Immunol. Rev.* 273, 48–60.
- 1862 Schrijver, I.T., Kemperman, H., Roest, M., Kesecioglu, J., and de Lange, D.W. (2017).
 1863 Myeloperoxidase can differentiate between sepsis and non-infectious SIRS and predicts
 1864 mortality in intensive care patients with SIRS. *Intensive Care Med. Exp.* 5(1), doi:
 1865 10.1186/s40635-017-0157-y.
- 1866 Schultze, J.L., Mass, E., and Schlitzer, A. (2019). Emerging Principles in Myelopoiesis at
 1867 Homeostasis and during Infection and Inflammation. *Immunity* 50, 288–301.
- 1868 Schulz, A.R., and Mei, H.E. (2019). Surface barcoding of live PBMC for multiplexed mass
 1869 cytometry. In *Methods in Molecular Biology*, (Humana Press Inc.), pp. 93–108.
- 1870 Schuyler, R.P., Jackson, C., Garcia-Perez, J.E., Baxter, R.M., Ogolla, S., Rochford, R.,
 1871 Ghosh, D., Rudra, P., and Hsieh, E.W.Y. (2019). Minimizing Batch Effects in Mass
 1872 Cytometry Data. *Front. Immunol.* 10, doi: 10.3389/fimmu.2019.02367.
- 1873 Segawa, S., Kondo, Y., Nakai, Y., Iizuka, A., Kaneko, S., Yokosawa, M., Furuyama, K.,
 1874 Tsuboi, H., Goto, D., Matsumoto, I., et al. (2018). Placenta Specific 8 Suppresses IL-18
 1875 Production through Regulation of Autophagy and Is Associated with Adult Still Disease. *J.*
 1876 *Immunol.* 201, 3534–3545.
- 1877 Silvestre-Roig, C., Fridlender, Z.G., Glogauer, M., and Scapini, P. (2019). Neutrophil
 1878 Diversity in Health and Disease. *Trends Immunol.* 40, 565–583.
- 1879 Stiel, L., Delabranche, X., Galoisy, A.C., Severac, F., Toti, F., Mauvieux, L., Meziani, F., and
 1880 Boisramé-Helms, J. (2016). Neutrophil Fluorescence: A New Indicator of Cell Activation
 1881 during Septic Shock-Induced Disseminated Intravascular Coagulation. *Crit. Care Med.* 44,
 1882 e1132–e1136.
- 1883 Stiel, L., Meziani, F., and Helms, J. (2018). Neutrophil Activation during Septic Shock. *Shock*
 1884 49, 371–384.
- 1885 Stuart, T., Butler, A., Hoffman, P., Hafemeister, C., Papalex, E., Mauck, W.M., Hao, Y.,
 1886 Stoeckius, M., Smibert, P., and Satija, R. (2019). Comprehensive Integration of Single-Cell
 1887 Data. *Cell* 177, 1888-1902.e21.
- 1888 Tak, T., Wijten, P., Heeres, M., Pickkers, P., Scholten, A., Heck, A.J.R., Vrisekoop, N.,
 1889 Leenen, L.P., Borghans, J.A.M., Tesselaar, K., et al. (2017). Human CD62Ldim neutrophils
 1890 identified as a separate subset by proteome profiling and in vivo pulse-chase labeling. *Blood*
 1891 129, 3476–3485.
- 1892 Testa, U., Riccioni, R., Diverio, D., Rossini, A., Lo Coco, F., and Peschle, C. (2004).
 1893 Interleukin-3 receptor in acute leukemia. *Leukemia* 18, 219–226.
- 1894 Thomas, M.P., Whangbo, J., McCrossan, G., Deutsch, A.J., Martinod, K., Walch, M., and
 1895 Lieberman, J. (2014). Leukocyte Protease Binding to Nucleic Acids Promotes Nuclear
 1896 Localization and Cleavage of Nucleic Acid Binding Proteins. *J. Immunol.* 192, 5390–5397.

- 1897 Trouillet-Assant, S., Viel, S., Gaymard, A., Pons, S., Richard, J.C., Perret, M., Villard, M.,
 1898 Brengel-Pesce, K., Lina, B., Mezidi, M., et al. (2020). Type I IFN immunoprofiling in COVID-
 1899 19 patients. *J. Allergy Clin. Immunol.* 146(1), 206-208.e2.
- 1900 Uhel, F., Azzaoui, I., Grégoire, M., Pangault, C., Dulong, J., Tadié, J.M., Gacouin, A.,
 1901 Camus, C., Cynober, L., Fest, T., et al. (2017). Early expansion of circulating granulocytic
 1902 myeloid-derived suppressor cells predicts development of nosocomial infections in patients
 1903 with sepsis. *Am. J. Respir. Crit. Care Med.* 196, 315–327.
- 1904 Veglia, F., Perego, M., and Gabrilovich, D. (2018). Myeloid-derived suppressor cells coming
 1905 of age review-article. *Nat. Immunol.* 19, 108–119.
- 1906 Venet, F., Demaret, J., Gossez, M., and Monneret, G. (2020). Myeloid cells in sepsis-
 1907 acquired immunodeficiency. *Ann. N. Y. Acad. Sci.* doi: 10.1111/nyas.14333.
- 1908 Vo, A. Van, Takenaka, E., Shibuya, A., and Shibuya, K. (2016). Expression of DNAM-1
 1909 (CD226) on inflammatory monocytes. *Mol. Immunol.* 69, 70–76.
- 1910 Volkmann, J., Schmitz, J., Nordlohne, J., Dong, L., Helmke, A., Sen, P., Immenschuh, S.,
 1911 Bernhardt, W.M., Gwinner, W., Bräsen, J.H., et al. (2020). Kidney injury enhances renal G-
 1912 CSF expression and modulates granulopoiesis and human neutrophil CD177 in vivo. *Clin. Exp. Immunol.* 199, 97–108.
- 1914 Wang, D., Hu, B., Hu, C., Zhu, F., Liu, X., Zhang, J., Wang, B., Xiang, H., Cheng, Z., Xiong,
 1915 Y., et al. (2020). Clinical Characteristics of 138 Hospitalized Patients with 2019 Novel
 1916 Coronavirus-Infected Pneumonia in Wuhan, China. *JAMA* 323, 1061–1069.
- 1917 Wei, L., Wang, W., Chen, D., and Xu, B. (2020). Dysregulation of the immune response
 1918 affects the outcome of critical COVID-19 patients. *J. Med. Virol.* doi: 10.1002/jmv.26181.
- 1919 Wilk, A.J., Rustagi, A., Zhao, N.Q., Roque, J., Martínez-Colón, G.J., McKechnie, J.L., Ivison,
 1920 G.T., Ranganath, T., Vergara, R., Hollis, T., et al. (2020). A single-cell atlas of the peripheral
 1921 immune response in patients with severe COVID-19. *Nat. Med.* 26(7), 1070–1076.
- 1922 Xintian, X.I.A., Minyong, W.E.N., Shaofeng, Z., Jing, H.E., Weitao, C., Affiliated, F., and
 1923 Medicine, C. (2020). [An Increased Neutrophil/Lymphocyte Ratio Is an Early Warning Signal
 1924 of Severe COVID-19]. *J South Med Univ* 40, 333–336.
- 1925 Xu, Z., Shi, L., Wang, Y., Zhang, J., Huang, L., Zhang, C., Liu, S., Zhao, P., Liu, H., Zhu, L.,
 1926 et al. (2020). Pathological findings of COVID-19 associated with acute respiratory distress
 1927 syndrome. *Lancet Respir. Med.* 8, 420–422.
- 1928 You, Q., He, D.M., Shu, G.F., Cao, B., Xia, Y.Q., Xing, Y., Ni, M., Chen, J.F., Shi, S.L., Gu,
 1929 H.F., et al. (2019). Increased formation of neutrophil extracellular traps is associated with gut
 1930 leakage in patients with type 1 but not type 2 diabetes. *J. Diabetes* 11, 665–673.
- 1931 Younos, I.H., Abe, F., and Talmadge, J.E. (2015). Myeloid-derived suppressor cells: Their
 1932 role in the pathophysiology of hematologic malignancies and potential as therapeutic targets.
 1933 *Leuk. Lymphoma* doi: 10.3109/10428194.2014.987141.
- 1934 Yu, G., Wang, L.G., Han, Y., and He, Q.Y. (2012). ClusterProfiler: An R package for
 1935 comparing biological themes among gene clusters. *Omi. A J. Integr. Biol.* 16, 284–287.
- 1936 Zhou, F., Yu, T., Du, R., Fan, G., Liu, Y., Liu, Z., Xiang, J., Wang, Y., Song, B., Gu, X., et al.
 1937 (2020a). Clinical course and risk factors for mortality of adult inpatients with COVID-19 in

- 1938 Wuhan, China: a retrospective cohort study. Lancet 395, 1054–1062.
- 1939 Zhou, Z., Ren, L., Zhang, L., Zhong, J., Xiao, Y., Jia, Z., Guo, L., Yang, J., Wang, C., Jiang, S., et al. (2020b). Overly Exuberant Innate Immune Response to SARS-CoV-2 Infection. SSRN Electron. J. doi: 10.2139/ssrn.3551623.
- 1940
1941
- 1942 Ziyeng Ong, E., Fu Zi Chan, Y., Leong, W.Y., Mei Ying Lee, N., Kalimuddin, S., and Mohamed Haja Mohideen, S. (2020). A dynamic immune response shapes COVID-19 progression. Cell Host Microbe 27(6), 879-882.e2.
- 1943
1944
- 1945 Zuo, Y., Yalavarthi, S., Shi, H., Gockman, K., Zuo, M., Madison, J.A., Blair, C.N., Weber, A., Barnes, B.J., Egeblad, M., et al. (2020). Neutrophil extracellular traps in COVID-19. JCI Insight 5(11), e138999.
- 1946
1947
- 1948

Highlights

- SARS-CoV-2 infection induces profound alterations of the myeloid compartment
- Mild COVID-19 is marked by inflammatory HLA-DR^{hi}CD11c^{hi} CD14⁺ monocytes
- Dysfunctional HLA-DR^{lo}CD163^{hi} and HLA-DR^{lo}S100A^{hi} CD14⁺ monocytes in severe COVID-19
- Emergency myelopoiesis with immature and dysfunctional neutrophils in severe COVID-19

Analysis of patients with mild and severe COVID-19 reveals the presence of dysfunctional neutrophils in the latter that is linked to emergency myelopoiesis.

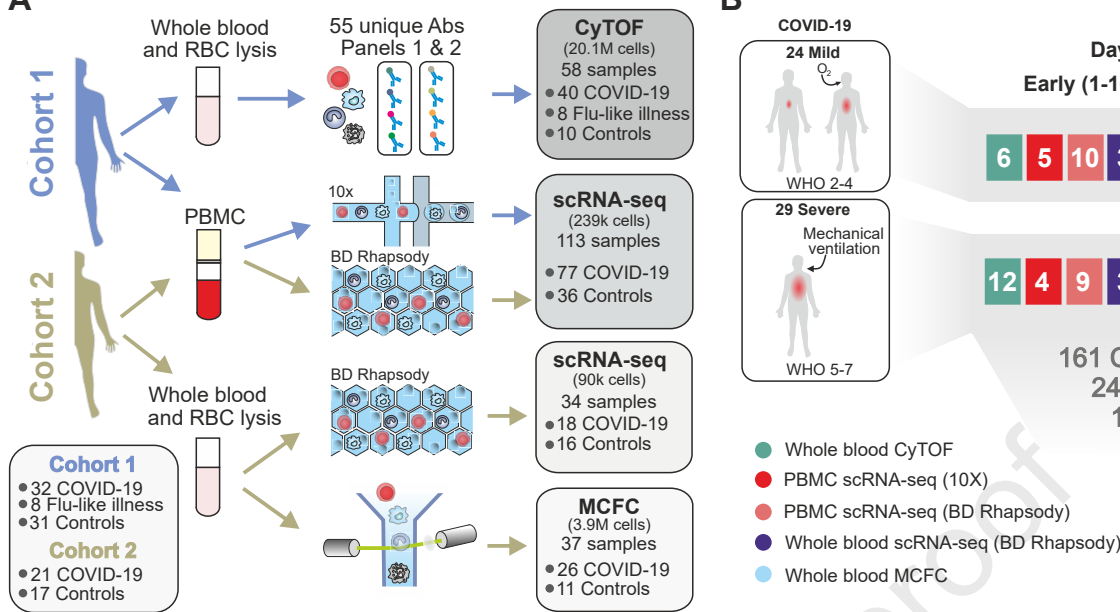
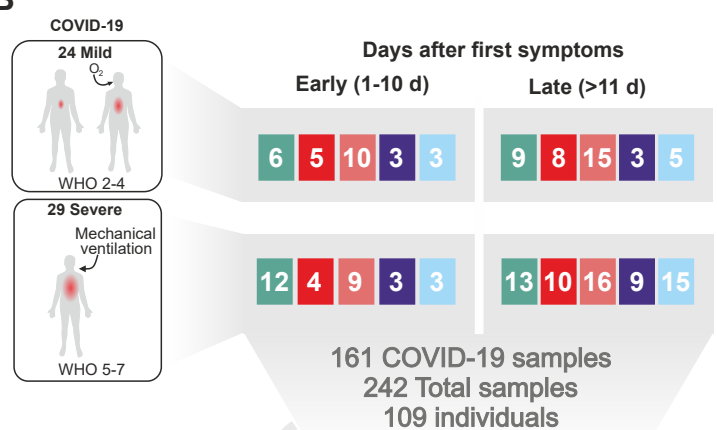
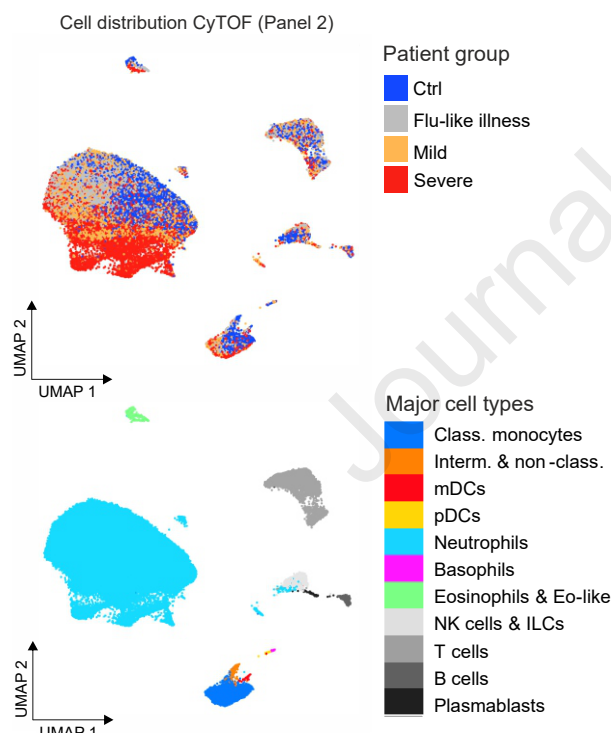
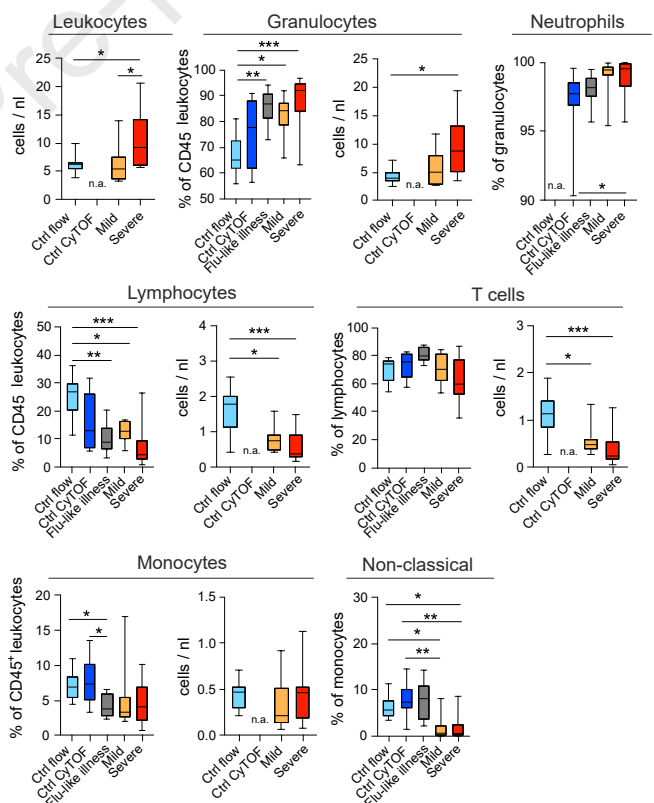
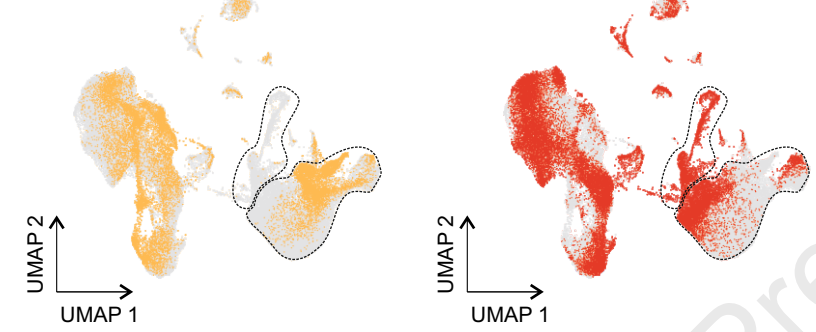
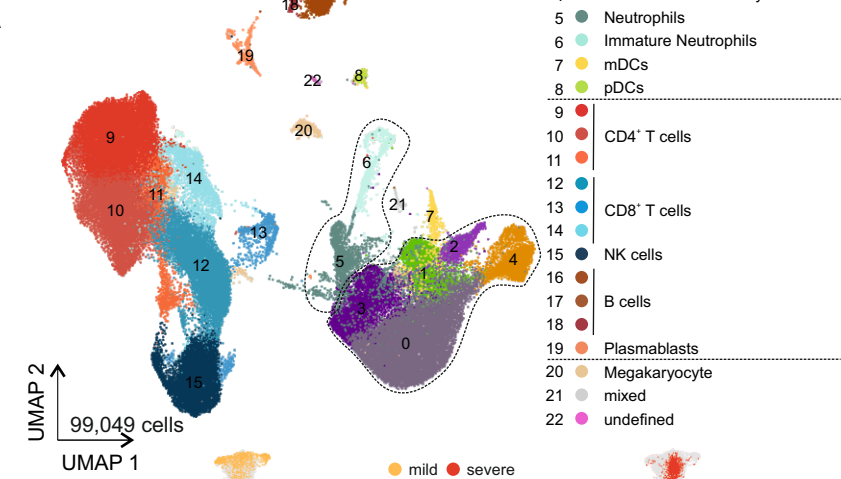
A**B****C****D**

Figure 2

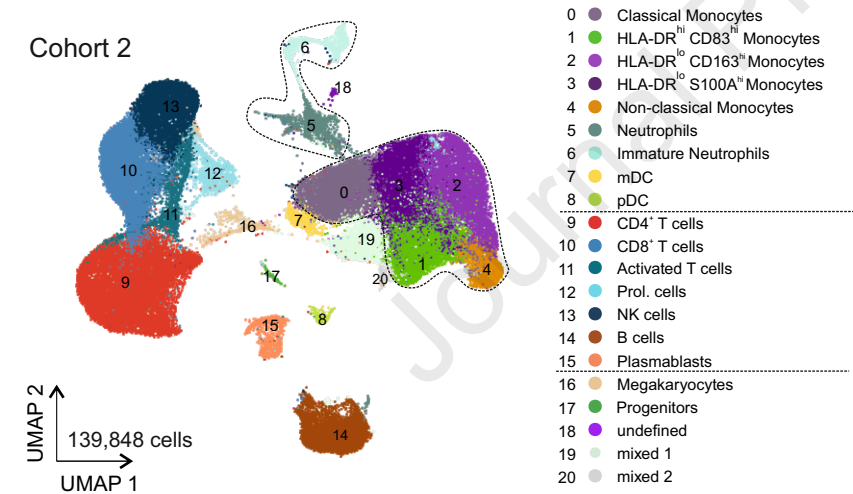
C

Journal Pre-proof

Cohort 1



Cohort 2



E

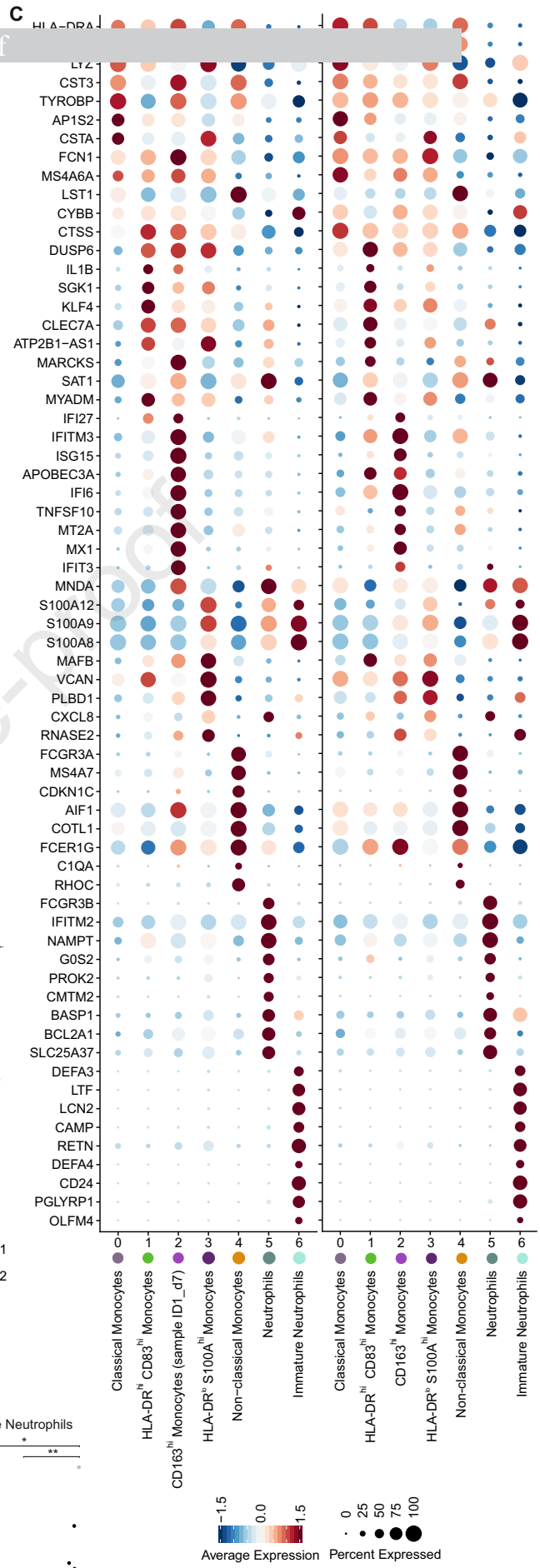
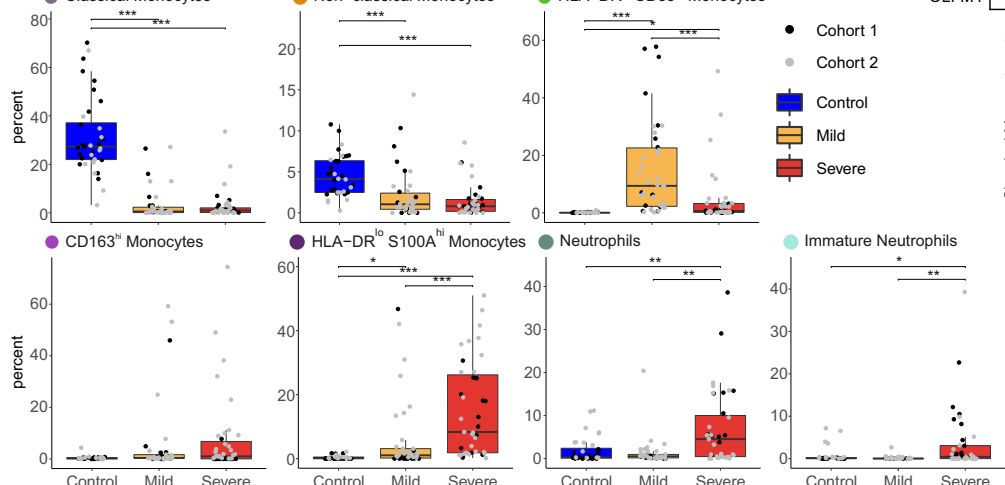
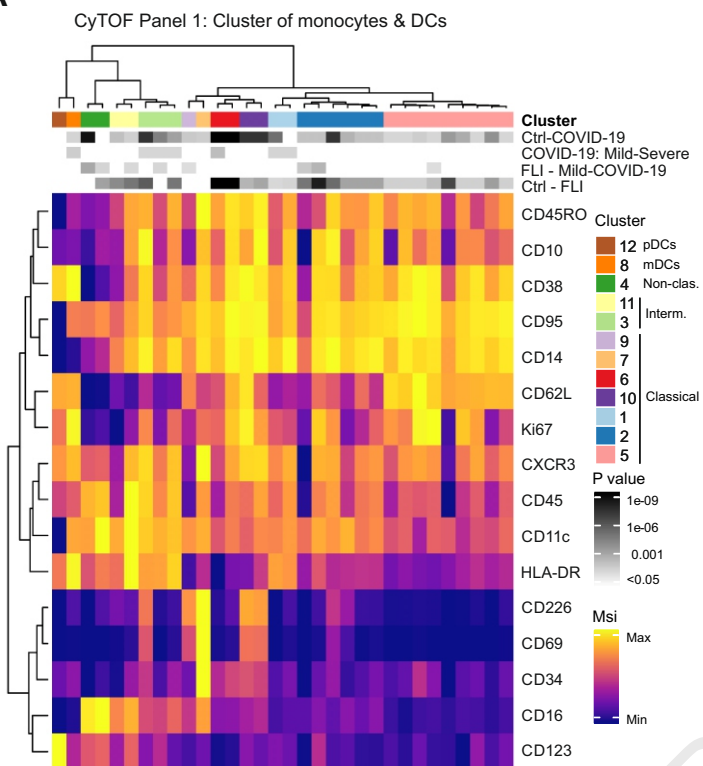


Figure 3

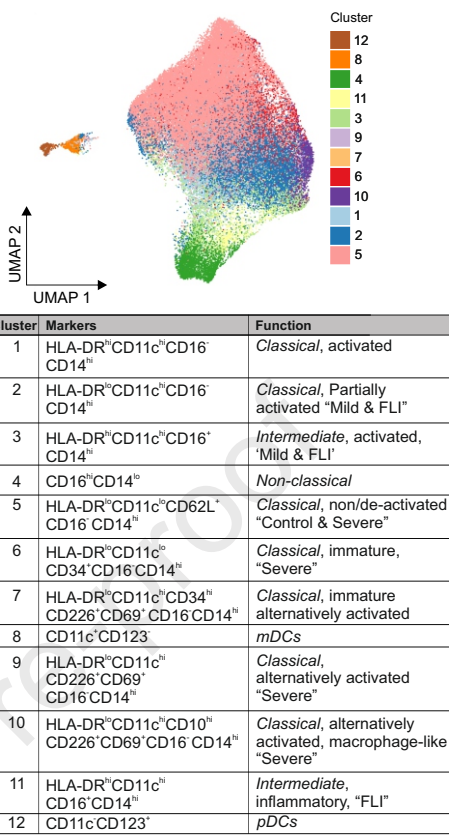
Journal Pre-proof

A

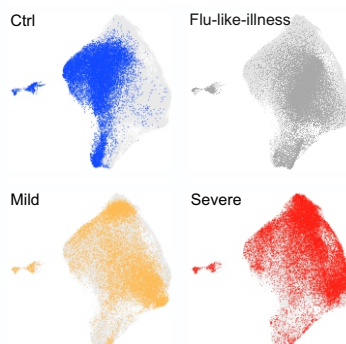
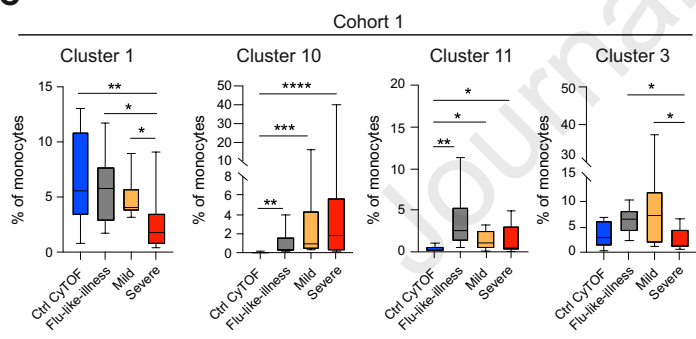


B

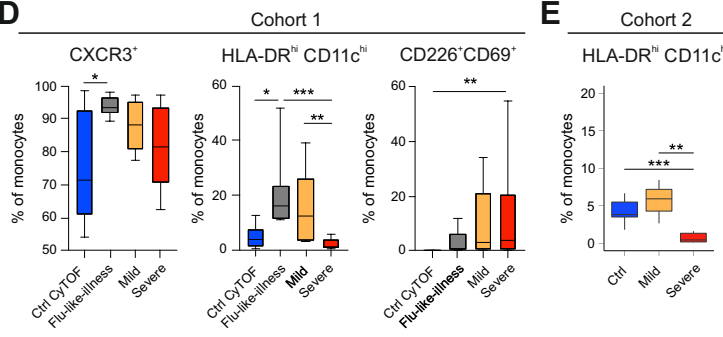
CyTOF Panel 1: Cluster of monocytes & DCs



C



D



E

Cohort 2

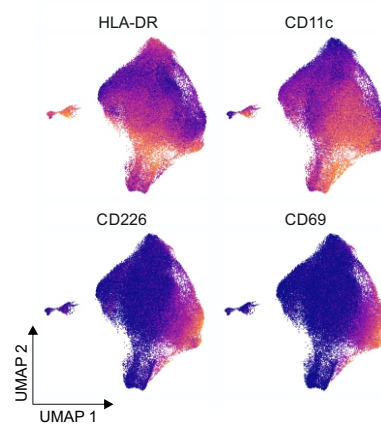
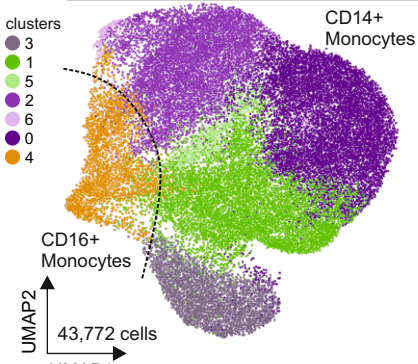


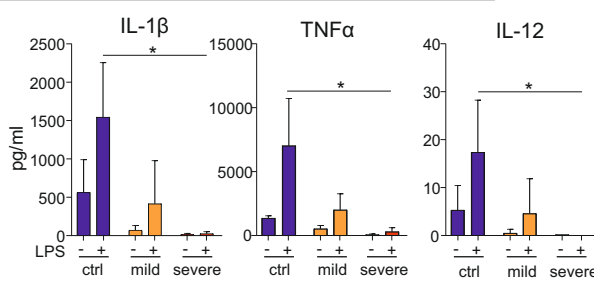
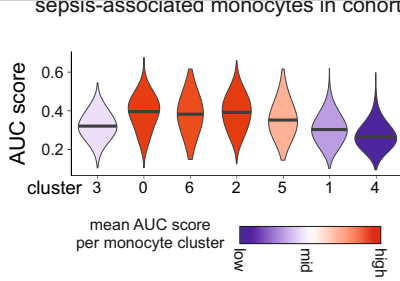
Figure 4

Journal Pre-proof

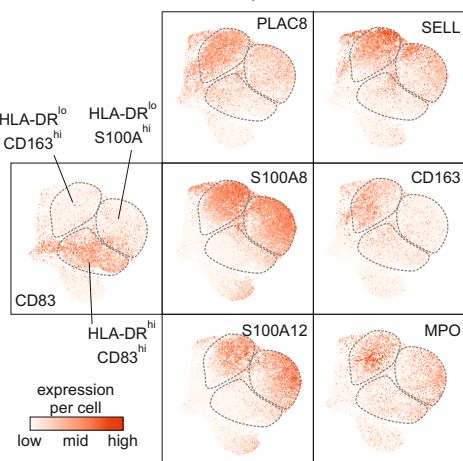
A



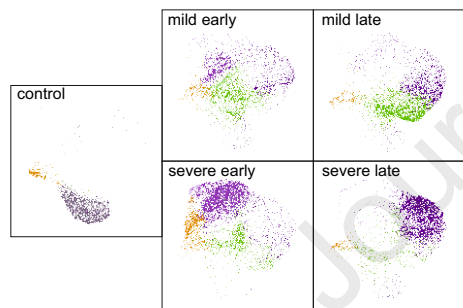
sepsis-associated monocytes in cohort 2



B Expression of markers in monocyte subsets of cohort 2

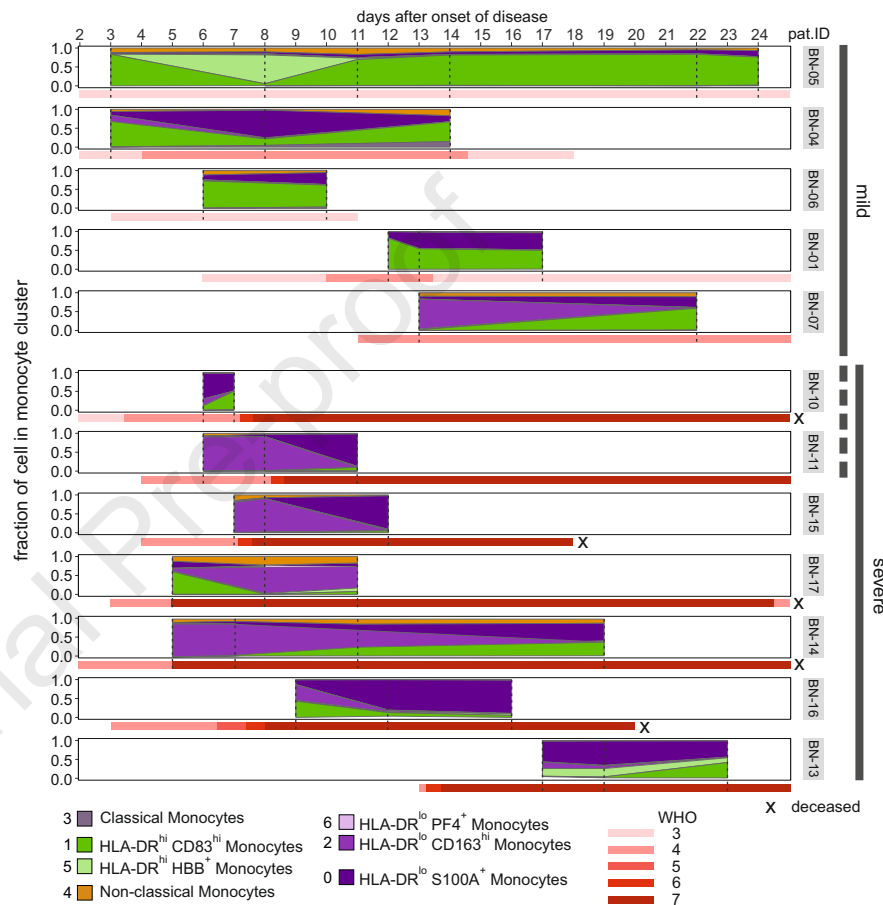


E Monocyte UMAP split by severity and disease stage

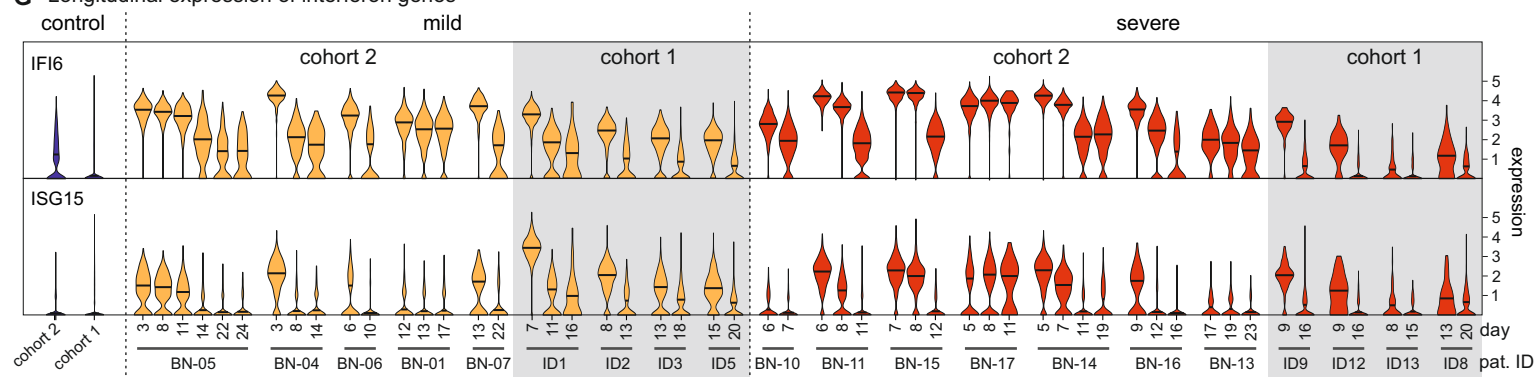


F

Longitudinal assessment of monocyte population distribution in cohort 2



G Longitudinal expression of interferon genes



H

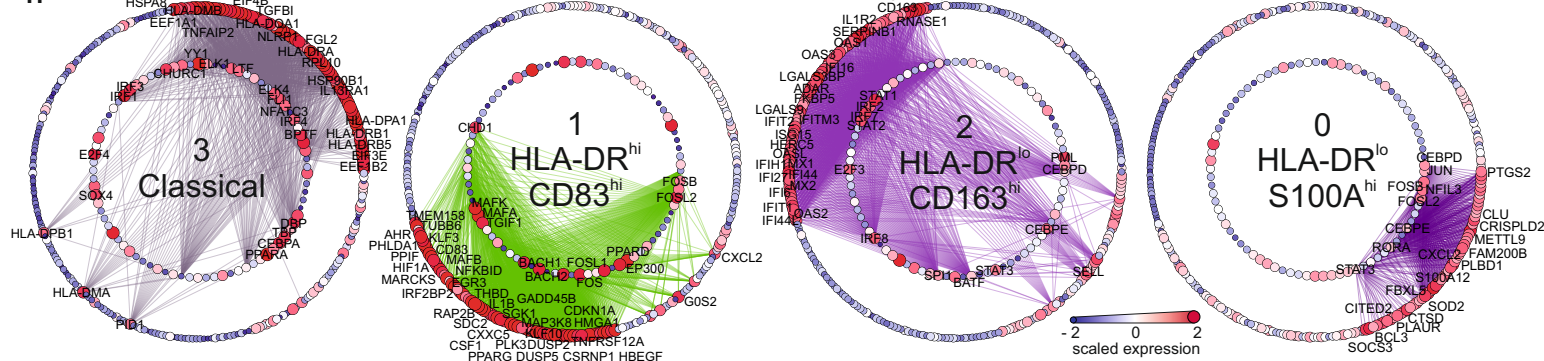
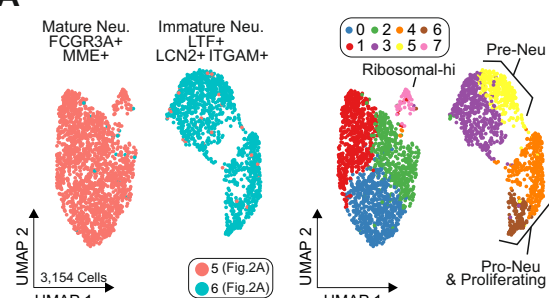


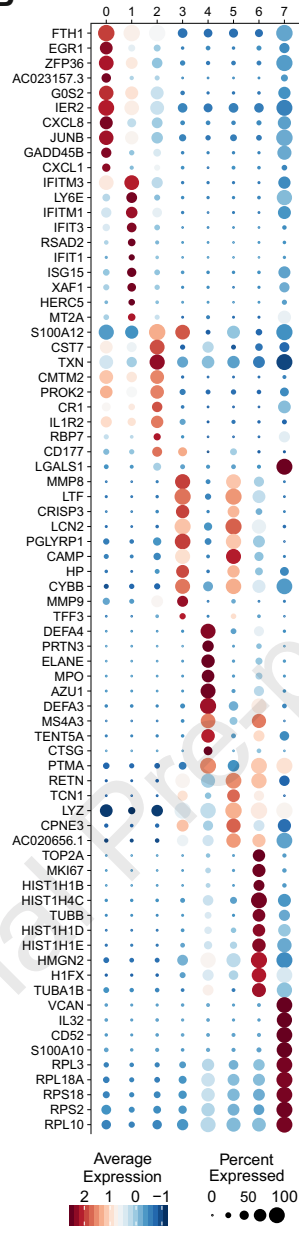
Figure 5

Journal Pre-proof

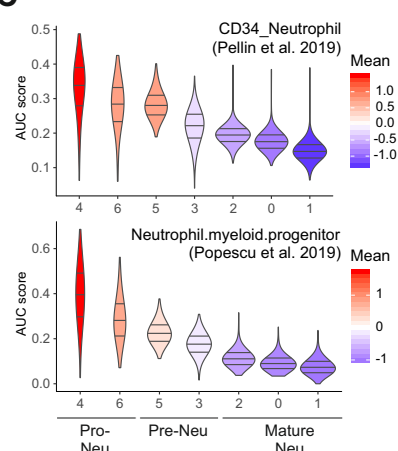
A



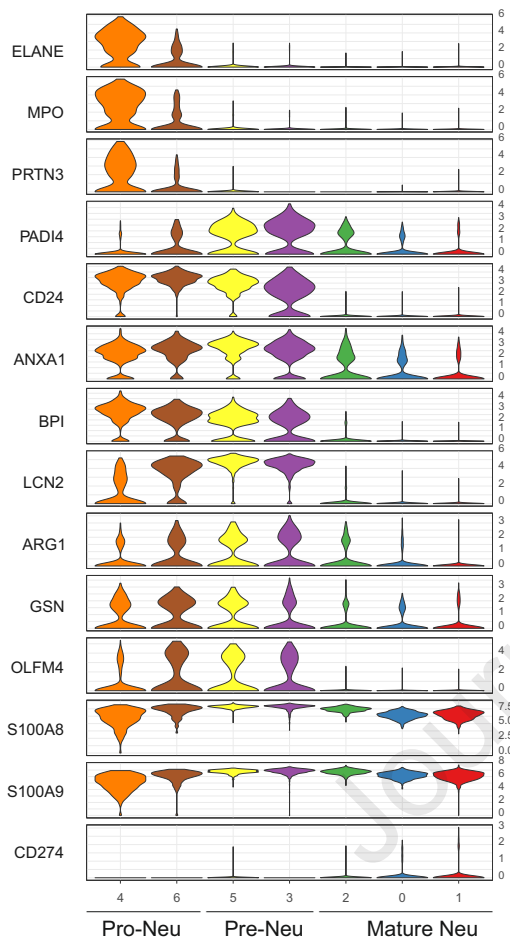
B



C



D



E

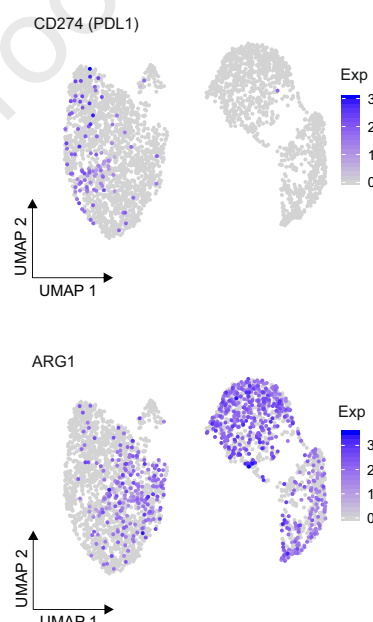
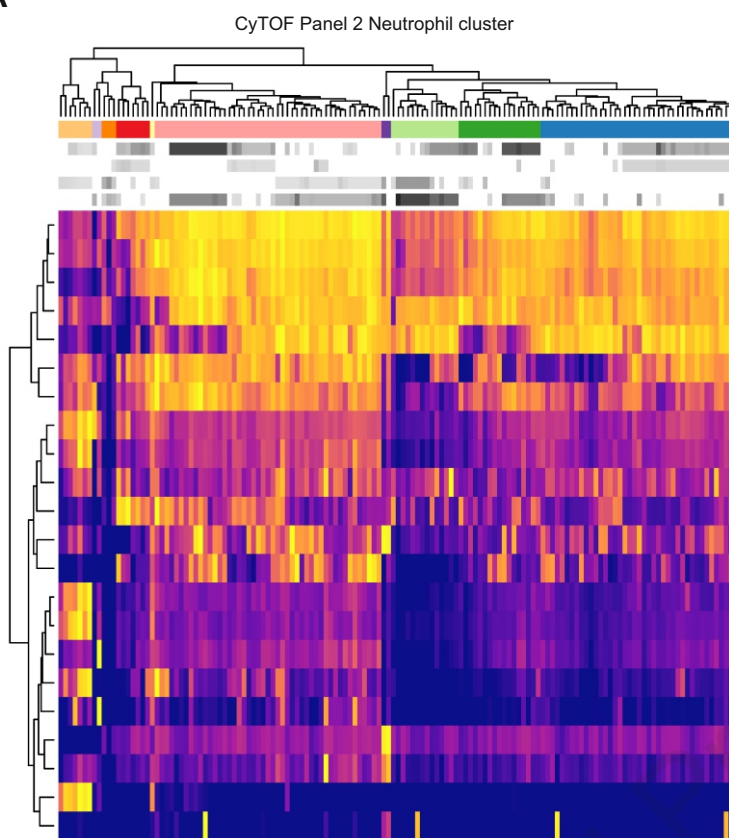


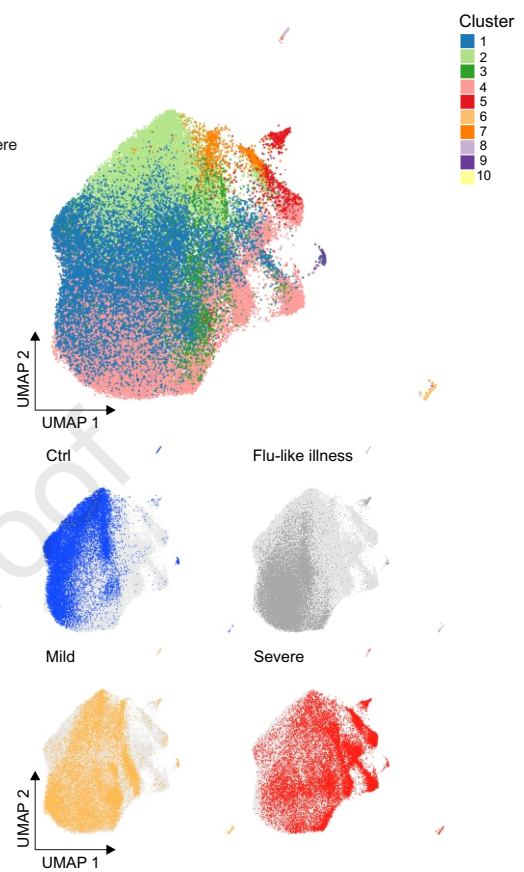
Figure 6

Journal Pre-proof

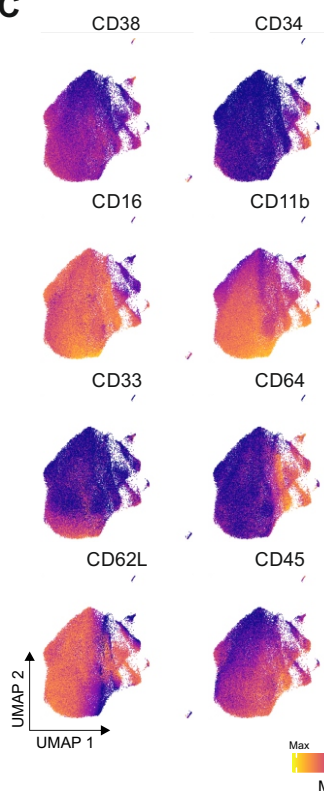
A



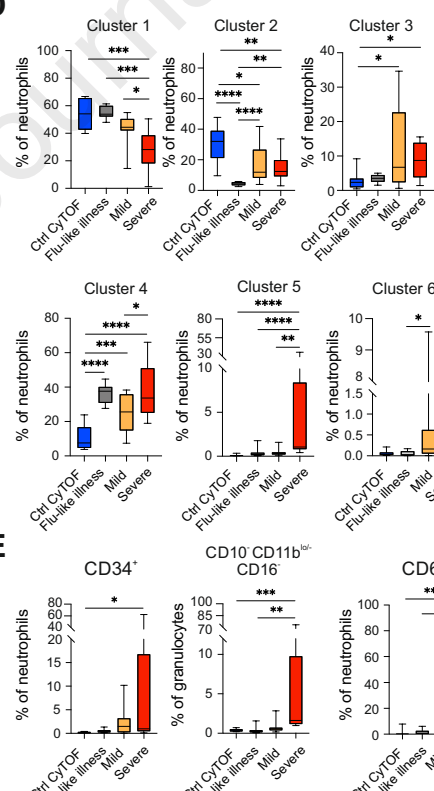
B



C



D



E

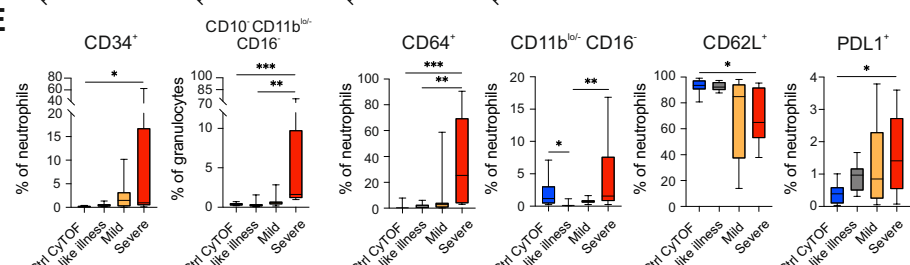


Figure 7

Journal Pre-proof

